UNIVERSITY OF CALIFORNIA,
IRVINE

Analysis of Laminar Nonpremixed Stagnation Flow and Swirl-Type Tubular Flames

DISSERTATION

submitted in partial satisfaction of the requirements
for the degree of

DOCTOR OF PHILOSOPHY

in Mechanical and Aerospace Engineering

by

Vinicius Maron Sauer

Dissertation Committee:
Professor Derek Dunn-Rankin, Chair
Professor William A. Sirignano
Professor Vince McDonell

2017

TABLE OF CONTENTS

LIST OF FIGURES

NOMENCLATURE

English

A	constant	
A	pre-exponential factor in Arrhenius equation	variable
a_0	function	
b	constant	
B_n	constants	
C	constant	
c	constant	
c	specific heat per unit mass	$\mathrm{J\,kg^{-1}\,K^{-1}}$
c_p	specific heat at constant pressure per unit mass	$\mathrm{J\,kg^{-1}\,K^{-1}}$
$\mathcal{D}$	mass diffusivity	$\mathrm{m^2\,s^{-1}}$
D	diameter	m
D/Dt	material derivative operator	
E	activation energy in Arrhenius equation	$\mathrm{J\,mol^{-1}}$
F	similarity variable	
$\mathbf{f}$	body force acceleration	$\mathrm{m\,s^{-2}}$
f	component of the body force acceleration	$\mathrm{m\,s^{-2}}$
G	similarity variable	
H	excess enthalpy	
H_0	distance between the stagnation plate and the oxidizer inlet	m
h	specific enthalpy	$\mathrm{J\,kg^{-1}}$
$\mathbf{j}_k$	diffusive mass flux of species k	$\mathrm{kg\,m^{-2}\,s^{-1}}$
L_0	distance between the burner ports in the counterflow configuration	m
Le	Lewis number	
M_k	molecular weight of species k	$\mathrm{kg\,mol^{-1}}$
$\dot{m}_F$	rate of consumption of fuel mass	$\mathrm{kg\,m^{-3}\,s^{-1}}$
$\dot{m}_k$	mass production rate of species k	$\mathrm{kg\,m^{-3}\,s^{-1}}$
P	function	
Pe	Péclet number	
Pr	Prandtl number	
p	gas pressure	Pa
Q	function	
$\mathbf{q}$	heat flux	$\mathrm{W\,m^{-2}}$
q	integrating factor	
q_c	amount of heat released per unit mass of fuel burnt	$\mathrm{kJ\,kg^{-1}}$
R	eigenfunction	
R	gas constant	$\mathrm{J\,mol^{-1}\,K^{-1}}$
Re	Reynolds number	
r	radial coordinate	m
r_D	characteristic length of diffusion in Roper model	m
S	mass of air consumed per unit mass of fuel burnt	

s	stoichiometric mass coefficient	
T	temperature	K
T_s	Sutherland constant	K
t	residence time in Roper model	s
t	time	s
$\mathbf{U}_k$	diffusion velocity vector of species k	$\mathrm{m\,s^{-1}}$
U	local undisturbed mean axial velocity	$\mathrm{m\,s^{-1}}$
U_k	diffusion velocity of species k in the axial direction	$\mathrm{m\,s^{-1}}$
U_r	scaled axial velocity in radial axisymmetric stagnation flow	$\mathrm{s^{-1}}$
U_z	scaled axial velocity in axial axisymmetric stagnation flow	$\mathrm{kg\,m^{-2}\,s^{-1}}$
$\mathbf{u}$	velocity vector	$\mathrm{m\,s^{-1}}$
u	axial velocity	$\mathrm{m\,s^{-1}}$
V	reference radial velocity	$\mathrm{m\,s^{-1}}$
V_k	diffusion velocity of species k in the radial direction	$\mathrm{m\,s^{-1}}$
V_r	scaled radial velocity in radial axisymmetric stagnation flow	$\mathrm{kg\,m^{-1}\,s^{-1}}$
V_z	scaled radial velocity in axial axisymmetric stagnation flow	$\mathrm{s^{-1}}$
v	radial velocity	$\mathrm{m\,s^{-1}}$
W_0	maximum intensity of the swirl velocity at the inlet	
W_z	scaled circumferential velocity in axial axisymmetric stagnation flow	$\mathrm{s^{-1}}$
w	circunferential velocity	$\mathrm{m\,s^{-1}}$
X	function	
Y_k	mass fraction of species k	
Z	mixture fraction	
z	axial coordinate	m

Greek

α	thermal diffusivity	$\mathrm{m^2\,s^{-1}}$
β	eigenvalues	
γ	adiabatic flame temperature increment	
δ	Diract delta function	
ε	perturbation term	
ζ	transformed coordinate	
η	transformed coordinate	
Θ	function	
θ	circumferential coordinate	rad
θ	transformed coordinate	
κ	thermal conductivity	$\mathrm{W\,m^{-1}\,K}$
Λ	pressure gradient	$\mathrm{N\,m^{-4}}$
λ	eigenvalues	
μ	dynamic viscotisy	$\mathrm{kg\,m\,s^{-1}}$
ν	kinematic viscotisy	$\mathrm{m^2\,s^{-1}}$
ν_k	stoichiometric coefficient of species k	$\mathrm{m^{-2}\,s^{-1}}$
ξ	transformed coordinate	
ρ	mass density	$\mathrm{kg\,m^{-3}}$
σ	weight function	

$\boldsymbol{\tau}$	stress tensor	$\mathrm{N^2\,m^{-1}}$
Φ	viscous dissipation	$\mathrm{kg\,m^{-1}\,s^{-3}}$
ϕ	eigenfunction	
σ_ϕ	weight function relative to the eigenfunction ϕ	
Ψ	stream function	$\mathrm{kg\,s^{-1}}$
ψ	function	
$\dot{\omega}_k$	molar rate of production of species k	$\mathrm{mol\,m^{-3}\,s^{-1}}$
ω	tangential component of vorticity	$\mathrm{s^{-1}}$

Subscripts

0	oxidizer inlet
0	reference
η	coordinate parallel to the stagnation surface
ξ	coordinate normal to the stagnation surface
F	fuel
f	fuel inlet
in	inner
k	species index
l	liquid phase
m	porous medium
O	oxidizer
out	outer
S	stoichiometric conditions
s	solid phase
w	wall

Superscripts

$'$	differentiation with respect to r
$*$	perturbation term
0	impermeable walls
$\widehat{\ }$	nondimensional variable
o	undisturbed term

ACKNOWLEDGMENTS

We try to control and plan it, but life remains that unpredictable thing that keeps surprising us every single day. Actually, so many of these unexpected events have happened over the course of the past five years that just remembering them, as well as all the people involved, is a tremendous experience.

I would probably not be finishing my PhD at UCI if I did not have extensive help from my Master's thesis advisor, Prof. Albino Leiroz. Without his support and encouragement I would not have applied for the scholarship that supported my studies. I am very thankful to him. It was also Prof. Leiroz who introduced me to my PhD advisor, Prof. Derek Dunn-Rankin.

Prof. Dunn-Rankin is one of those rare people someone finds in a lifetime. I have not met a single colleague who does not find him one of the most supportive, encouraging and motivating faculty he/she has ever met. It is impossible to describe how important all the mentoring he has provided to both my academic and personal life during my PhD. I cannot imagine a better academic role model. Thank you, Professor, for having me in your research group. It was quite an experience.

I would like to thank Professors William Sirignano and Vincent McDonell for being the readers of my dissertation. I appreciate all the valuable guidance and feedback. I want to thank Prof. Fernando Fachini (who was also in my Master's thesis committee) for generously sharing his time discussing the subtleties of theoretical combustion. His collaboration was of paramount importance to the description of some models in this manuscript.

The support and collaboration of all my colleagues from the Laser, Flames and Aerosols Research Group was extremely important. Thank you Jesse Tinajero (my first cubemate in the lab), David Escofet-Martin, Rosa Padilla, Sunny Karnani, Jin Dang, Mazdak Kebria, Ali Ziaee, Alice Chien, John Garman, Marco Minniti, Michael Bryant, Valentina Ricchiuti, Michela Vicariatto, Claudia Francisca Lopez Camara, and Andrea Biasioli. I want to tank all the undergraduate students who worked with me in a variety of projects and hope that the experience was worth it.

I would like to acknowledge the support from the staff of the Department of Mechanical and Aerospace Engineering, particularly, Louise Yeager, David Hartwig, Steve Heck, Edward Lau, Tucker Parris, Steve Weinstock and Ted Ediss.

I would like to thank the Brazilian National Council for Scientific and Technological Development (CNPq) for the doctoral scholarship program that supported and made this PhD possible. I would like to thank UCI for the Miguel Velez Scholarship, and the Department of Mechanical and Aerospace Engineering for the financial support.

Thank you to all friends we made throughout the past five years. Thank you Arnold, Rina and all the Guerra family for being our family in the US, Raphael and Ana Paula Ribeiro,

Arthur Valadares, Paula Yamashita, Ana Carolina and Christian Adriano, Juliana Zanotto and family, Bianca Endo and Felipe Augusto de Souza.

Last but not least¸ I would like to thank my family. My parents, my sister and all the new members that have recently joined us. Maria Fernanda, Bernard and Alice, thank you from the bottom of my heart for sharing your love and life with me. This is just the beginning.

CURRICULUM VITAE

Vinicius Maron Sauer

EDUCATION

Ph.D., Mechanical and Aerospace Engineering — **2017**
University of California, Irvine — Irvine, California

M.S., Mechanical Engineering — **2012**
Univerisdade Federal do Rio de Janeiro — Rio de Janeiro, Rio de Janeiro

B.S., Mechanical Engineering — **2010**
Univerisdade Federal do Rio de Janeiro — Rio de Janeiro, Rio de Janeiro

RESEARCH EXPERIENCE

Graduate Student Researcher — **2012–2017**
University of California, Irvine — Irvine, California

Graduate Student Researcher — **2010–2012**
Universidade Federal do Rio de Janeiro — Rio de Janeiro, Rio de Janeiro

Undergraduate Student Researcher — **2009–2010**
Universidade Federal do Rio de Janeiro — Rio de Janeiro, Rio de Janeiro

TEACHING EXPERIENCE

Teaching Assistant — **2012–2017**
University of California, Irvine — Irvine, California

Instructor/Coordinator — **2005–2009**
EDUCAFRO — Rio de Janeiro, Rio de Janeiro

Teaching Assistant — **2012–2017**
Universidade Federal do Rio de Janeiro — Rio de Janeiro, Rio de Janeiro

SCHOLARSHIPS, HONORS AND AWARDS

CNPq Brazil
Ph.D. Scholarship — 2012–2016
M.S. Scholarship — 2010

ANP Brazil
M.S. PRH 37 Scholarship — 2010–2012

Combustion Institute Travel Awards

Internation Symposium on Combustion	2016 and 2014
Technical Meeting, Western States Section of the Combustion Institute	2015 and 2013
US National Combustion Meeting	2017 and 2015

PUBLICATIONS

Refereed Publications

Sauer, V. M., Dunn-Rankin, 2017, "Impinging Nonpremixed Coflow Methane-Air Flames with Unity Lewis Number," Proceedings of the Combustion Institute, 36, 1, pp. 1411-1419

Conference Papers (full papers, full peer-review)

Sauer, V. M., Dunn-Rankin, D., 2017. "Porous Wall Fed Liquid Fuel Nonpremixed Swirl-Type Tubular Flames," Proceedings of the 26th International Colloquium on the Dynamic of Explosions and Reactive Systems (ICDERS), Boston, MA

Sauer, V. M., Leiroz, A. J. K., Colaço, M. J., 2012. "Analysis of Biofuels Reacting Flows in Ducts," Presented at the 14th Brazilian Thermal Science Meeting (ENCIT), Rio de Janeiro, RJ

Conference Papers (full papers, acceptance based on abstract)

Sauer, V. M., Fachini, F.F., Dunn-Rankin, D., 2017. "Structure of Nonpremixed Swirl-Type Tubular Flames Burning Condensed Fuels with Unity Lewis Numbers," Presented at the 10th US Combustion Meeting, Washington, MD

da Silva, A. P., Sauer, V. M., Dunn-Rankin, D., 2015. "Experimental Evaluation of a Miniature Liquid Film Combustor with Secondary Air Injection," Presented at the Fall 2015 Meeting of the Western States Section of the Combustion Institute, Provo, UT

Sauer, V. M., Dunn-Rankin D., 2015. "Impinging Coflow Nonpremixed Methane-Air Flames with Unity Lewis Number," Presented at the 9th US Combustion Meeting, Cincinnati, OH

Sauer, V. M., Padilla, R. E., Dunn-Rankin, D., 2013. "Analyzing Water-Laden Non-Premixed Counterflow Flames Using the Mixture Fraction/ Excess-Enthalpy Approach," Presented at the Fall 2013 Meeting of the Western States Section of the Combustion Institute, Fort Collins, CO, USA

Conference Papers (abstract only)

Sauer, V. M., Dunn-Rankin, D., 2016. "Parametric Uncertainty in the Analysis of the Steady-State and Extinction Characteristics Nonpremixed Laminar Flames with Simplified Chemistry," Work-in-Progress Poster, 36th International Symposium on Combustion, Seoul, SCA

Sauer, V. M., Dunn-Rankin, D., 2014. "Analyzing Water-Laden Non-Premixed Counterflow Flames Using Generalized Shvab-Zel'dovich Variables," Work-in-Progress Poster, 35th International Symposium on Combustion, San Francisco, CA

Submitted

Sauer, V. M., Fachini, F. F., Dunn-Rankin, D., "Nonpremixed Swirl-Type Tubular Flames Burning Liquid Fuels," Journal of Fluid Mechanics

In Preparation
Sauer, V. M., Dunn-Rankin, D., "Nonpremixed Swirl-Type Tubular Flames"

PRESENTATIONS

Sauer, V. M. and Dunn-Rankin, D., 2016. "Impinging Nonpremixed Coflow Methane-Air Flames with Unity Lewis Number," 36th International Symposium on Combustion, Seoul, SCA

Sauer, V. M., Leiroz, A. J. K., Colaço, M. J., 2011. "Biofuel Reacting Flows in Ducts with Variable Section and Bluff Bodies," (in Portuguese) ANP Annual Meeting, Florianópolis, SC

EDITORIAL DUTIES

Referee/Reviewer
Combustion Science and Technology, Fuel, Proceedings of the Royal Society A, ABCM International Congress of Mechanical Engineering (Brazil)

MENTORING

Undergraduate Researchers

Jagdeep S. Batther, Project: Annular Miniature Combustor	2017
Marion Lallemand, Project: Miniature Combustor with Porous Walls	2016
Igor M. Alves, Project: PIV System Calibration Using a Laminar Pipe Flow	2016
André P. da Silva, Project: Miniature Liquid Film Combustor	2015
Muath Askar, Project: Parabolic Solar Stove Cooker	2015
Ahmed Alharbi, Project: Parabolic Solar Stove Cooker	2015
Saad Almuhanna, Project: Analysis of Laminar Pipe Flows Using PIV	2015

MEMBERSHIPS

Combustion Institute	2013–Present
ABCM (Brazil)	2015

PARTICIPATION IN EVENTS

Uncertainty Quantification Summer School USC, Los Angeles, CA	2016
5th School of Combustion ICISS, São Paulo, SP	2015
Princeton-CEFRC Summer School, Princeton, NJ	2014

ABSTRACT OF THE DISSERTATION

Analysis of Laminar Nonpremixed Stagnation Flow and Swirl-Type Tubular Flames

By

Vinicius Maron Sauer

Doctor of Philosophy in Mechanical and Aerospace Engineering

University of California, Irvine, 2017

Professor Derek Dunn-Rankin, Chair

Combustion is expected to remain one of the main sources of power in the world. Therefore, the understanding of the underlying physical and chemical processes needs to continue improving, to increase efficiency and to reduce emissions of combustion systems. In order to study the steady-state characteristics of complex flame configurations, laminar surrogate models can aid significantly in the description of more complicated systems. One valuable class of surrogate configurations is the nonpremixed laminar flame, in which fuel and oxidizer are initially separated. In nonpremixed flames the mixing process is a necessary part of the flow to be investigated and the chemical process can be represented by a global reaction mechanism. Such simplification allows the conservation equations to be treated with analytical or semi-analytical methods, while still capturing the critical physical characteristics of the system. The dissertation describes and analyzes three laminar nonpremixed stagnation flow models based on canonical flame configurations: a coflow impinging flame, a water-laden counterflow flame, and a tubular counterflow burning condensed fuels. The performance of the theoretical models is validated with experimental data available in the literature. In addition, the nonpremixed swirl-type tubular flame configuration is presented for the case of a liquid fueled porous wall fed system. The experimental system and the mathematical model that describes theoretically

the configuration are evaluated. To this end, a novel analytical solution based on asymptotic methods is presented.

Chapter 1

Introduction

1.1 Overview

Combustion is a remarkable phenomenon that is, at the same time trivial to describe (e.g., the fire triangle of heat, fuel, and oxidizer), and extraordinarily complex (e.g., turbulent multiphase reacting flows). The simplicity of combustion allowed its discovery and utilization by early humans and its complexity creates environmental impact challenges. This dichotomy has given rise to two approaches in combustion science — one following the detailed chemistry and fluid mechanics, and the other exploring the core aspects via physically relevant simplified systems that are analytically tractable. This dissertation follows the latter path.

Mankind's discovery of the ignition process leading to combustion about 30 000 years ago [1] was a turning point in the evolution of the human race. Fire was used to keep people warm, to cook their food, in fire drives in hunting or warfare, to kill insects, and to clear forests, among others [2]. These new abilities allowed the expansion of human activity. Early uses of combustion technology as a source of power to drive systems have also been documented,

including the Aeolipile proposed by Hero of Alexandria in the 1st century BC. Since then, several devices based on burning of fuels have been developed, such as Thomas Newcomen's atmospheric engine (1712), and Nikolaus Otto's (1876) and Rudolf Diesel's (1900) engines. Nowadays, combustion engines are an important part of most people's everyday life and they are expected to remain one of the main sources of power in the world. The science of combustion started its development, in the last half of the nineteenth century, with the experiments of Sir Humphry Davy (1815), Robert Bunsen (1866), Claude Louis Berthelot and Paul Marie Eugene Vieille (1881, 1882) and Ernest Mallard and Henry Louis le Chatelier (1881, 1883), as well as with the theories of Vladimir Aleksandrovich Mikhel'son (1890), David Leonhard Chapman (1899) and Emile Jouguet (1905) [3]. Combustion science, i.e., the understanding of the underlying physical and chemical processes, needs to continue improving, helping to increase the efficiency and to reduce the emissions of combustion systems.

Combustion processes are, mainly, highly exothermic gas-phase chemical reactions between oxidizer and fuels, described theoretically through the interaction of the disciplines of thermodynamics, fluid mechanics, kinetic theory and chemical kinetics. In many combustion systems, fuel and oxidizer are initially separated. In the high temperature zones of these nonpremixed reacting systems, in which the reaction time is very short, reactants coexist only in thin reaction layers. Fuel and oxidizer, after arriving from opposite sides, are consumed while crossing the flame by diffusion. Nonpremixed flames are very common in engineering systems for propulsion and energy production, including diesel engines, gas turbines, rocket engines, and power-plant furnaces, in heating devices for domestic applications, and in the process industry [4]. The complete description of these practical combustion devices requires time-dependent three-dimensional geometries and chemical models of complex fuels, which typically involve a number of chemical species and reactions. Such systems are too complex to be modeled effectively using elementary chemical kinetics and full-fluid mechanical description [5]. For that reason, simplified

models that provide fundamental understanding of flame structure and the influence of key parameters on reacting flows have been developed, for example, concentrating on the details of combustion chemistry and flame structure in idealized laboratory settings [5]. These surrogate systems are often called canonical flame configurations.

Each of the disciplines used to describe a reacting flow can be simplified to different levels of detail. The Navier-Stokes equation, i.e., the momentum conservation equations, together with the continuity equation and an equation of state, describe the flow field of a moving fluid. A number of flow conditions can be characterized by simple forms of the momentum equation. For instance, flows with similarity conditions, such as stagnation point flows, in which a set of assumptions leads to the exact elimination of terms, or flows in which some terms become small compared to others, such as systems where the boundary-layer theory is valid. The relation between state variables is commonly described by the ideal gas law. The first law of thermodynamics, which governs the relations between heat and other forms of energy, is often simplified by omitting or modeling complicated interactions internal or external to the system. Most commonly, the enthalpy flux is neglected, the heat capacity of the mixture is approximated by a polynomial fit in the temperature, the Lewis number (the ratio of thermal to mass diffusivity) is assumed approximately constant, the diffusion flux is given by Fick's law, and the viscosity of a mixture is given as a function of the Prandtl number (the ratio of the momentum to thermal diffusivity) [6]. The Soret effect (species flux due to temperature gradient), the Duffour effect (energy flux due to species concentration gradient), and radiation heat transfer are often neglected as well. The approximation of the reaction rate using an Arrhenius equation and the law of mass action, usually assumed in combustion theory, is often sufficient to reveal the basic features of a process, since the detailed kinetics of the chemical change is not always known [7].

The approximations considered in the theoretical description of reacting flow, thus, require the specification of a number of thermodynamic and kinetic rate parameters. Those

quantities are typically derived from empirical observations, and therefore involve some degree of uncertainty due to limitations in experimental measurements [8]. At the same time, the physical models may involve uncertainty in model structure, parameters, geometry, inputs, initial conditions, boundary conditions, and strong non-linear dependence on temperature [9]. For that reason, even detailed models that attempt to take into account all scales involved in the description of reacting systems might suffer from some level of approximation. Notwithstanding, the more intricate the theoretical model describing a phenomenon, the more time consuming is the process of obtaining its solution. A good example is the estimation of transport coefficients in multicomponent systems, such as reacting flows. In those systems, the detailed models consider the interactions between all species. In order to do so, kinetic theory of gases is used to evaluate the coefficients, an effort that requires the solution of linear systems arising from Galerkin approximations of the linearized Boltzmann equation [10]. Such a task is computationally expensive, and, for some systems, impractical with the computational resources available. More importantly, the determination of transport coefficients represents only a fraction of the total effort involved in the complete theoretical description of a reacting flow. As an alternative, simplifications in the conservation equations that allow them to be treated analytically or semi-analytically can provide some qualitative or even quantitative metrics that improve the understanding of such systems or provide new viewpoints.

1.2 Objective

The present work aims to extend classical theoretical combustion models (e.g., [11–13]) in order to analyze both new and existing nonpremixed flames configurations operating at conditions in which simplified analytical and semi-analytical models have not been applied. Such mathematical descriptions can provide design parameters for the development and

improvement of physical systems, as well as aid in the evaluation of uncertainties associated to the models — which is beyond the scope of this manuscript. Unusual configurations based on canonical nonpremixed systems are described, modeled and solved through various techniques. In addition, an experimental setup accompanied by a theoretical model is presented for a condition in which canonical nonpremixed systems have not been described. The laminar systems discussed herein are categorized into stagnation flow flames and swirl-type tubular flames. The stagnation systems are analyzed depending on the direction of the stagnation plane, i.e., axial and radial. The axial systems considered are nonpremixed coflow impinging flames and water-laden counterflow flames. The configuration where a radial stagnation plane is established is a tubular counterflow burning condensed fuels. The last system analyzed is the liquid fueled porous wall fed nonpremixed swirl-type tubular flame. The experimental setup and the obtained flame structures as well as stability limits are discussed. A mathematical model that describes the configuration theoretically is proposed and its solution compared to some experimental observations.

1.3 Summary of the Dissertation

This document consists of six chapters. Chapter 1 presents a literature review on the main topics of the dissertation. Important concepts are discussed together with a review of the most relevant research to date on laminar nonpremixed counterflow and tubular configurations. Chapter 2 introduces the fundamentals of the theoretical models used to describe laminar nonpremixed flames. Conservation equations for species, momentum and energy used to predict the flow field, temperature and species profiles based on the a global chemical reaction are presented together with the simplified assumptions considered. The bulk of Chapter 3 is devoted to describe the theoretical model and the procedures employed to obtain the solution to nonpremixed stagnation flow flames. The chapter is

divided into three main sections, each describing a different configuration. In Chapter 4 the experimental setup for nonpremixed swirl-type tubular flames is presented. Details of the overall system behavior are discussed together with some description of the operation conditions. A mathematical model is then presented in Chapter 5 to describe theoretically some of the experimental observations from Chapter 4. The solution to the model is obtained through perturbation theory by combining earlier theoretical models used to describe systems with similar characteristics. In the final chapter, conclusions and suggestions for further developments and improvements in the theoretical models as well as in the experimental setup are presented.

1.4 Laminar Nonpremixed Flames

In this dissertation laminar nonpremixed flames are isobaric systems in which a high temperature reaction zone is produced along a thin region that can be approximated as a surface which is the locus of stoichiometric composition and where the chemical reaction rate is much faster than the rate at which the reactants are supplied by diffusion to it (mixing rate). The theory of nonpremixed combustion was first presented by Burke and Schumann in 1928 [11] who developed a model for hot nonpremixed flames [7]. The model consists of a vertical cylindrical coflow burner in which fuel issues from the inner duct and mixes with the air stream from the outer duct. Upon neglecting heat transport by radiation, streamwise diffusion, Soret and Dufour effects, and assuming uniform gas flow with equal diffusivities of heat and mass (unity Lewis number), an analytical solution to the conservation equations can be obtained. The foundations of the theory of nonpremixed flames were later established by Shvab [14], Zeldovich [15] and Spalding [16] who described the general properties of those flames based on Burke and Schumann's idea of an infinitely thin chemical reaction zone [7].

1.4.1 Counterflow Nonpremixed Flames

Several elementary nonpremixed flame configurations have been proposed to study the overall reaction rates for various combinations of fuel and oxidant, the detailed structure and reaction mechanism of laminar diffusion flames, and the effects of electric field and inhibitors on the structure and reaction of the flame [17]. Ishizuka [18] classified laminar nonpremixed flames into two large groups: the parallel configuration in which a nonpremixed flame is established between two parallel streams of fuel and oxidizer, and the counterflow configuration in which a diffusion flame is established between two opposing streams of fuel and oxidizer. A classical example of the parallel type flame is the Burke-Schumann configuration [11] and the flat flame obtained by the Wolfhard-Parker burner [19]. Flames produced in the parallel configuration are known to have their structure and stability affected by the dead space near the rim of the burner, where the flame is not established due to heat losses to the wall and where a premixture is formed by the interdiffusion of fuel and oxidizer [17]. Parallel flames are also susceptible to buoyancy effects that can be minimized only under very restricted conditions [20]. Moreover, the flame is multidimensional and it is hard to separate physical and chemical effects when the operational conditions are varied.

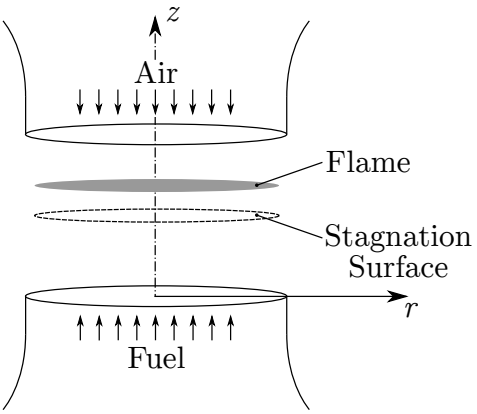

Figure 1.1: Schematic of the nonpremixed counterflow configuration.

Counterflow systems are in the class of similar, axisymmetric stagnation flows. The opposing jet configuration was conceived as a tool to measure chemical reaction rates and

the apparent flame strength (the average mass flow rate of fuel and oxidant per unit area in the central part of the flame at flame extinction) [21]. The counterflow nonpremixed flame is stabilized in the zone of impingement of two directly opposed jets of fuel and oxidizer. A representation of the system is shonw in Fig. 1.1. The physical model with a mathematical description of the experiment was introduced by Spalding [22]. It was soon realized that the conterflow configuration was more suitable as a method for studying flame structure [23] and extinction [24] than high-temperature flame kinetics. It was also noticed that the effect of the burner port on the flow field could alter the flame behavior of the configuration with opposed jets from circular tubes. Nozzles [25], metal matrices [24], and porous-metal [26, 27] burner ports have been proposed and are still of use nowadays. Tsuji and Yamaoka [28, 29, 30, 31] introduced the notion of using a stagnation point flow as an ideal way to study the structure of nonpremixed flames [5]. They experimentally mapped the velocity, temperature and species profiles for a number of fuels and flow conditions using a porous cylinder from which gaseous fuel was ejected radially. In this counterflow configuration, commonly referred as the Tsuji burner, the porous cylinder is subject to a transversal air flow. Systematic computational and experimental studies have been conducted for counterflow nonpremixed flames since Tsuji's seminal review [17].

The study of counterflow nonpremixed flames allowed the description of ignition and extinction phenomena. Integrating numerically the conservation equations for a counterflow nonpremixed flame, Fendell [32] found that the dependence of the maximum temperature on Damköhler number (the ratio of diffusion time to chemical reaction time) becomes S-shaped (three-branched).

1.4.1.1 Condensed Fuel Configuration

In the condensed fuel configuration, a stagnation-point boundary layer flow is established over the vaporizing surface of a pool of liquid fuel. A schematic of the system is shown

in Fig. 1.2. The configuration is applied to the analysis of liquid fuels with high boiling points that do not prevaporize without experiencing thermal breakdown. The systematic analysis of the structure of nonpremixed flames in the stagnation-point boundary layer of a condensed fuel was introduced by Krishnamurthy and Williams [33] in 1974. Their

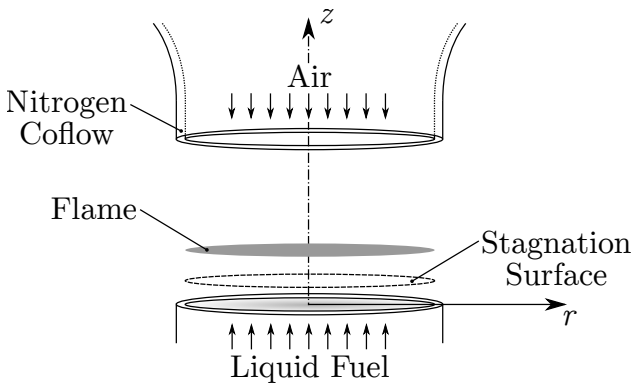

Figure 1.2: Schematic of the nonpremixed liquid-pool counterflow flame.

theoretical model involved the infinitely fast global reaction assumption, with unity Lewis number. The temperature at the condensed phase was assumed known, an assumption often made in problems with a condensed phase pool. A mass transfer number B — introduced by Spalding [34], which characterizes the thermodynamic part of diffusion controlled combustion — up to 10 was considered. It was observed that the flame sheet and the point of maximum velocity move towards the free stream as the transfer number increases due to the increasing fuel mass flux from the surface. The assumption of unity Lewis number in the asymptotic analysis was later relaxed [35]. Based on the theoretical results of [33], an experimental setup was developed to study the structure and extinction of n-heptane, n-decane, n-hexadecane, iso-octane and kerosene in the condensed fuel pool configuration [36]. Thermocouples and gas chromatography were used to measure temperature and concentration on a steady pale blue flame located between 1 mm to 3 mm above the liquid surface. Flame extinguishment was produced either by strain or dilution of the oxidizer with other gases. Extinction was analyzed in the framework of the Damköhler number, which was also used to study experimentally flame structure and

extinction of liquid fuels with [37–40] and without [41–43] the oxidizer mixed with fire suppressants. The overall kinetic parameters of the fuels studied (methanol, heptane, toluene, haptane, benzene, iso-propyl ether, butyl-vinyl ether, methyl methacrylate, poly methyl methacrylate, iso-octane, kerosene, normal alkanes and mixtures of the above) were obtained through an asymptotic technique developed earlier for stagnation point boundary layers [44]. A detailed chemical reaction mechanism and multicomponent transport were used in the comparison between experimental measurements and numerical calculations for heptane [45]. The results were latter compared to numerical solutions obtained with five- and six-step reduced mechanisms [46]. Discrepancies observed on the fuel side of the reaction zone were attributed to inaccuracies in the steady-state concentrations of O and OH. In both condensed heptane studies [45, 46], instead of prescribing the temperature at the liquid surface, a gas-vapor equilibrium was presumed, and interface temperature was calculated through an iterative process. Four- and five-step reduced mechanisms, and prescribed boiling temperature condition, were considered in a methanol flame investigation [47]. The simplified solution was compared with early experimental measurements [38] and a detailed reaction mechanism for a wide range of pressure (1 bar to 10 bar), dilution and preheat temperatures of the oxidizer stream. Flame structure, major species concentrations and extinction conditions for both reduced mechanisms were in good agreement with the detailed mechanism. Higher pressures (up to 3.5 MPa) were considered in a theoretical (unity Lewis number) and experimental [48, 49] study of the extinction characteristics of a condensed heptane pool configuration. A numerical analysis of a hydrogen counterflow diffusion flame above liquid oxygen was used to infer that for cryogenic rocket motors the nonpremixed flame in the wake of the oxygen injector lip cannot be extinguished downstream [50]. More recently, the condensed fuel configuration started being applied to investigate ignition. An activation-energy asymptotic theory that predicts autoignition of condensed hydrocarbon fuels (n-heptane, n-octane, n-decane, n-dodecane, n-hexadecane, iso-octane, cyclohexane, methylcyclohexane, o-xylene, JP-10,

JP-8, and diesel) has been developed [51]. The strain-rate, and the Damköhler number at autoignition were used to obtain the chemical-kinetic rate parameters. The analysis was extended by employing a detailed kinetic model to predict extinction and autoignition of straight-chain alkanes and iso-octane [52]. The experimental analysis of ignition and extinction of low molecular weight esters (methyl butanoate, methyl crotonate, ethyl propionate, biodiesel, and diesel) was used to provide insights on combustion of high molecular weight esters and biodiesel. Critical conditions of extinction and ignition were accurately predicted numerically using a reduced kinetic model for methyl butanoate. The experimental investigation was extended to analyze extinction curves at pressures up to 0.4 MPa [53].

1.4.2 Tubular Nonpremixed Flames

Albeit strained, the flame produced by the counterflow configuration is flat. As a consequence, this configuration does not allow fundamental studies on the influence of curvature effects (unless strong perturbations are induced to the flame [54–59]) or simple rotating flow motion (unless the burner undergoes rigid body rotation [60–64]) on the structure and extinction of nonpremixed flames. In order to evaluate those effects a different elementary system was proposed by Ishizuka in 1984 [65], which is called the tubular configuration.

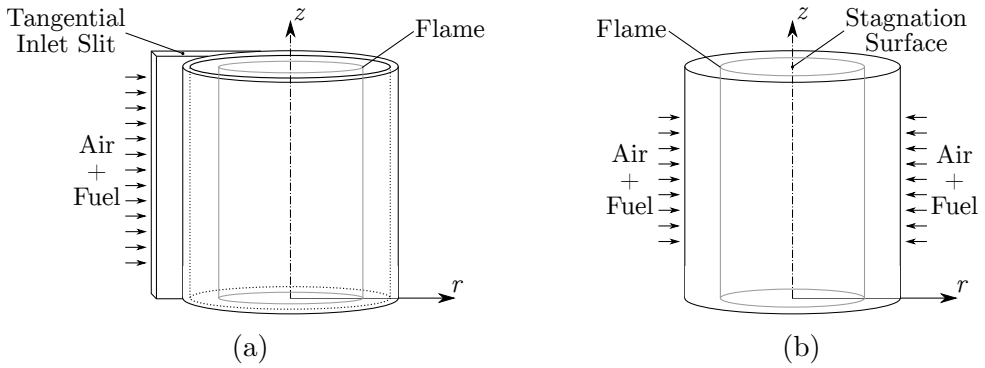

Figure 1.3: Premixed tubular flame configurations. (a) Swirl-type. (b) Counterflow type.

The tubular configuration is one in which a flame circular in cross section and long in the perpendicular direction is established. They experience simultaneously stretch, along the longitudinal direction, and curvature [13]. Tubular flames can be divided into two large groups based on the swirling characteristic of the flow field [18]. The tubular flame in non-rotating flows is formed inside a cylindrical burners with porous walls (Fig. 1.3a) [65] or with radial inlet flow (Fig. 1.3b) [66, 67]. The tubular flame in rotating flows is established in swirl burners [68, 69]. When the rotation speed is small and the pressure variation caused by the circumferential movement is low, the tubular flame with rotation is equivalent to the tubular flame without rotation since the circumferential flow field can be uncoupled and solved separately [70]. However, high swirl rates lead to substantial radial pressure variations [71]. In this case, both pressure variation and the pressure gradient influence the flame response, which is different from the tubular flame without rotation [70]. Nonpremixed tubular flames were obtained only with non-rotating gaseous flow [72], whereas, in rotating flows, a nonpremixed flame has already been established for fuels in condensed phase [73].

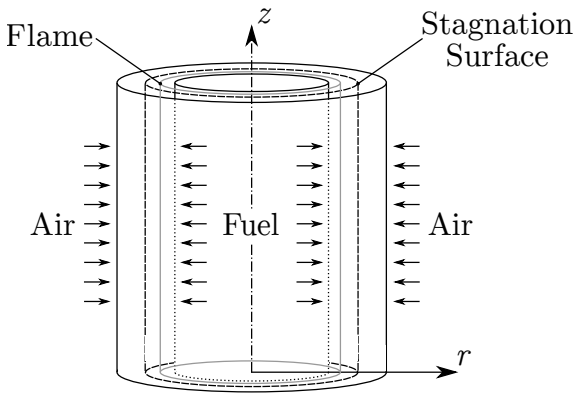

Figure 1.4: Schematic of the nonpremixed counterflow tubular flame.

Non-premixed tubular flames were established using the opposed tubular burner for the first time by Hu et al. [72]. A schematic of the system is shown in Fig. 1.4. A detailed structural investigation using the spontaneous Raman scattering technique was conducted on diluted hydrogen-air flames with constant curvature at various stretch rates. Measured temperature and major species concentrations had a good agreement with the numerical

predictions [72, 74]. It was observed that the curvature of the tubular configuration affects preferential diffusion effects, such that for flames with $Le < 1$, convex curvature promotes combustion, enhances the flame temperature and therefore retards extinction and vise versa for flames with $Le > 1$ [75]. It was also observed that, for Lewis number close to unity, curvature has minimal effects on tubular nonpremixed flames. Extinction of the opposed tubular flames generated by burning diluted hydrogen, methane, and propane with air were investigated for both concave and convex curvature [76]. Several studies on the observation of cellular structures with one to four cells were observed for flames with sufficiently low Lewis number when the flame approaches extinction [76–79]. The characteristics of the cellular instability of opposed nonpremixed tubular flames near the extinction limit were investigated using linear stability analysis and two-dimensional numerical simulations, and the cellular structures dependence on the Damköhler number is replicated in the results [80, 81]. A review on the effects of stretch and curvature on tubular premixed and nonpremixed flames was published recently [70].

A variation of the tubular configuration in which liquid fuels have been applied is known as the liquid film combustor [69, 73]. The concept of condensed fuel film combustors is based on the injection of liquid fuel into the cylindrical combustion chamber in a way that allows the fuel to spread over the inner surface of the chamber's wall. The liquid film vaporizes and becomes the fuel source for the chemical reaction with air that comes from the bottom inlet. The flame is located between the fuel film and the exhaust gas in the center region of the combustion chamber. In early fuel film combustor designs the fuel and air injection were performed tangentially through injectors located at the closed end of the combustion chamber [82]. The tangential air injection creates a swirl movement of the flow field which helps to spread the fuel and stabilize the film on the combustor inner surface [82]. Non-uniformity of the fuel film creates density gradients along the chamber and provides fuel-rich and fuel-lean zones useful for the flame anchor mechanism and establishment [83]. The flame stabilization mechanism requires a balance of several factors such as air strain

on the flame base that does not exceed the maximum flame propagation speed, swirling flow to generate fuel concentration gradients, enhanced heat transfer to the film, a liquid film that remains upstream of the flame anchor point, and a thermally conductive chamber material that permits heat transfer from the flame through the walls and to the film [82]. Research on fuel film combustors has also shown their feasibility and potential as portable power devices [82–86]. Among the several configurations for the film combustor that were attempted the one with secondary injection showed better flame stability when working at overall lean conditions [84]. Based on the secondary injection concept, a new configuration was recently proposed to combine the promising characteristics of different designs [87]. A mathematical model for the system considering unity Lewis numbers was developed to describe theoretically the combustion process in the liquid film burner [88]. Perturbations were used to account for effects of swirl-induced flow, vaporization-induced flow, and gas expansion on an undisturbed plug-flow. For the case of a parabolic velocity profile, the combination of these effects was not taken into account.

The literature on counterflow diffusion flames described above shows that there remains the opportunity for enhanced analytical solutions of nonpremixed counterflow flames. Moreover, it also shows that there are still systems for which both an experimental setup and the theoretical description of the combustion phenomena has not been proposed yet. These analyses are the core effort of this dissertation.

Chapter 2

Conservation Equations for Laminar Nonpremixed Flames

2.1 Introduction

Nonpremixed flames constitute a class of combustion systems in which fuel on oxidizer are not combined before entering the combustion chamber, such that the mixing process has an important role in the system. In this chapter we review the conservation equations and the assumptions used to obtain the flow field, temperature and species profiles in reacting flow with a focus on laminar nonpremixed systems. Although some of what follows in this chapter also appears in the classical combustion literature, it is included to ensure a uniform nomenclature throughout the dissertation and to provide the foundation for the extended and novel analyses presented later.

2.2 Conservation Equations for Reacting Flows

The conservation laws that describe reacting gaseous flows are represented mathematically by the continuity, momentum, energy and species conservation equations. They are given respectively by [89],

$$\frac{D\rho}{Dt} + \rho\nabla \cdot \mathbf{u} = 0 \tag{2.1}$$

$$\rho\frac{D\mathbf{u}}{Dt} = -\nabla p + \nabla \cdot \boldsymbol{\tau} + \rho\mathbf{f} \tag{2.2}$$

$$\rho\frac{DY_k}{Dt} = -\nabla \cdot \mathbf{j}_k + \dot{\omega}_k M_k \tag{2.3}$$

$$\rho\frac{Dh}{Dt} = \frac{Dp}{Dt} + \nabla \cdot \mathbf{q} - \sum_{k=1}^{K} \nabla \cdot h_k \mathbf{j}_k - \sum_{k=1}^{K} h_k \dot{\omega}_k M_k + \Phi \tag{2.4}$$

The independent variable t is the time. The operator $D(\cdot)/Dt$ denotes the material derivate, and $\mathbf{u}$ is the velocity vector. The term $\boldsymbol{\tau}$ is the deviatoric stress tensor and $\mathbf{f}$ represents the acceleration due to body forces acting on the fluid. The mass fraction of each chemical species k is given by Y_k, with $k = 1, ..., K$, where K is the total number of species. The variables ρ, p, h and h_k are the gas density, pressure, enthalpy and the enthalpy of species k, respectively. The term $\dot{\omega}_k$ represents the rate of production of species k per unit mol, and M_k its molecular weight. The vectors $\mathbf{q}$ and $\mathbf{j}_k$ denote the diffusive fluxes of heat and mass, respectively, and Φ the viscous dissipation. The conservation equations can be simplified by noting that, in the systems analyzed, the Mach number is small. In such flows the transport of energy by pressure variations Dp/Dt is small compared to the transport via conduction and convection [5]. Together with these hypotheses, other simplifying assumptions are also considered. Viscous dissipation Φ, which represents the irreversible conversion of kinetic into thermal energy, heat transport by radiation, and the Soret and Dufour effects are neglected in the analysis. Stokes hypothesis is assumed. Fourier's law is used to describe the diffusion of heat. The mass diffusion flux vector is represented by $\mathbf{j}_k = \rho_k \mathbf{U}_k$, in which the components of the diffusion velocity vector of the species k, $\mathbf{U}_k$, in the axial and radial directions are,

respectively, U_k and V_k. Assuming the gaseous mixture as an ideal gas, the state variables of the system are related by,

$$p = \rho R T \sum_{k=1}^{K} \frac{Y_k}{M_k} \tag{2.5}$$

in which R is the gas constant. The systems discussed herein can be described more conveniently in terms of the cylindrical coordinate system. The axysimmetric steady-state form of Eqs. (2.1) to (2.4) can be expressed as,

$$\frac{\partial}{\partial z}(\rho u) + \frac{1}{r}\frac{\partial}{\partial r}(\rho r v) = 0 \tag{2.6}$$

$$\rho\left(u\frac{\partial u}{\partial z} + v\frac{\partial u}{\partial r}\right) = -\frac{\partial p}{\partial z} + \frac{\partial}{\partial z}\left[2\mu\left(\frac{\partial u}{\partial z} - \frac{1}{3}\nabla\cdot\mathbf{u}\right)\right] + \frac{1}{r}\frac{\partial}{\partial r}\left[\mu r\left(\frac{\partial v}{\partial z} + \frac{\partial u}{\partial r}\right)\right] + \rho f_z \tag{2.7}$$

$$\rho\left(u\frac{\partial v}{\partial z} + v\frac{\partial v}{\partial r} - \frac{w^2}{r}\right) = -\frac{\partial p}{\partial r} + \frac{\partial}{\partial z}\left[\mu\left(\frac{\partial v}{\partial z} + \frac{\partial u}{\partial r}\right)\right] + \frac{\partial}{\partial r}\left[2\mu\left(\frac{\partial v}{\partial r} - \frac{1}{3}\nabla\cdot\mathbf{u}\right)\right] + \frac{2\mu}{r}\left(\frac{\partial v}{\partial r} - \frac{v}{r}\right) + \rho f_r \tag{2.8}$$

$$\rho\left(u\frac{\partial w}{\partial z} + v\frac{\partial w}{\partial r} + \frac{vw}{r}\right) = \frac{\partial}{\partial z}\left(\mu\frac{\partial w}{\partial z}\right) + \frac{\partial}{\partial r}\left[\mu\left(\frac{\partial w}{\partial r} - \frac{w}{r}\right)\right] + \frac{2\mu}{r}\left(\frac{\partial w}{\partial r} - \frac{w}{r}\right) + \rho f_\theta \tag{2.9}$$

$$\rho\left(u\frac{\partial Y_k}{\partial z} + v\frac{\partial Y_k}{\partial r}\right) = -\left[\frac{\partial}{\partial z}\left(\rho U_k Y_k\right) + \frac{1}{r}\frac{\partial}{\partial r}\left(\rho r V_k Y_k\right)\right] + M_k\dot{\omega}_k \tag{2.10}$$

$$\rho c_p\left(u\frac{\partial T}{\partial z} + v\frac{\partial T}{\partial r}\right) = \frac{\partial}{\partial z}\left(\kappa\frac{\partial T}{\partial z}\right) + \frac{1}{r}\frac{\partial}{\partial r}\left(\kappa r\frac{\partial T}{\partial r}\right) - \sum_{k=1}^{K}\rho c_{p,k} Y_k\left(U_k\frac{\partial T}{\partial z} + V_k\frac{\partial T}{\partial r}\right) - \sum_{k=1}^{K} h_k M_k\dot{\omega}_k \tag{2.11}$$

The independent variables z, r, and θ denote the spatial coordinates in the axial, radial and circumferential directions, respectively. The position of a point in the spatial domain is represented as (z, r, θ) and the respective components of the velocity vector $\mathbf{u}$ are given as (u, v, w). In Eqs. (2.7) to (2.9), the source terms f_z, f_r and f_θ are the components of the body acceleration vector $\mathbf{f}$ in the directions z, r and θ, respectively. The parameters c_p, μ, and κ are the gas specific heat at constant pressure, dynamic viscosity, and thermal

conductivity, respectively, which, in general, depend on temperature and composition. The term $c_{p,k}$ is the specific heat at constant pressure of species k.

The system of conservation equations in Eqs. (2.7) to (2.11) can be further simplified if the physical model can be described in terms of similarity variables. This simplification reduces the system of partial differential equations into a system of ordinary differential equations. The similarity variables are obtained by special combinations of the spatial coordinates. As described in the next sections, the transformation from the original independent variables into self-similar ones is specific for the each configuration, i.e., it depends on the physics and on the geometry of the system.

2.3 Stagnation Flow Configuration

The stagnation (point) flow configuration represents a physical system in which a fluid flow approaches a stagnation surface. In the region near the surface, the flow changes its direction and a viscous layer develops. The governing equations for this configuration can describe the interaction of the fluid flow with a solid surface as well as with another flow in the opposite direction. Two stagnation surfaces can be represented in term of cylindrical coordinates: one in which the surface is normal to the axial direction, and another one, in which the stagnation surface is parallel to the axial direction. Note that the axial direction is not always the dominant flow direction in these stagnation flows. The stagnation surface can impede either an axial or radial flow while maintaining cylindrical symmetry.

2.3.1 Stagnation Flow in the Axial Direction

This configuration represents a physical system in which a viscous flow oriented axially impinges upon a stagnation surface normal to the axial direction. The formulation can be

represented by considering two different perspectives, depending on how the flow field far from the region near the stagnation surface is described. For an incompressible isothermal viscous flow being impinged on the surface, Homann [90], following Hiemenz [91], proposed an incompressible stream function in the form,

$$\Psi(z, r) \equiv -Br^2 z \tag{2.12}$$

in which B is a constant. By representing the stream function in cylindrical coordinates as,

$$\frac{\partial \Psi}{\partial r} \equiv \rho r u, \qquad \frac{\partial \Psi}{\partial z} \equiv -\rho r v \tag{2.13}$$

which is valid for any axisymmetric flow, and substituting the velocity components into the conservation equation for the momentum in the radial direction, Eq. (2.8), one obtains a third-order ordinary differential equation for which the boundary conditions are given at the stagnation surface and at the inviscid region far from the stagnation point [92]. Therefore, the transformation given in Eq. (2.12) cannot represent flows in which the flow issues from a manifold separated by a finite distance from the stagnation surface [5]. For such flows, the boundary condition needs to be defined at both the manifold and the stagnation surface, and the stream function defined in Eq. (2.12) prevents such description. As an alternative, the stream function Eq. (2.13) can have its dependence on the axial direction modified and it can be written as [93–96],

$$\Psi(z, r) \equiv r^2 U_z(z) \tag{2.14}$$

where $U_z(z)$ is an unspecified function of z. By using the stream function in cylindrical coordinates, Eq. (2.13), the axial and radial velocity components are given as,

$$\rho r u = 2 r U_z, \qquad \rho r v = -r^2 \frac{dU_z}{dz} \tag{2.15}$$

Equations (2.6) to (2.11) are simplified by substituting the expressions from Eq. (2.15) as [95, 96]

$$\frac{d}{dz}(\rho u) + 2\rho V_z = 0 \tag{2.16}$$

$$\frac{dp}{dz} = -\rho u\frac{du}{dz} + \frac{4}{3}\frac{d}{dz}\left(\mu\frac{du}{dz} - \mu V_z\right) + 2\mu\frac{dV_z}{dz} \tag{2.17}$$

$$\rho u\frac{dV_z}{dz} + \rho\left(V_z^2 - W_z^2\right) - \frac{d}{dz}\left(\mu\frac{dV_z}{dz}\right) = -\frac{1}{r}\frac{dp}{dr} = -\Lambda_r \tag{2.18}$$

$$\rho u\frac{dW_z}{dz} + 2\rho V_z W_z = \frac{d}{dz}\left(\mu\frac{dW_z}{dx}\right) \tag{2.19}$$

$$\rho u\frac{dY_k}{dz} = -\frac{d}{dz}\left(\rho U_k Y_k\right) + M_k\dot{\omega}_k \tag{2.20}$$

$$\rho u c_p\frac{dT}{dz} = \frac{d}{dz}\left(\kappa\frac{dT}{dz}\right) - \sum_{k=1}^{K}\rho c_{p,k}U_k Y_k\frac{dT}{dz} - \sum_{k=1}^{K}h_k M_k\dot{\omega}_k \tag{2.21}$$

where Λ_r (the radial pressure gradient) is an eigenvalue of the problem [95, 96]. The scaled radial (V_z) and circumferential (W_z) velocities are given by

$$V_z \equiv -\frac{1}{\rho}\frac{dU_z}{dz} = \frac{v}{r}, \qquad W_z \equiv \frac{w}{r} \tag{2.22}$$

Density ρ, temperature T, axial velocity u, mass fractions Y_k as well as the scaled radial V_z and circumferential W_z velocities are seen to be functions of z alone. The velocity components can be determined from the system composed by Eqs. (2.16), (2.18) and (2.19). Equation (2.17) is used to determine the axial component of the pressure gradient, which is decoupled from the system.

2.3.2 Stagnation Flow in the Radial Direction

In systems in which a viscous flow issues from a manifold oriented radially and impinges on a stagnation surface that is located at a finite distance from, and oriented parallel to, the axial direction, the velocity field can be described in terms of a stream function in the

form [13, 97],

$$\Psi(z,r) \equiv zV_r(r) \tag{2.23}$$

where $V_r(r)$ is an unspecified function of r. The axial and radial components are given as,

$$\rho r u = -z\frac{dV_r}{dr}, \qquad \rho r v = V_r \tag{2.24}$$

The system of conservation equations given in Eqs. (2.6) to (2.11), can be simplified by substituting Eq. (2.24) as [13, 97],

$$\frac{d}{dr}(\rho r v) + \rho r U_r = 0 \tag{2.25}$$

$$\rho v\frac{dU_r}{dr} + \rho U_r^2 - \frac{1}{r}\frac{d}{dr}\left(\mu r\frac{dU_r}{dr}\right) = -\frac{1}{z}\frac{dp}{dz} = -\Lambda_z \tag{2.26}$$

$$-\frac{dp}{dr} = \rho u\frac{\partial v}{\partial r} - \rho\frac{w^2}{r} - 2\frac{d}{dr}\left(\mu\frac{dv}{dr}\right) + \frac{2}{3}\frac{d}{dr}\left[\mu\left(U_r + \frac{1}{r}\frac{d}{dr}(rv)\right)\right] - \frac{2\mu}{r}\left(\frac{dv}{dr} - \frac{v}{r}\right) \tag{2.27}$$

$$\rho v\frac{dw}{dr} + \rho\frac{vw}{r} = \frac{d}{dr}\left[\mu\left(\frac{dw}{dr} - \frac{w}{r}\right)\right] + \frac{2\mu}{r}\left(\frac{dw}{dr} - \frac{w}{r}\right) \tag{2.28}$$

$$\rho v\frac{dY_k}{dr} = -\frac{1}{r}\frac{d}{dr}(\rho r V_k Y_k) + M_k\dot{\omega}_k \tag{2.29}$$

$$\rho v c_p\frac{dT}{dr} = \frac{1}{r}\frac{d}{dr}\left(\kappa r\frac{dT}{dr}\right) - \sum_{k=1}^{K}\rho c_{p,k}V_k Y_k\frac{dT}{dr} - \sum_{k=1}^{K}h_k M_k\dot{\omega}_k \tag{2.30}$$

where Λ_z (the axial pressure gradient) is an eigenvalue of the problem [95, 96]. The scaled axial velocity U_r is given by,

$$U_r \equiv \frac{1}{\rho r}\frac{dV_r}{dr} = \frac{u}{z} \tag{2.31}$$

Density ρ, temperature T, radial velocity v, mass fractions Y_k as well as the scaled axial velocity U_r are seen to be functions of r alone. The velocity components can be determined from the system comprised by Eqs. (2.25), (2.26) and (2.28). Equation (2.27) is used to determine the radial component of the pressure gradient, which is decoupled from the system.

2.3.3 Nonrotating Axisymmetric Stagnation Flows

The governing equations Eqs. (2.16) to (2.21) and Eqs. (2.25) to (2.30) can be expressed as a single system of ordinary differential equations if they are represented in terms of a coordinate system in which the stagnation surface is used as reference. Denoting the coordinates normal and parallel to the surface as ξ and η, respectively, and the respective velocity components as, u_ξ and u_η, the generalized system of conservation equations for nonrotating stagnation point flows in cylindrical coordinates is given as,

$$\frac{d}{d\xi}\left[\rho(2\xi)^\beta u_\xi\right] + \xi^\beta 2\rho U_\eta = 0 \tag{2.32}$$

$$\rho u_\xi \frac{dU_\eta}{d\xi} + \rho U_\eta^2 - \frac{1}{\xi^\beta}\frac{d}{d\xi}\left(\mu\xi^\beta \frac{dU_\eta}{d\xi}\right) = -\frac{1}{\eta}\frac{dp}{d\eta} = -\Lambda_\eta \tag{2.33}$$

$$\rho u_\xi \frac{dY_k}{d\xi} = -\frac{1}{\xi^\beta}\frac{d}{d\xi}(\rho\xi^\beta U_{\xi,k} Y_k) + M_k\dot{\omega}_k \tag{2.34}$$

$$\rho u_\xi c_p \frac{dT}{d\xi} = \frac{1}{\xi^\beta}\frac{d}{d\xi}\left(\kappa\xi^\beta \frac{dT}{d\xi}\right) - \sum_{k=1}^{K} \rho c_{p,k} U_{\xi,k} Y_k \frac{dT}{d\xi} - \sum_{k=1}^{K} h_k M_k \dot{\omega}_k \tag{2.35}$$

in which U_ξ and U_η are the scaled velocities in the normal and parallel directions, and the parameter β equals zero for the axial, and one for radial stagnation flows, respectively. Equations (2.32) to (2.35) show that existing computer programs designed to solve axial stagnation flows (e.g., the algorithms used for reacting flow calculations in CHEMKIN [98] and Cantera [99]) can be easily extended to solve its radial counterpart by the addition of a few terms.

2.3.4 Transport Coefficients

Transport coefficients are parameters that represent diffusive transport processes such as molecular diffusion, thermal conductivity, viscosity and thermal diffusion. In multicomponent systems, such as reacting flows, the transport coefficients need to be

estimated considering all the interacting species. In order to do so, different degrees of approximation can be employed. The multicomponent model, in which the kinetic theory of gases is used to evaluate the transport coefficients, is the most accurate. However, the evaluation of the coefficients requires the solution of linear systems that arise form Galerkin approximations applied to the linearized Boltzmann equation [10], which is computationally expensive. In cases where one species is in excess, mixture-averaged coefficients offers a good compromise between computational cost and satisfactory accuracy [5]. In simplified models, such as asymptotic solutions, transport coefficients for pure species is often used. The temperature dependence of transport parameters in the analyses discussed herein are based on the latter.

The variation of the viscosity of pure species with temperature can be represented in the form of a power law, such as,

$$\frac{\mu}{\mu_0} = \left(\frac{T}{T_0}\right)^m, \qquad 150\,\mathrm{K} \leqslant T \leqslant 500\,\mathrm{K} \tag{2.36}$$

in which, for polyatomic gases, typically $m \approx 0.645$ [5], or the variation can be obtained using the Sutherland formula [100],

$$\frac{\mu}{\mu_0} = \frac{T_0 + T_s}{T + T_s}\left(\frac{T}{T_0}\right)^{3/2}, \qquad 100\,\mathrm{K} \leqslant T \leqslant 1900\,\mathrm{K} \tag{2.37}$$

Assuming constant Prandtl and Lewis numbers, other transport coefficients are obtained using the viscosity calculated from Eqs. (2.36) and (2.37). These formulas are valid for a limited temperature range, even though extrapolations are often used. Only a limited number of species have their Sutherland constants (T_s) tabulated [101]. It is possible to obtain Sutherland's untabulated constants either empirically [102] or, for species for which kinetic-theory parameters are available, though a curve fitting of Sutherland formula.

The Prandtl number, defined as the ratio of momentum diffusivity to thermal diffusivity, is assumed as 0.7 for all models discussed in this study.

2.3.5 Infinitely Fast Chemistry

The chemical transformations in combustion systems can be described in several ways. In general, the reactions occurring in chemically reacting flows can be summarized, in order of increasing complexity as [5]: infinitely fast reactions, chemical equilibrium, reduced reaction mechanisms, and detailed reaction mechanisms. These approaches can be divided into two groups [5]. The first group, comprised of infinitely fast and chemical equilibrium approaches, is characterized by the fast chemistry assumption, i.e., it is assumed that the rate of chemical conversion is not kinetically controlled. The second group consists of reduced and detailed reaction mechanisms. In this group finite-rate chemistry is considered, such that the processes are kinetically controlled. However, a limitation of the finite-rate hypothesis resides in the fact that a large computational effort is required to describe comprehensively the transformations occurring in chemically reacting flows. Finite rate chemistry details are necessary when the goal is to obtain distributions of intermediate or minor species, as might be critical for predicting emissions, for instance. When the objective is focused on heat release, flame shape, and flow coupling dynamics, fast chemistry is often sufficient.

The fast chemistry approximation, also known as the Burke-Schumann limit, is characterized by the assumption of instantaneous reactions, which is valid if the system is mixing controlled, i.e., when the chemical reaction rate is much faster than the mixing rate. This corresponds to a high Damköhler number, a dimensionless parameter defined as the ratio of diffusion time to chemical reaction time. For the chemical equilibrium model, an equilibrium composition is estimated by minimizing the Gibbs free energy of the system. Both infinitely fast and chemical equilibrium models often result in similar model

predictions for major species, provided the overall process is diffusion controlled, but the may fail in predicting concentrations on minor components such as pollutants [5].

The present work aims at describing reactive flows through simple models with a focus on major flame behaviors in unusual stagnation flow geometries. Thus, the analysis performed herein focus on infinitely fast chemistry. The fast chemistry assumption is used solely in the evaluation of the structure of high-temperature steady nonpremixed flames. Extinction cannot be predicted using such an assumption unless a threshold temperature is also considered. In the Burke-Schumann limit the chemical reactions are described by a single one-step irreversible reaction. The infinitely fast conversion of reactants into stable products is assumed to be limited to a very thin exothermic reaction zone — which can be treated as a geometrical surface — where stoichiometric mixing of fuel and oxidizer occurs, and where temperature and combustion products concentrations are maximized. This assumption results in the absence of fuel on the oxidizer side and vice-versa. The combustion process for alkanes (the type of hydrocarbons considered in this study) is represented by the one-step irreversible global reaction,

$$\mathrm{C_nH_{2n+2}} + \frac{3n+1}{2}\left(\mathrm{O_2} + 3.76\mathrm{N_2}\right) \longrightarrow n\mathrm{CO_2} + (n+1)\mathrm{H_2O} + 1.88(3n+1)\mathrm{N_2} \qquad \text{(I)}$$

where the composition for air is assumed as 21 % O_2 and 79 % N_2 by volume. This overall reaction represents with good accuracy the global chemical reaction when the concentrations of the minor species on the products side, such as H_2, OH, CO, H and O, are small compared with those of the main species CO_2 and H_2O. According to Reac. (I), a unit mass of fuel reacts with a mass $s = 8(3n+1)/(7n+1)$ of oxygen, to produce a mass $s_{CO_2} = 22n/(7n+1)$ and $s_{H_2O} = 9(n+1)/(7n+1)$ of carbon dioxide and hydrogen, respectively, with $1 + s = s_{CO_2} + s_{H_2O}$ [4]. An amount q_c of heat is released per unit mass of fuel burnt in the process. From the assumptions, the mass production rate of the species k can be expressed in terms

of an irreversible Arrhenius rate as,

$$\dot{m}_k = M_k \dot{\omega}_k = \nu_k M_k \frac{\rho Y_F}{M_F} \frac{\rho Y_O}{M_O} A \exp\left(-E/RT\right) \tag{2.38}$$

where ν_k is the stoichiometric coefficient of species k, where A and E are the pre-exponential factor and the activation energy, respectively. The subscripts F and O denote fuel and oxidizer, respectively. The conservation equation for species k, Eq. (2.3), can be simplified to,

$$\rho \frac{D\hat{Y}_k}{Dt} = \nabla \cdot \left(\frac{\rho\alpha}{Le_k} \nabla \hat{Y}_k \right) + \frac{\nu_k M_k}{Y_{k,\mathrm{ref}}} \frac{\rho Y_F}{M_F} \frac{\rho Y_O}{M_O} A \exp\left(-E/RT\right) \tag{2.39}$$

where $\hat{Y}_k$ is the nondimensional species mass fraction scaled by a reference value $Y_{k,\mathrm{ref}}$, and α ($\equiv \kappa/\rho c_p$) is the gas mixture thermal diffusivity. The parameters $Le_k \equiv \alpha_k/\mathcal{D}_k$, α_k and $\mathcal{D}_k$ are, respectively, the Lewis number, thermal diffusivity, and mass diffusivity of species k. Adopting a Fickian description for the diffusion velocities, the conservation equations for species Eq. (2.39), for fuel ($\hat{Y}_F$) and oxidizer ($\hat{Y}_O$) scaled mass fractions, and energy, Eq. (2.4), can be written, respectively, as,

$$\rho \frac{D\hat{Y}_F}{Dt} = \nabla \cdot \left(\frac{\rho\alpha}{Le_F} \nabla \hat{Y}_F \right) - \dot{m}_F \tag{2.40}$$

$$\rho \frac{D\hat{Y}_O}{Dt} = \nabla \cdot \left(\frac{\rho\alpha}{Le_O} \nabla \hat{Y}_O \right) - S\dot{m}_F \tag{2.41}$$

$$\rho c_p \frac{D\hat{T}}{Dt} = \nabla \cdot \left(\kappa \nabla \hat{T} \right) + q_c Y_{F,\mathrm{fuel}} \dot{m}_F / T_0 \tag{2.42}$$

where, $\dot{m}_F = \rho^2 \hat{Y}_F \hat{Y}_O A \exp\left(-E/RT\right) Y_{O,0}/M_O$ is the scaled consumption rate of fuel mass per unit volume and $\hat{T} \equiv (T - T_0)/T_0$ is the nondimensional temperature scaled by the its value at the oxidizer inlet, T_0. The reference values used in the definition of the nondimensional mass fractions of fuel and oxidizer are the mass fractions of fuel and oxidizer at their respective inlets, namely, $Y_{F,f}$ and $Y_{O,0}$. The stoichiometric mass ratio is

defined as $S \equiv sY_{F,f}/Y_{O,0}$. An extension to the Shvab-Zel'dovich [14, 15] formulation proposed by Liñán [4, 103–105] is invoked in order to simplify the set of conservation equations. Assuming uniform temperature dependent physical properties for the whole mixture, energy and species conservation equations can be replaced by conservations equations free of source terms for the mixture fraction Z and the excess-enthalpy H given, respectively, as,

$$\rho\frac{DZ}{Dt} = \nabla\cdot\left(\frac{\rho\alpha}{Le}\nabla Z\right) \tag{2.43}$$

$$\rho\frac{DH}{Dt} = \nabla\cdot(\rho\alpha\nabla H) + K\nabla\cdot(\rho\alpha\nabla Z) \tag{2.44}$$

in which the conserved scalars are defined, respectively, as,

$$Z \equiv (S\hat{Y}_F - \hat{Y}_O + 1)/(S+1) \tag{2.45a}$$

$$H \equiv \hat{T}/\gamma + \hat{Y}_F + \hat{Y}_O - 1 \tag{2.45b}$$

in which the heat release $\gamma \equiv q_c Y_{F,f}/c_p T_0(S+1)$. At the flame front, the concentrations of fuel ($\hat{Y}_F$) and oxidizer ($\hat{Y}_O$) are minimized and the flame position can be determined by,

$$Z_S = 1/(S+1) \tag{2.46}$$

The peak flame temperature T_S can be obtained as [4, 106],

$$T_S = T_0 + \gamma Y_{F,f} + (T_f - T_0)/(S+1) \tag{2.47}$$

The Lewis number Le and the parameter K are written as [103–105],

$$Le = \begin{cases} Le_F & \text{for } Z \geqslant Z_S \\ Le_O & \text{for } Z < Z_S \end{cases} \qquad \text{and} \qquad K = \begin{cases} \dfrac{1-Le_F}{Le_F}\dfrac{1}{1-Z_S} & \text{for } Z \geqslant Z_S \\ \dfrac{Le_O-1}{Le_O}\dfrac{1}{Z_S} & \text{for } Z < Z_S \end{cases} \tag{2.48}$$

With the formulation given above, the flame surface is defined by the set of points at which $Z = Z_S$. Due to preferential diffusion effects, non-unity Lewis number, the flame temperature is eventually higher ($Le < 1$) or lower ($Le > 1$) than its adiabatic value.

As described above, the analytical formulation implemented in the following chapters uses the basic classical methods of infinitely-fast chemistry and Schvab-Zel'dovich variables, and then employs an extension to the latter with novel geometric flow self-similarity to solve a set of stagnation and tubular flow combustion problems.

Chapter 3

Stagnation Flow Flames

3.1 Introduction

The stagnation flow configuration has been applied to a variety of reacting systems, such as chemical-vapor-deposition reactors, premixed and nonpremixed counterflow and tubular flames, among others. In this chapter, the theoretical model for nonpremixed flames is presented for systems that can also be described in terms of the governing equations for stagnation flows presented in Chapter 2. Solutions are obtained for the case of infinitely fast chemical reactions. A theoretical model is presented for a novel configuration, identified as an impinging coflow flame, and its solution is obtained semi-analytically. Two nonpremixed opposed flow systems are then discussed. The first one is a classical counterflow flame, but studied under water-laden fuel conditions. Finally, the mathematical model for the tubular counterflow flame configuration is extended and solved for the case of condensed fuels delivered through porous walls.

3.2 Impinging Coflow Flames

Flame impingement heating is a well-established technique that has been widely used and studied for many years. Typical applications include melting of scrap metal, shaping glass and heating metal bars. Fabrication and assembly applications include soldering, brazing, cutting and welding [107]. In industrial furnaces the use of direct flame impingement significantly enhances the convective heat transfer rates from combustion products to the load, increasing productivity, reducing fuel consumption and lowering pollutant emission [107]. Several semi-analytical solutions have been proposed for calculating the structure and heat flux of impinging flames, and a number of reviews are available describing further details of the solutions [107–110].

The majority of the work on the analysis of impinging flames is devoted to the study of premixed flames. Both laminar and turbulent premixed flames have been investigated. Impinging jets are considered to be laminar up to Reynolds numbers of approximately 2500 [108]. Earlier descriptions of premixed impinging flames, as those from Sibulkin [111], Fay and Riddell [112], Rosner [113] and, most recently Remie et al. [114], developed equations to compute the structure and heat flux at the stagnation point of an axisymmetric surface subject to a uniform, external, steady flow. Sibulkin [111] described the heat flux near a stagnation point that was obtained by numerically solving the laminar boundary layer equations of an impinging jet. Lees [115] analyzed the laminar heat-transfer problem in dissociated air, using the boundary layer equations considering equilibrium and diffusion controlled regimes to obtain expressions for the heat transfer coefficients for both cases. Fay and Riddell [112] later extended the semi-analytical solutions from Sibulkin [111] and Lees [115] by taking into account the recombination of radicals in the boundary layer. More recently, numerical models have been applied to study impinging jet flames. Liakos et al. [116] evaluated the effects of the reacting mixture pressure and angle of impingement of a turbulent premixed jet flame impinging on a solid surface using a numerical code. Malikov

et al. [117] used a simplified two-dimensional numerical simulation of a reactive jet to study heat and mass transfer in a direct flame impingement system and compared their results with experimental data from a furnace. Liakos et al. [118] developed a numerical model of a premixed turbulent jet impinging on a plane wall using the k-ϵ model and the RNG k-ϵ model to calculate heat release, local extinction effects and radiative heat transfer. The numerical results were compared with experimental data from the literature. Remie et al. [114] derived an analytical expression for the heat flux of a laminar flame impinging on a flat plate with flame jet approximated by a hot inert jet. Their analytical expressions are based on an isothermal plug flow concept for the flame jet valid for radial distances $r < R$ and nozzle-tip distances $z < 2R$. Remie et al. [119] extended their analytical solution to predict the complete heat-transfer distribution to a flat target. In a subsequent work, Remie et al. [120] modified their analytical results based on the numerical solution from a commercial CFD software.

Despite the fairly rich research in premixed flames, the impinging nonpremixed flames literature is sparse. In some experimental and numerical analyses of premixed flames, the inner conical rich premixed flame produced by a Bunsen burner is incidentally surrounded by an outer nonpremixed flame [121, 122], but the nonpremixed flame is not the focus of the work. Coflow systems have also been applied, but the work was limited to the experimental and numerical study of premixed and partially premixed flames [123]. More recently, Dong et al. [124] presented an experimental investigation of inverse nonpremixed flames. They compared their measurements of the heat flux at the stagnation plate with the semi-analytical solution from Fay and Riddell [112]; however, no qualitative agreement was observed, mainly because of the different flow regimes for relatively low Reynolds numbers (1500) in the inverse nonpremixed flame analyzed. It appears that the works of Chien et al. [125–127] are the first experimental studies on impinging nonpremixed flames. In the course of their study of electric field effects on nonpremixed flames, they investigated the effect of a stagnation plate on the structure of a nonpremixed coflowing reacting jet of air and methane. In order

to provide a theoretical background to their system, a semi-analytical model was proposed by Sauer and Dunn-Rankin [128, 129], with which, using simplifying assumptions, the flame position can be obtained.

The theoretical model proposed by Roper et al. [12, 130] for coflow nonpremixed flames — a modified version of the Burke-Schumann's nonpremixed flame [11] — assumes that axial velocity u, temperature T and species mass fractions Y_k are functions of the axial direction only. Sunderland et al. [131] extended Roper's model to predict complete flame shapes assuming uniform velocity and temperature throughout the flame with a formulation they called the Extended Roper model [132]. Sauer and Dunn-Rankin [129] proposed an extension of the model developed by Sunderland et al. [131] to study impinging coflow flames. In order to determine the velocity field of the system, a stagnation point viscous flow for incompressible fluids between stationary porous plates [93–96] and the Extended Roper model (ER) are used to obtain the flame shape. The conservation equations of the model can also be transformed using streamline coordinates; an approach called the Stream Function as a Coordinate (SFC), introduced by von Mises in 1927 [133]. The transformation of coordinates of the conservation equations from the axial and radial coordinates into another system (in which the equations present a simpler form) was also performed by Li et al. [134] and Vázquez-Espí [135] to study coflow flames. They analyzed an axisymmetric laminar jet nonpremixed flame in unconfined coflowing air using a boundary-layer description applying the von Mises [133] approach. The use of SFC simplifies the conservation equations by using the stream function as one of the independent coordinates and the axial direction as the other. The second approach included here to analyze impinging coflow nonpremixed flames is based on the von Mises transformation. The conservation equations are transformed using the SFC model from which the flame shape and height are determined.

3.2.1 Experimental Observations

The theoretical model for nonpremixed impinging flame is based on the experiment represented in the schematic in Fig. 3.1 which is described in detail in [125–127]. Although the system was used for other work, as identified in the references, specific measurements for inclusion in this dissertation were taken to focus on the key features of comparison needed for validating the analytical approach. The system is composed of a vertical cylindrical coflow burner and stainless steel plate that acts as the impinging surface. The radius of the inner tube, from which methane is issued, is $r_F = 2\,\text{mm}$, the radius of the outer tube, from which air is supplied to the system, is $r_O = 25.4\,\text{mm}$.

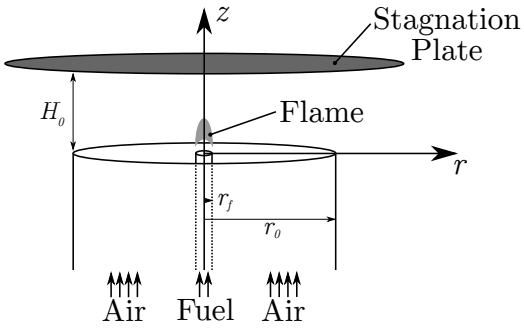

Figure 3.1: Representation of the physical system.

The flow from the outer tube is made uniform by a bed of beads and a honeycomb mesh positioned at the burner port. The inner tube does not have any stabilizing strategy, such that the velocity profile of the fuel at the burner port is fully developed and laminar. Both fuel and air are issued at a constant nominal velocity of $20\,\text{cm}\,\text{s}^{-1}$. The plate is a 1.5 mm thick stainless steel square with 10.2 mm sides. The impinging surface is allowed to move vertically and its position is adjusted by a translation stage. For the conditions described, the overall flame luminosity (mainly due to exited-state CH and OH radicals) was imaged at different positions using an intensified EMCCD camera with resolution of 512 x 512 pixels. The flame position is determined as the locus of maximum luminous intensity. An Abel transform is used for image deconvolution and the resulting data is filtered to reduce the

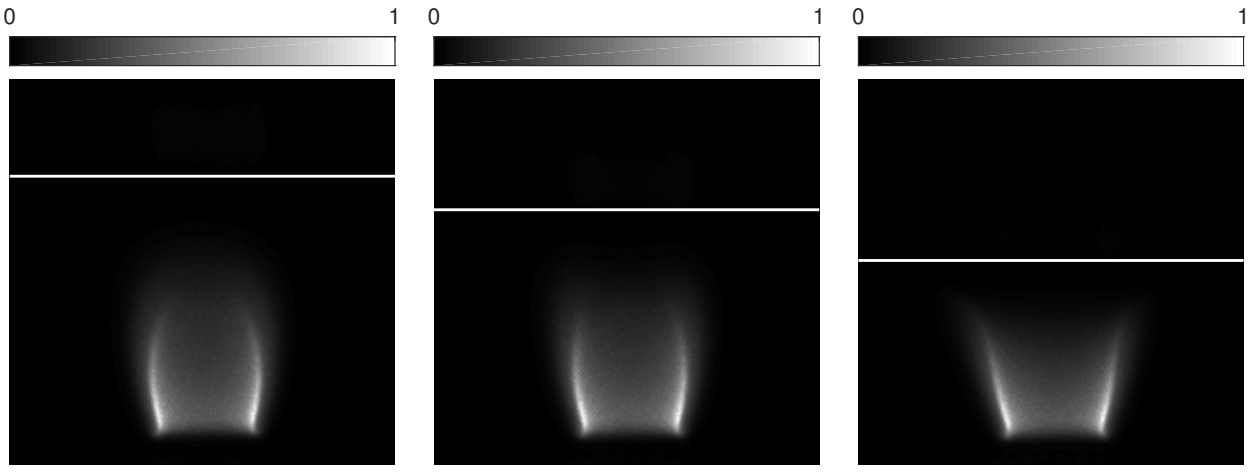

(a) (b) (c)

Figure 3.2: Photographic images of the flame with the stagnation plate at different vertical positions. (a) $H_0 = 10.6\,\text{mm}$; (b) $H_0 = 9.4\,\text{mm}$; (c) $H_0 = 7.5\,\text{mm}$. The horizontal white line represents the bottom surface of the impinging plate.

remaining noise. In order to apply the transform, a set of images of the steady flame is averaged over time, and the background noise from the camera removed by using pictures from the system without any ambient light. Photographic images of the flame luminosity scaled by its maximum intensity are shown in Fig. 3.2. The images show the different flame shapes observed when the impinging plate is positioned at three different vertical distances from the burner port. As the plate is moved closer to the flame, the luminous core transitions from an open-tip into a closed-tip structure.

3.2.2 Theoretical Model

The models through which the system is represented are described in terms of a semi-infinite axisymmetric domain following the schematic in Fig. 3.1. The inlets are located at the r-axis. Fuel flows from the inner tube of radius r_f (diameter D_f) and mixes with the air stream from an outer tube of radius r_0 (diameter D_0). The flat plate acting as a stagnation surface is kept at a finite distance H_0 from the burner port. The outer tube and the plate diameters are assumed sufficiently large compared with the maximum flame radius, so that edge effects

do not disturb the coflowing stream near the flame. Inflow velocities and temperature of air and fuel streams are equal and represented by u_0 and T_0, respectively. The inlet mass fractions of fuel and oxidizer at their respective inlets are represented by $Y_{F,f}$ and $Y_{O,0}$, and the flame position is represented by Z_S. The chemical reactions are described by the single one-step irreversible reaction from Reac. (I). Buoyancy effects are neglected in the analysis. The formulation from Section 2.3.5 is invoked in order to simplify the set of conservation equations, by assuming equal diffusivities of heat and mass, i.e., unity Lewis number, which allows energy and species conservation equations to be replaced by a conservation equation for the mixture fraction Z, given by Eq. (2.44).

3.2.2.1 Axisymmetric Stagnation Flow

The velocity field is described in terms of the conservation equations for axial stagnation flows, namely, Eqs. (2.16) to (2.18). These conservation equations are nondimensionalized in order to simplify the evaluation and generalize the conclusions to systems with similar structure as influenced by the same dimensionless parameters. Assuming a nonrotating axisymmetric flow with constant uniform properties, the dimensionless continuity and radial momentum equations are given, respectively, as,

$$\frac{d\hat{u}}{d\hat{z}} + 2\hat{V}_z = 0 \tag{3.1a}$$

$$\hat{u}\frac{d\hat{V}_z}{d\hat{z}} + \hat{V}_z^2 = -\hat{\Lambda}_r + \frac{1}{Re}\frac{d^2\hat{V}_z}{d\hat{z}^2} \tag{3.1b}$$

where $\hat{z} \equiv z/H_0$ and $\hat{r} \equiv r/H_0$ are the independent variables scaled by the distance between the burner port and the stagnation surface H_0. The term $\hat{u} \equiv u/u_0$ is the velocity component in the axial direction scaled by the uniform value at the inlet u_0, and $\hat{V}_z \equiv H_0 V_z/u_0$ is the nondimensional scaled velocity in the radial direction, where V_z is given as in Eq. (2.22). The Reynolds number and the dimensionless eigenvalue are given, respectively, by $Re \equiv H_0 u_0/\nu_0$

and $\hat{\Lambda}_r \equiv \Lambda_r H_0^2/\rho_0 u_0^2$, where the constants ρ_0 and ν_0 represent the gas density and kinematic viscosity, respectively. The boundary conditions required to solve the system of equations are given by,

$$\hat{u} - 1 = \hat{V}_z = 0, \quad \hat{z} = 0 \tag{3.2a}$$

$$\hat{u} = \hat{V}_z = 0, \quad \hat{z} = 1 \tag{3.2b}$$

3.2.2.2 The Extended Roper Model

Roper [12] considered the following assumptions to predict the flame length:

1. Temperature and axial velocity are allowed to vary in the axial direction but are constant at each z location, i.e., they are functions of z but not r;
2. Combustion causes no change in the number of molecules;
3. Axial diffusion is neglected;
4. The momentum, mass and thermal diffusivity are equal;
5. The effects of radiation are not integral to the model but the first assumption allows them to be considered approximately.

As a consequence of the first assumption — which is also valid for the SFC model — body forces such as buoyant acceleration effects [132] and forces due to the presence of electric or magnetic field can be accounted for by the model. The assumptions in the Roper model were originally conceived to predict flame height [12]. Therefore, hypothesis 1 to 5 are not perfectly suited for determining flame shapes, and some modifications are required for better qualitative predictions [132].

The steady-state conservation equations for species k, Eq. (2.20), can be combined into a conservation equation for the mixture fraction Z free of source terms, Eq. (2.44). Considering the third assumption, the conservation equation for the mixture fraction can be simplified as [136],

$$u(z)\frac{\partial Z}{\partial z} + v(r)\frac{\partial Z}{\partial r} = \frac{\mathcal{D}}{r}\frac{\partial}{\partial r}\left(r\frac{\partial Z}{\partial r}\right) \tag{3.3}$$

where, from the first assumption, the velocity components $u(z)$ and $v(r)$ are functions of z and r, respectively, and Z is allowed to vary in both axial and radial directions. The following transformations are used in order to determine the position of the flame sheet,

$$t \equiv \int_0^z \frac{dz}{u}, \quad \xi(r,z) \equiv \frac{r}{r_D(z)}, \quad \frac{d\ln r_D}{dt} \equiv \frac{v}{r}, \quad \theta \equiv \mathcal{D}\int_0^t \frac{dt}{r_D^2} \tag{3.4}$$

in which t and r_D are, respectively, the residence time on the flame axis and the characteristic length of diffusion [136]. Substituting Eq. (3.4) into Eq. (3.3),

$$\frac{\partial Z}{\partial \theta} = \frac{1}{\xi}\frac{\partial}{\partial \xi}\left(\xi\frac{\partial Z}{\partial \xi}\right) \tag{3.5}$$

which is subject to the boundary conditions,

$$Z(0,\xi) = 1, \quad 0 \leqslant \xi \leqslant 1 \tag{3.6a}$$

$$Z(0,\xi) = 0, \quad \xi > 1 \tag{3.6b}$$

Both sides of Eq. (3.5) are functions of only one independent variable, thus its solution can be found by a separation of variables in the form,

$$Z(\theta,\xi) = \Theta(\theta)R(\xi) \tag{3.7}$$

which can be substituted into Eq. (3.5), yielding,

$$\frac{1}{R}\left(\frac{d^2R}{d\xi^2}+\frac{1}{\xi}\frac{dR}{d\xi}\right)=\frac{1}{\Theta}\frac{d\Theta}{d\theta}=-\lambda^2 \tag{3.8}$$

The solution for the direction θ is obtained by integrating the equation for $\Theta(\theta)$ as,

$$\Theta(\theta)=c_1\exp\left(-\lambda^2\theta\right) \tag{3.9}$$

where c_1 is a constant of integration. The left hand side of Eq. (3.8), which is in Sturm-Liouville form, is the Bessel differential equation of order zero for $R(\xi)$. Its solution is given by,

$$R(\xi)=c_2J_0(\lambda\xi) \tag{3.10}$$

where J_0 is the Bessel function of the first kind of order zero, which is bounded at $\xi=0$. The solution of $Z(\theta,\xi)$ is integrated over all positive values of λ, yielding,

$$Z(\theta,\xi)=\int_0^\infty c(\lambda)\exp\left(-\lambda^2\theta\right)J_0(\lambda\xi)d\lambda \tag{3.11}$$

The boundary condition at the burner port is used to determine the coefficients $c(\lambda)$. At $\theta=0$ Eq. (3.11) becomes,

$$Z(0,\xi)=\int_0^\infty c(\lambda)J_0(\lambda\xi)d\lambda \tag{3.12}$$

which is the Fourier-Bessel expansion of the function $Z(\xi,0)$, for which $c(\lambda)$ are given by,

$$c(\lambda)=\lambda\int_0^\infty \xi' J_0(\lambda\xi')Z(\xi',0)d\xi' \tag{3.13}$$

Substituting Eq. (3.13) into Eq. (3.11) yields,

$$Z(\theta,\xi)=\int_0^\infty\left[\lambda J_0(\lambda\xi)\exp\left(-\lambda^2\theta\right)\int_0^\infty\xi' J_0(\lambda\xi')Z(0,\xi')d\xi'\right]d\lambda \tag{3.14}$$

Rearranging the order of integration and simplifying [137],

$$Z(\theta,\xi)=\frac{1}{2\theta}\exp\left(-\frac{\xi^2}{4\theta}\right)\int_0^1\xi'\exp\left(-\frac{\xi'^2}{4\theta}\right)I_0\left(\frac{\xi\xi'}{2\theta}\right)d\xi' \tag{3.15}$$

I_0 denotes the modified Bessel function of the first kind of order zero. Equation (3.15) is called the P-function [134, 137, 138]. Conversion from transformed coordinates (θ,ξ) into dimensionless physical coordinates $(\hat{z},\hat{r})$ is given by the following expressions,

$$\hat{z}=\frac{u_0 r_f^2}{H_0}\frac{1}{\mathcal{D}_0}\left(\frac{T_0}{T_S}\right)^m\theta \tag{3.16a}$$

$$\hat{r}=\frac{r_f}{H_0}\left(\frac{u_0}{u}\frac{T_S}{T_0}\right)^{0.5}\xi \tag{3.16b}$$

where $\mathcal{D}_0$ is a reference mass diffusivity, T_S is a constant temperature in the flame region [12], and the exponent m is due to dependence of the viscosity μ being approximated by the power law expression from Eq. (2.36).

3.2.2.3 Stream Function as a Coordinate (SFC) Model

The stream function from Eq. (2.15) defines the flow streamwise direction. Using the von Mises transformation [133], i.e., defining,

$$\zeta=\hat{z} \tag{3.17a}$$

$$\eta=\hat{\Psi}(\hat{z},\hat{r}) \tag{3.17b}$$

and assuming that the diffusion of heat and mass in the streamwise direction is negligible, the conservation equation for the coupling function Z, Eq. (2.44), can be simplified by substituting the partial derivatives for $\hat{r}$ and $\hat{z}$ by the transformed coordinates as,

$$\frac{\partial}{\partial \hat{r}} = \hat{\rho}\hat{r}\hat{u}\frac{\partial}{\partial \eta} \tag{3.18a}$$

$$\frac{\partial}{\partial \hat{z}} = \frac{\partial}{\partial \zeta} - \hat{\rho}\hat{r}\hat{v}\frac{\partial}{\partial \eta} \tag{3.18b}$$

yielding,

$$\frac{\partial Z}{\partial \zeta} = \frac{1}{Pe}\frac{\partial}{\partial \eta}\left(\hat{\rho}\hat{\mathcal{D}}\hat{u}\hat{r}^2\frac{\partial Z}{\partial \eta}\right) \tag{3.19}$$

where the Peclét number is defined as $Pe \equiv u_0 H_0/\mathcal{D}_0$, $\hat{\rho} \equiv \rho/\rho_0$ is the scaled density, and $\hat{\mathcal{D}} \equiv \mathcal{D}/\mathcal{D}_0$ is the scaled mass diffusivity. The assumption of negligible diffusion in the streamwise direction is valid if the convective transport along the streamlines is large compared to the diffusive transport [139]. Equation (3.19) can be further simplified using Eqs. (2.14) and (2.15) to give,

$$\frac{\partial Z}{\partial \zeta} = \frac{2}{Pe}\frac{\partial}{\partial \eta}\left(\eta\frac{\partial Z}{\partial \eta}\right) \tag{3.20}$$

which is subject to the boundary conditions,

$$Z(0,\eta) = 1, \quad 0 \leqslant \eta \leqslant \eta_f \tag{3.21a}$$

$$Z(0,\eta) = 0, \quad \eta > \eta_f \tag{3.21b}$$

where η_f represents the transformed dimensionless inner duct radius. Assuming constant uniform properties ($\hat{\rho} = \hat{\mathcal{D}} = 1$), and noting that Eq. (3.20) has the same form as Eq. (3.5), its solution is found using the same procedure discussed in Section 3.2.2.2, and it is given

by,

$$Z(\zeta,\eta) = \frac{Pe}{2\zeta}\exp\left(-Pe\frac{\eta}{2\zeta}\right)\int_0^{\eta_d}\exp\left(-Pe\frac{\eta'}{2\zeta}\right)I_0\left(Pe\frac{\sqrt{\eta\eta'}}{\zeta}\right)d\eta' \tag{3.22}$$

Conversion from transformed coordinates (ζ,η) into dimensionless physical coordinates $(\hat{z},\hat{r})$ is given by the following expressions,

$$\hat{z} = \zeta \tag{3.23a}$$

$$\hat{r} = \left(\frac{2\eta}{\hat{u}}\right)^{1/2} \tag{3.23b}$$

3.2.3 Discussion

The mixture fraction field of a nonpremixed methane-air flame is obtained using ER and SFC models. The axisymmetric stagnation flow for a finite gap is used to obtain the constant temperature velocity field between the burner port and the stagnation plate surface. The system parameters, based on the experiment, are $T_0 = 298\,\mathrm{K}$ and $m \simeq 0.67$. The flame is located at the position where Eq. (2.46) is satisfied, i.e., at the locus where the mixture is stoichiometric. For methane-air flames the stoichiometric value of the mixture fraction on a mass basis, Z_S, is 0.055. For the Roper Model the coupling function is defined on a molar basis, following [12], and its stoichiometric value is 0.095. The solution of the stagnation point flow equations is obtained via a FORTRAN code. The FORTRAN BVP_SOLVER [140] subroutine is used to solve the system of ordinary differential equations, Eqs. (3.1a) and (3.1b). The integrals, Eqs. (3.15) and (3.22), are calculated using the FORTRAN QUADPACK [141] subroutine.

3.2.3.1 Velocity Field

Classically, the viscous flow field in an incompressible isothermal impinging system, represented schematically in Fig. 3.3, is divided into three zones: the free jet, the stagnation and the wall jet regions [109]. The free jet region is characterized by a potential

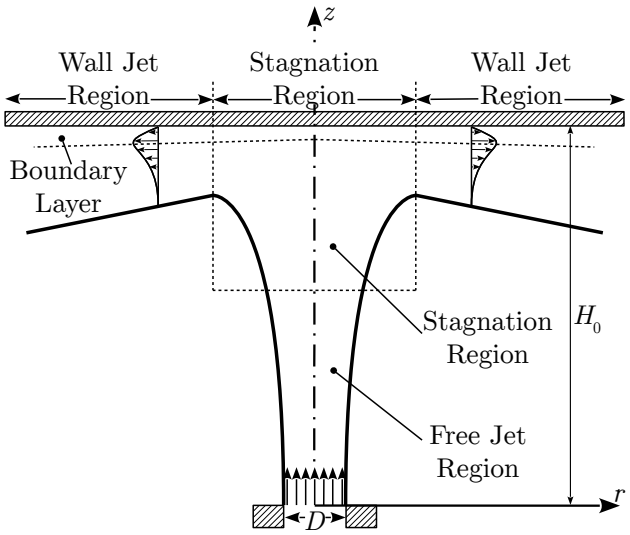

Figure 3.3: Flow zones in an impinging system (adapted from [109]).

core zone, in which the axial velocity profile remains approximately constant; a developing flow region, in which the axial velocity starts to decay; and a developed flow region, in which the velocity profile is fully developed [108]. The free jet region is an outer inviscid and rotational layer which extends from the burner port to the boundary of the stagnation region, where the tangential component of the flow velocity vanishes. The stagnation region is characterized by a turning of the jet in the radial direction and approximately constant thickness. It consists of an inner viscous flow layer near the plate surface, which extends slightly bellow the stagnation plane. The wall jet region is characterized by a bulk flow in the outward radial direction.

The computed velocity profiles for three different Reynolds numbers are shown in Fig. 3.4. It is observed that $d\hat{V}_z/d\hat{z}$ is approximately constant from $\hat{z} = 0$ to $\hat{z} \simeq 0.8$ for Reynolds numbers of order 10^2 or greater, which is the case of the flows analyzed. In that region,

advective (convective) terms should prevail over the diffusion terms in the conservation equations. This limit defines the thickness of the viscous (inner) layer and the inviscid (outer) layers. Therefore, in the outer region, the assumption of negligible streamwise diffusion is valid.

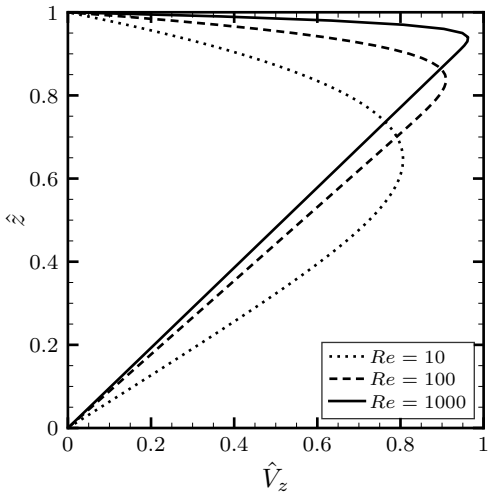

Figure 3.4: Nondimensional scaled velocity profiles for Reynolds numbers 10, 100 and 1000.

3.2.3.2 Model Validation

The axisymmetric flame contour for a methane-air flame for both the ER model and the SFC model in the $\hat{z}\hat{r}$ plane are presented in Fig. 3.5. The flame position obtained experimentally is also shown. The full width at half maximum (FWHM) of the experimental measurements is shown as a shaded area in Fig. 3.5 and represents uncertainty in the measurements.

The results for the ER model are obtained considering the constant temperature in the flame region as $T_S = 1500\,\mathrm{K}$ [130]. In the SFC model the reference diffusion coefficient, which, following [142], is treated as an adjustable parameter, is evaluated at 750 K. We observe from Fig. 3.5 that both models represent qualitatively well the overall flame shape. The flame shape obtained through the ER model is wider than the solution obtained using the SFC model for all conditions analyzed. The difference is due to the approach considered in the ER model to account for the variation of physical properties with temperature from

the burner port to the flame region. The flame shapes obtained using the SFC model present qualitatively good agreement with the shapes obtained experimentally for the three separation distances presented, particularly given the simplifying assumptions in the model.

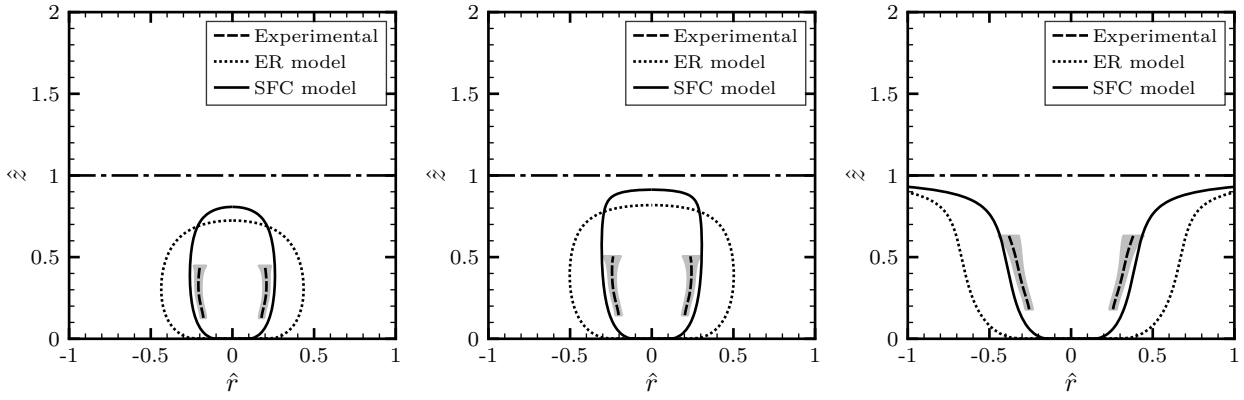

Figure 3.5: Experimental and calculated flame location with the stagnation plate at different vertical positions. Dotted line: ER model. Solid line: SFC model. Dashed line: Region of maximum luminous intensity obtained experimentally. Shaded area: FWHM of the maximum luminous intensity obtained experimentally. a) $H_0/D_f = 5.3$ ($H_0 = 10.6\,\text{mm}$); (b) $H_0/D_f = 4.7$ ($H_0 = 9.4\,\text{mm}$); (c) $H_0/D_f = 3.75$ ($H_0 = 7.5\,\text{mm}$). The long-dash-dot line at $\hat{z} = 1$ represents the stagnation plane.

In the present analysis, an insulating inert wall is assumed. However, in real systems, the gaseous components can interact with the solid surface through heat or mass transfer, for example, if heat conduction through the stagnation plate or destruction of active radicals at the stagnation surface are considered. Thus, the models developed herein need to be extended if some of the neglected physics or chemistry phenomena are to be included in the analysis. For flame shape, however, the results of the simplified model already capture the key behaviors.

3.2.3.3 Effect of Separation Distance on Flame Tip Opening

The flame shape transitions from a closed tip to an open tip configuration as the separation distance between the stagnation plane and the burner port is varied. The tip opening can

be observed in Fig. 3.5 as the stagnation plane moves downward, with H_0/D_f going from 3.75 to 4.7. Consequently, there exists a relationship between the separation distance H_0 and the maximum flame height. Both the ER model and the SFC model are able to predict the flame tip opening phenomenon.

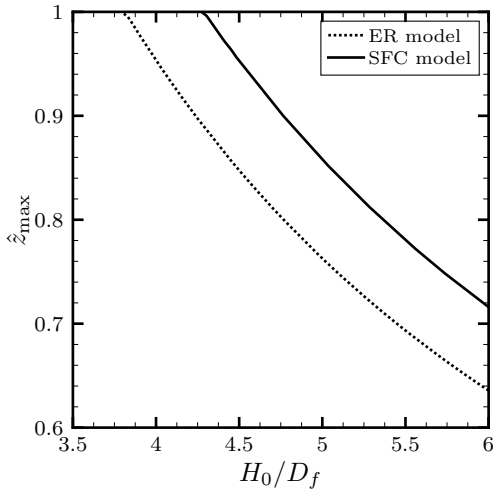

Figure 3.6: Maximum flame height obtained using ER and SFC models.

In a classical Burke-Schumann problem, it is possible to obtain a closed form solution for the maximum height of the flame, since, in the case of an overventilated flame, the tip is expected to close at the axis of symmetry. However, in the present case it is not possible to express the flame height in terms of a simple analytical function for all the separation distances, because the solution for the velocity field is obtained through the numerical solution of the system of ordinary differential equations given by Eq. (3.1b). The same is true for the stagnating plate distance at which flame tip opening is observed. The semi-analytical nature of the solutions for the flame shape allows determination of the maximum flame height at several separation distances and ploting them as a function of the distance between the burner port and the stagnation plate as shown in Fig. 3.6.

The lines in Fig. 3.6 represent several positions of the maximum flame height $\hat{z}_{\max}$ at the axis of symmetry. The heights are determined recording the positions in the $\hat{z}$ axis where the coupling function has its stoichiometric value. The ER model predicts flame opening

at slightly lower separation distance compared to the SFC model. From the experimental results in Fig. 3.5, the position at which the flame opens seems to be accurately predicted by both models. The ER model predicts flame tip opening at $H_0/D_f = 3.8$, and the SFC model, at $H_0/D_f = 4.3$.

3.2.3.4 Temperature and Mass Fraction Fields

The first assumption considered in the theoretical model proposed by Roper [12], namely the hypothesis that temperature is allowed to vary only in the axial direction, prevents the ER model from predicting the temperature field in any coflow system. On the other hand, in the SFC model no assumptions are made with respect to the spatial variation of temperature or concentration of species. Contours of the nondimensional temperature field and mass fractions are presented, respectively, in Figs. 3.7 and 3.8 for the SFC model.

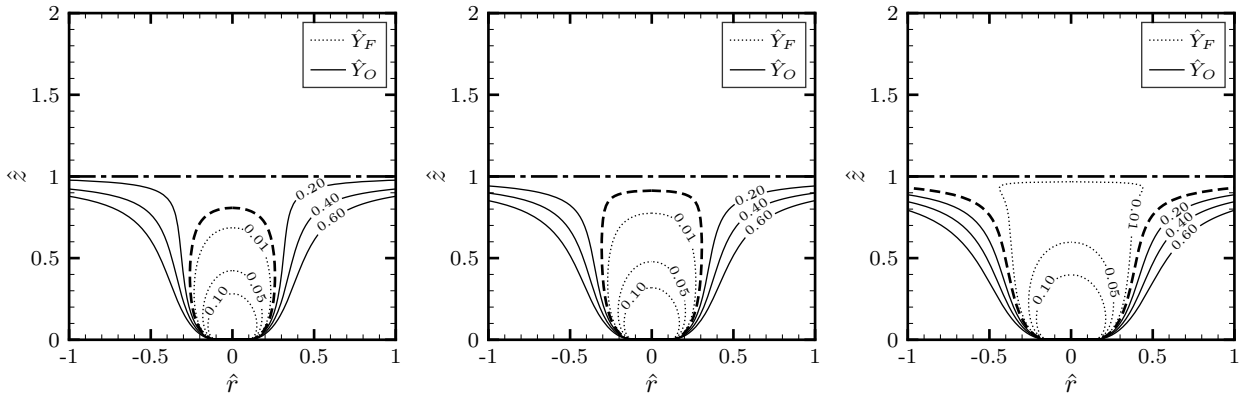

Figure 3.7: Contours of dimensionless mass fraction fields. The dashed line represents the flame sheet. a) $H_0/D_f = 5.3$ ($H_0 = 10.6\,\text{mm}$); (b) $H_0/D_f = 4.7$ ($H_0 = 9.4\,\text{mm}$); (c) $H_0/D_f = 3.75$ ($H_0 = 7.5\,\text{mm}$). The long-dash-dot line at $\hat{z} = 1$ represents the stagnation plane.

The flame position, obtained as the location where the mixture fraction satisfies Eq. (2.46), is highlighted. In Fig. 3.8 the contour levels represent the nondimensional temperature. Dimensionless mass fractions of fuel ($\hat{Y}_F$) and oxidizer ($\hat{Y}_O$) are represented in Fig. 3.7 by continuous and dotted lines, respectively, in their respective sides. Experimental results are

not available for the validation of those profiles. However, based on the results obtained by the SFC model for the flame position presented in Section 3.2.3.2 the profiles observed in Figs. 3.7 and 3.8, are expected to predict qualitatively experimental observations.

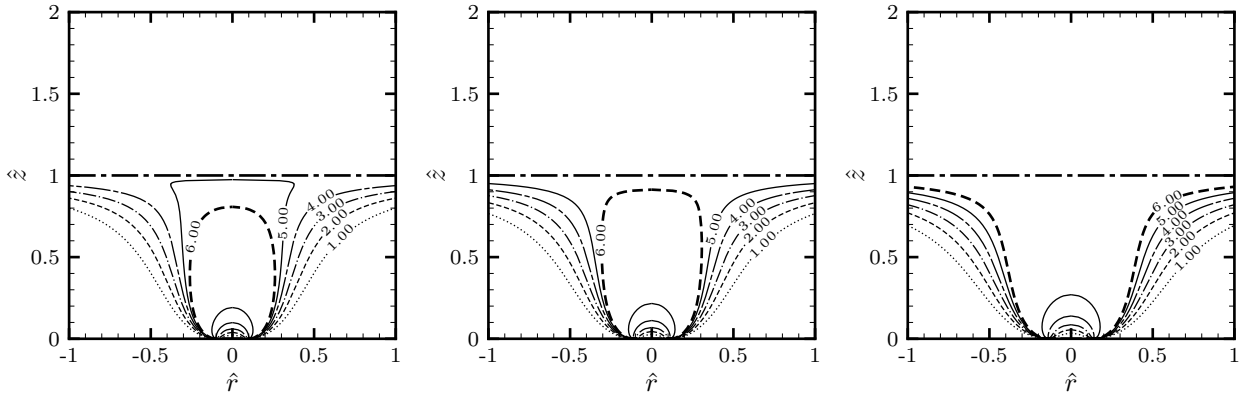

Figure 3.8: Contours of dimensionless temperature fields. The dashed line represents the flame sheet. a) $H_0/D_f = 5.3$ ($H_0 = 10.6\,\text{mm}$); (b) $H_0/D_f = 4.7$ ($H_0 = 9.4\,\text{mm}$); (c) $H_0/D_f = 3.75$ ($H_0 = 7.5\,\text{mm}$). The long-dash-dot line at $\hat{z} = 1$ represents the stagnation plane.

3.3 Water-Laden Counterflow Flames

The addition of water to combustible systems and the interaction between water and the flame has attracted the interest of researchers in past years [143–146]. Water is considered as a nontoxic, noncorrosive suppressant with zero ozone depletion and negligible global warming risks. Previous studies have focused mainly on fire suppression applications since water mists possess significant cooling capacity and diluting effects of reactants in both liquid and vapor phases, reducing the adiabatic flame temperature [143–147]. In addition, studies that have focused in understanding the combustion of water/fuel emulsions have incorporated high amounts of water addition to liquid spray fuels in order to mitigate the production of nitrogen oxides (NOx) in internal combustion engines [148]. Another example of a water laden nonpremixed flame is the methane hydrate flame since large amounts of water are

naturally incorporated into the fuel stream. Molar composition in hydrate fuels is, in general, 86 % water and 14 % methane [149].

In the case of laminar nonpremixed flames, the counterflow burner, due to its practical assembling and modeling, is a configuration that has been broadly used to compare experimental data and the solution of the conservation equations that govern the system. The effect of water addition on nonpremixed counterflow flames has been analyzed in a number of studies, most of them focusing on chemical kinetics effects when water is added to the air side of the burner. The addition of water has also shown effects on three-body recombination and water-gas shift reactions [150–152]. Numerical analysis of similar systems concluded that the concentration of OH radical is increased if water is added to the system, but that this effect is reduced with increasing water addition [153, 154]. The augmented production of OH radical is commonly justified by increased water dissociation. More recently, the effect of water addition to the fuel side of a nonpremixed counterflow burner has been examined numerically and experimentally [155–157]. The effect of water addition on a a similar configuration is performed in this dissertation study to analyze the effect of water addition on the physics of the system by assuming infinite Damkõhler number.

In order to account for the combustion process the infinitely fast chemistry from Reac. (I) is used, reducing the flame to an interface that separates the rich and lean sides. In spite of its simplicity, many important dynamic aspects of the combustion process can be understood by assuming that the chemical reaction between fuel and oxidizer takes place in a single overall step [158]. The conservation equations for axial stagnation flows Section 2.3.1 are simplified by considering Schvab-Zel'dovich variables from Section 2.3.5 for flows with non-unity Lewis numbers and the equations are utilized to determine the steady-state structure of the water-laden counterflow flame system. The gas composition is assumed uniform throughout the domain. The temperature dependence of

thermodynamic and transport properties is obtained, respectively, by the ideal gas law Eq. (2.5) and the power law expression from Eq. (2.36). Buoyancy effects are neglected, and the Prandtl number, defined as $Pr \equiv \nu/\alpha$ is assumed constant, as discussed in Section 2.3.4. The conservation equations, Eqs. (2.16), (2.18), (2.43) and (2.44), can be nondimensionalized as,

$$\frac{d}{d\hat{z}}(\hat{\rho}\hat{u}) + 2\hat{\rho}\hat{V}_z = 0 \tag{3.24}$$

$$\hat{\rho}\hat{u}\frac{d\hat{V}_z}{d\hat{z}} + \hat{\rho}\hat{V}_z^2 - \frac{1}{Re}\frac{d}{d\hat{z}}\left(\hat{\mu}\frac{d\hat{V}_z}{d\hat{z}}\right) = -\hat{\Lambda}_r \tag{3.25}$$

$$\hat{\rho}\hat{u}\frac{dZ}{d\hat{z}} = \frac{1}{LePe}\frac{d}{d\hat{z}}\left(\hat{\rho}\hat{\alpha}\frac{dZ}{d\hat{z}}\right) \tag{3.26}$$

$$\rho\hat{u}\frac{dH}{d\hat{z}} = \frac{1}{Pe}\frac{d}{d\hat{z}}\left(\hat{\rho}\hat{\alpha}\frac{dH}{d\hat{z}}\right) + \frac{K}{Pe}\frac{d}{d\hat{z}}\left(\hat{\rho}\hat{\alpha}\frac{dZ}{d\hat{z}}\right) \tag{3.27}$$

where $\hat{z} \equiv z/L_0$ is the independent variable scaled by the distance between the burner ports L_0. The term $\hat{u} \equiv u/u_0$ is the velocity component in the axial direction scaled by the uniform value at the oxidizer inlet u_0, and $\hat{V}_z \equiv L_0 V_z/u_0$ is the nondimensional scaled velocity in the radial direction. The Reynolds number and the dimensionless eigenvalue are given, respectively, as $Re \equiv L_0 u_0/\nu_0$ and $\hat{\Lambda}_r \equiv \Lambda_r L_0^2/\rho_0 u_0^2$, where ρ_0 and ν_0 are the density and kinematic viscosity at the oxidizer inlet, respectively. The Péclet number is defined as $Pe \equiv RePr$. The boundary conditions required to solve the system of equations are,

$$\hat{u} - \hat{u}_f = \hat{V}_z = Z - 1 = H = 0, \quad \hat{z} = 0 \tag{3.28a}$$

$$\hat{u} + 1 = \hat{V}_z = Z = H = 0, \quad \hat{z} = 1 \tag{3.28b}$$

where $\hat{u}_f \equiv u_f/u_0$ is the nondimensional axial velocity at the fuel inlet.

3.3.1 Model Validation

The counterflow nonpremixed flame configuration represents a strained, laminar, one-dimensional flamelet, with well characterized dynamics. A schematic of the system is shown in Fig. 3.9. The experimental apparatus, described in [155], consists of a pair of steel tubes (nozzles) separated by a finite distance, each surrounded with a concentric coflow of nitrogen (N_2) which prevents burning of fuel with the ambient air. Methane (CH_4), air and nitrogen are supplied by gas cylinders. Water is vaporized in an electric furnace and mixed with methane. Thermocouples are used to measure the temperature distribution in the flame as well as the state of the gas mixtures at the inlets.

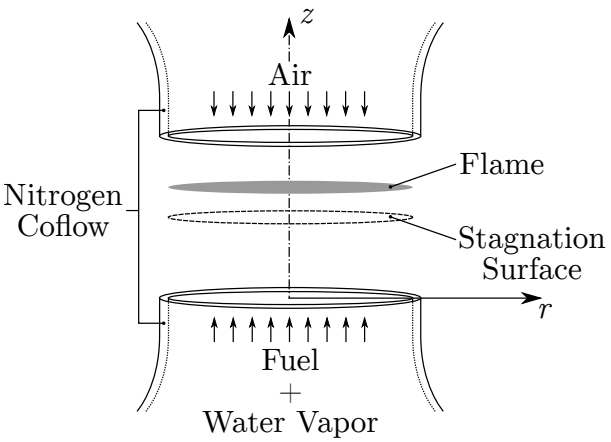

Figure 3.9: Schematic of counterflow nonpremixed flame.

The mixture of fuel and water vapor is issued from the bottom nozzle and air, from the one at the top. The inner diameter of both nozzles is $D_0 = 19\,\text{mm}$ and the separation distance between them is $L_0 = 12.7\,\text{mm}$. For obtaining stabilized, uniform flow at the nozzle exits, the flows are forced through stainless steel beads with an average particle diameter of 2.61 mm and three layers of stainless steel honeycombs. A stainless steel screen covers each nozzle exit. The upper and lower inner tubes are aligned so that their centerline is along the same axis. The burner is placed inside a semi-closed, plexiglas chamber to help isolate the flame from external contamination. The mixture of fuel and water vapor reacts with air near a stagnation plane between the nozzles. A spark-igniter initiates the laminar, flat nonpremixed

flame. To prevent burning of fuel with the ambient air, a N_2 coflow dilutes the products and prevents heating the upper nozzle. The coflow injection velocity is adjusted to be the same as the respective fuel and air injection velocities $u_{F,f}$ and $u_{O,0}$. However, the nominal fuel-side coflow velocity does not include the additional momentum produced when water vapor is added. Commercial mass flow controllers are used to deliver CH_4, air (21 % O_2 and 79 % N_2 in volume) and nitrogen coflow. Deionized liquid water is supplied into the fuel stream using a syringe pump. Water and fuel mixtures run through an electric furnace (maximum heating temperature of (1373 K). The lower nozzle is electrically heated using a heating band and is thermally insulated. Automated stage-mounted B-type thermocouples are used to take temperature profiles of the flame with position. To confirm that water is prevaporized prior to injection at the fuel nozzle exit, temperatures at the electric furnace entrance and exit, and at the fuel nozzle exit are monitored using K-type thermocouples.

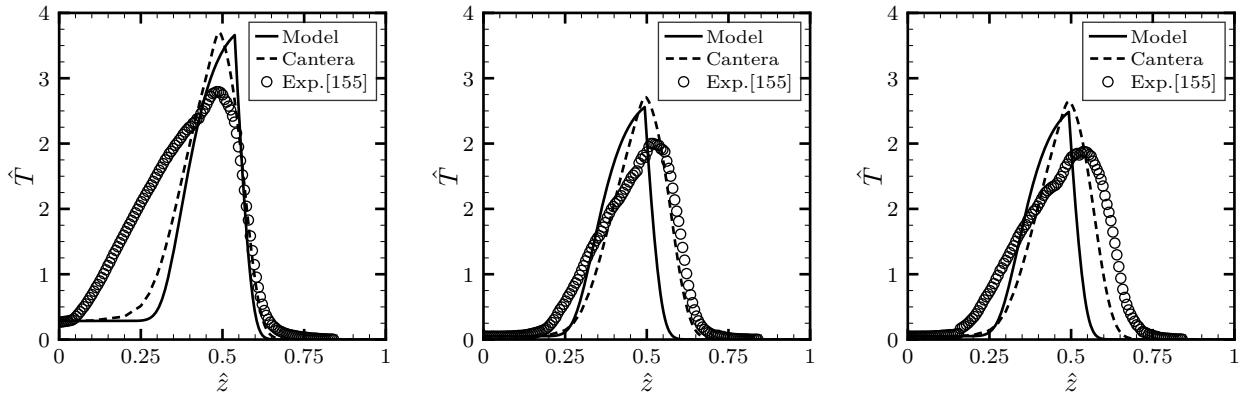

Figure 3.10: Nondimensional temperature profiles for different water to methane molar ratios at the fuel inlet. Solid line: Theoretical model. Symbols: Experimental data from [155]. Water-to-fuel mole fraction (a) 0.00 (b) 1.00 (c) 1.20.

A computational code in Python 2.7 and the FORTRAN BVP_SOLVER [140] subroutine are used to solve the system of ordinary differential equations, Eqs. (3.24) to (3.27). The code can be used to obtain the solution to nonrotating stagnation flows in both axial and radial directions since the general conservation equations from Section 2.3.3 are implemented. The adiabatic flame temperature T_S is modified proportionally to the addition of H_2O molecules

following the volume fractions considered in the experiments. Different values are assumed for the Lewis numbers one the fuel and oxidizer sides, namely, $Le_F = 0.90$ and $Le_O = 0.98$. Dimensionless temperature profiles, obtained using the physical properties of air for the gas mixture, are presented together with measured data from [155], for water to methane mole ratios of 0.00, 1.00 and 1.20 at the fuel inlet, are shown in Fig. 3.10.

It is observed from Fig. 3.10 that the model correlates qualitatively well with the experiment for all cases. The model is also able to predict the variation of peak temperature, even though the maximum value is estimated from a simple proportionality relationship. Experimental data from [155] for the case of zero water addition does not agree with data from the literature, probably because the temperature profile obtained through thermocouple measurements still needs to be corrected to account for thermal losses. Therefore, the temperature data for water to methane molar ratios greater than one are also not expected to be ideally accurate. This can be confirmed by comparing the temperature profile for a system based on the experiments of Puri et al. [159], which have been used to validate nonpremixed counterflow flame simulations. The theoretical model can indeed predict qualitatively the experimental observations as well as the numerical prediction obtained numerically using Cantera [99], as shown in Fig. 3.11.

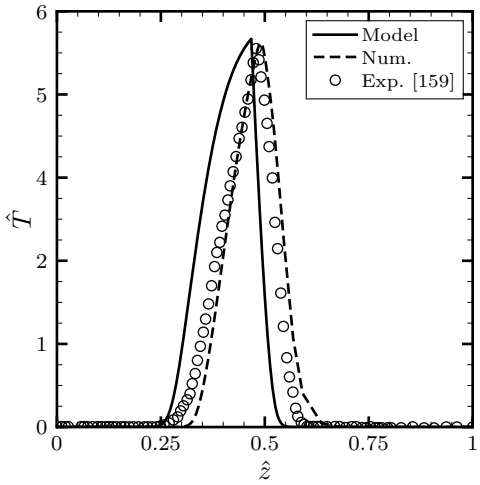

Figure 3.11: Nondimensional temperature profiles. Solid line: Theoretical model. Dashed line: Numerical solution. Symbols: Experimental data from [159].

3.4 Tubular Counterflow Flames Burning Liquid Fuels

The tubular counterflow configuration was proposed by Hu et al. [72], Wang et al. [74] as means to study the effect of curvature on stretched nonpremixed flames. The geometry and stability of the flame produced by the combustor allows the three-dimensional time dependent conservation equations to be described in terms of a system of ordinary differential equations. A schematic of the configuration is shown in Fig. 3.12.

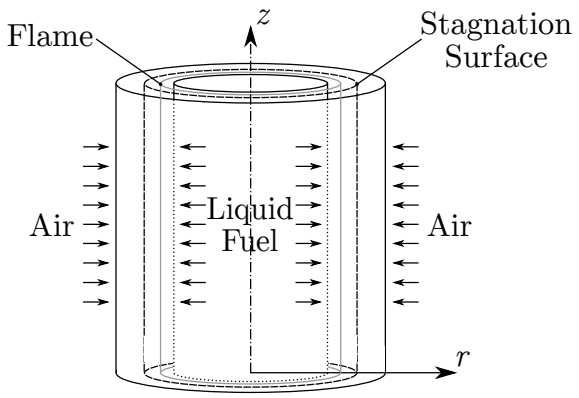

Figure 3.12: Schematic of tubular counterflow nonpremixed flame.

Theoretical analyses of the nonpremixed counterflow tubular flame have been presented in several studies. However, even though hydrogen [72, 74, 80, 81, 160] and gaseous hydrocarbons [72, 74] have been considered, counterflow tubular flames using fuels in condensed phase have not been evaluated by theoretical model or experimentally. In this section, the fundamental modifications to the mathematical model necessary to describe the combustion of a liquid fueled nonpremixed tubular flame are presented.

The mathematical description of the system is based on the same model employed in the evaluation of flames produced by gaseous fuels. The system consists of two long concentric porous tubes through which fuel and oxidizer issue radially as shown in Fig. 3.12. Air is injected inwardly from the outer tube of radius r_0, and liquid fuel evaporates from the inner tube of radius r_f becoming the gaseous fuel source for the combustion reaction. A tubular stagnation surface is created due to the counterbalance of the opposing momentum forces

in the radial direction. The flame is located in the annular space between the concentric porous tubes. The conservation equations, Eqs. (2.25), (2.27), (2.43) and (2.44), can be nondimensionalized as,

$$\frac{d}{d\hat{r}}(\hat{\rho}\hat{r}\hat{v}) + \hat{\rho}\hat{r}\hat{U}_r = 0 \tag{3.29}$$

$$\hat{\rho}\hat{v}\frac{d\hat{U}_r}{d\hat{r}} + \hat{\rho}\hat{U}_r^2 - \frac{1}{Re_0}\frac{1}{\hat{r}}\frac{d}{d\hat{r}}\left(\hat{\mu}\hat{r}\frac{d\hat{U}_r}{d\hat{r}}\right) = -\hat{\Lambda}_z \tag{3.30}$$

$$\hat{\rho}\hat{v}\frac{dZ}{d\hat{r}} = \frac{1}{LePe_0}\frac{1}{\hat{r}}\frac{d}{d\hat{r}}\left(\hat{\rho}\hat{r}\hat{\alpha}\frac{dZ}{d\hat{r}}\right) \tag{3.31}$$

$$\rho\hat{v}\frac{dH}{d\hat{r}} = \frac{1}{Pe_0}\frac{1}{\hat{r}}\frac{d}{d\hat{r}}\left(\hat{\rho}\hat{r}\hat{\alpha}\frac{dH}{d\hat{r}}\right) + \frac{K}{Pe_0}\frac{1}{\hat{r}}\frac{d}{d\hat{r}}\left(\hat{\rho}\hat{r}\hat{\alpha}\frac{dZ}{d\hat{r}}\right) \tag{3.32}$$

where $\hat{r} \equiv r/r_0$ is the independent variable scaled by the radius of the outer tube r_0. The term $\hat{v} \equiv v/v_0$ is the velocity component in the axial direction scaled by the uniform value at the oxidizer inlet v_0, and $\hat{U}_r \equiv r_0 U_r/v_0$ is the nondimensional scaled velocity in the axial direction. The Reynolds number and the dimensionless eigenvalue are given, respectively, as $Re \equiv r_0 v_0/\nu_0$ and $\hat{\Lambda}_z \equiv \Lambda_z r_0^2/\rho_0 v_0^2$, where ρ_0 and ν_0 are the density and kinematic viscosity at the oxidizer inlet, respectively. The Péclet number is defined as $Pe_0 \equiv Re_0 Pr$, where Pr is the Prandtl number.

The main difference between the theoretical description considered herein and the ones in which gaseous fuels issue outwardly through the inner tube is the mathematical description of the boundary conditions on the fuel side. Assuming no penetration of other species at the liquid-vapor interface, Stefan convection and diffusion on the gas side and the convection on the liquid side are related by[†]

$$\hat{v}_{w_+}\hat{Y}_{k,w_+} - \frac{1}{Pe_0}\frac{\partial\hat{Y}_k}{\partial\hat{r}}\bigg|_{\hat{r}_{w_+}} = \hat{v}_{w_+}\hat{Y}_{F,l}\delta_{k,F} \tag{3.33}$$

[†]The derivation is presented for a system in which fuel is injected from the inner wall. However, nonpremixed counterflow-type tubular flames can be established with the fuel inlet at either the inner or the outer tube.

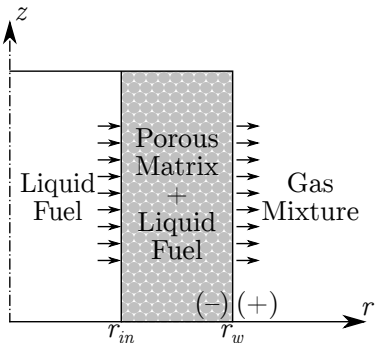

Figure 3.13: Representation of the wall interface.

where δ is the delta function and $\hat{Y}_{F,l}$ is the mass fraction of fuel in the condensed phase. Purely inward radial flow is assumed inside the porous medium, which means that we consider the flow inside the porous matrix not to be affected by the flow in the tube. From mass conservation, the radial velocity $\hat{v}_{w_+}$ at the outer surface of the inner tube is related to the fuel velocity in the condensed phase according to $\hat{v}_{w_+} = \varphi\hat{\rho}_l\hat{v}_{w^-}$, in which $\hat{\rho}_l \equiv \rho_l/\rho$ is the liquid fuel density and φ is the porosity of the permeable tube walls. The subscripts $-$ and $+$ denote the liquid and gas sides at the tube wall, respectively, as shown in Fig. 3.13. From a First Law analysis at the interface, assuming that it is nonreacting,

$$\frac{1}{Pe_0}\left.\frac{\partial\hat{T}}{\partial\hat{r}}\right|_{\hat{r}_{w^+}} = \frac{1}{Pe_m}\left.\frac{\partial\hat{T}}{\partial\hat{r}}\right|_{\hat{r}_{w^-}} + \hat{v}_{w_+}\hat{L} \tag{3.34}$$

where $\hat{L} \equiv L/c_pT_0$, in which L is the latent heat of vaporization and c_p is the specific heat at constant pressure of the gas mixture. The Péclet number on the porous medium side is defined as $Pe_m \equiv r_w v_0/\alpha_m$, where $\alpha_m \equiv \kappa_m/(\rho c)_m$ is the effective thermal diffusivity of the porous medium, in which $\kappa_m \equiv \varphi\kappa_l + (1-\varphi)\kappa_s$, and $(\rho c)_m \equiv \varphi(\rho c)_l + (1-\varphi)(\rho c)_s$ are, respectively, overall thermal conductivity and the overall heat capacity per unit volume. The subscripts l and s denote the liquid and solid phases, respectively.

The radial velocity $\hat{v}_{w_+}$ is related to the outer injection velocity at the liquid-porous matrix interface as $(\hat{r}\hat{v})_{w_+} = \hat{\rho}_l\varphi(\hat{r}\hat{v}_l)_{in}$, in which $\hat{r}_{in}$ and $\hat{v}_{l,in}$ are the radius and velocity of liquid fuel at the inner radius of the tube. The velocity of the liquid fuel at the inner wall $\hat{v}_{w^-}$ can

be written as a function of the injection fuel velocity at the inner surface of the inner porous tube, $(\hat{r}\hat{v})_{w^-} = (\hat{r}\hat{v}_l)_{in}$. The assumption $\hat{r}_{in} \simeq \hat{r}_w$ is imposed.

Fuel is heated from the injection temperature, $\hat{T} = 0$, to a state close to its boiling point $\hat{T} = \hat{T}_b$. The amount of heat necessary for that to happen is supplied by the hot gas in the combustion chamber. Thus, some of the heat generated by the reacting flow is used to vaporize the fuel, and the remainder is conducted into the permeable wall. It is assumed that the porous wall is an isotropic medium where radiative effects, viscous dissipation and work done by pressure changes are negligible, that there is local thermal equilibrium between the solid and fluid phases, and that heat conduction in both phases takes place in parallel such that there is no heat transfer from one phase to the other [161]. Moreover, considering the permeable wall consisting of an interior region at uniform temperature, $\hat{T}_0$, and a thin layer at the wall surface temperature, $\hat{T}_w$, and neglecting the axial components of the fluid flow with respect to the the terms in the radial direction, the heat conducted into the interior of the porous medium is given as,

$$\frac{1}{Pe_m}\left.\frac{\partial \hat{T}}{\partial \hat{r}}\right|_{\hat{r}_{w_-}} = \hat{v}_{w_+}\hat{c}_l\hat{T}_w \tag{3.35}$$

Substituting Eq. (3.35) into Eq. (3.34) and defining an effective latent heat of vaporization as $\hat{L}_{eff} \equiv \hat{c}_l\hat{T}_w + \hat{L}$, where $\hat{c}_l \equiv c_l/c_p$ is the nondimensional specific heat of the liquid phase, we have,

$$\frac{1}{Pe_0}\left.\frac{\partial \hat{T}}{\partial \hat{r}}\right|_{\hat{r}_{w_+}} = \hat{v}_{w_+}\hat{L}_{eff} \tag{3.36}$$

For simplicity (and assuming tacitly that heat conduction is rapid in the porous matrix) the wall surface temperature is assumed to be equal to the boiling point of the fuel, i.e., $\hat{T}_w = \hat{T}_b$. This condition prescribes both the temperature and the mass fraction at the walls. The term $\hat{v}_{w_+}$ becomes an eigenvalue of the problem, specified through the imposition of the

boundary conditions. Its value is determined by considering an estimated value, which is corrected until it equals the real value of $\hat{v}_{w_+}$, obtained by substituting the solution for $\hat{T}$ into Eq. (3.36). The same relationships are found for the case of liquid fuel issuing outwardly, as depicted in Fig. 3.12. The boundary conditions required to solve the system of equations are,

$$\hat{U}_r = \hat{v} - \hat{v}_{w_+} = Z - Z_w = H - H_w, \quad \hat{r} = \hat{r}_w \tag{3.37a}$$

$$\hat{U}_r = \hat{v} + 1 = Z = H = 0, \quad \hat{r} = 1 \tag{3.37b}$$

At the same time, the fluxes of both conserved scalars at the inner wall are obtained by substituting Eqs. (2.45a) and (2.45b) into Eqs. (3.33) and (3.36) as,

$$\frac{1}{Pe_0}\frac{\partial Z}{\partial \hat{r}}\bigg|_{\hat{r}_{w_+}} = \hat{v}_{w_+}\frac{S(1-\hat{Y}_{F,w})}{(S+1)} \tag{3.38a}$$

$$\frac{1}{Pe_0}\frac{\partial H}{\partial \hat{r}}\bigg|_{\hat{r}_{w_+}} = \hat{v}_{w_+}\hat{L}_{eff} \tag{3.38b}$$

The solution for the system of equations is found by assuming heptane as the fuel. The experimental peak flame temperature used as reference corresponds to $\gamma \simeq 4.5$. Experimental measurements are not available for the case of liquid fuels, and, for that reason, conditions equivalent to the ones for gaseous fuels [75] are assumed. The same computational code from Section 3.3 is used to solve the system of ordinary differential equations given in Eqs. (3.29) to (3.32).

Before proceeding with the solution for condensed fuels, the computational code is validated comparing its solution with the experimental temperature profile for a stretched nonpremixed diluted methane-air flame (30 % CH_4/N_2) with stretch rate $k = 122\,s^{-1}$ obtained using Raman spectroscopy [75]. The dimensionless temperature profile is shown in Fig. 3.14. A jump in the experimental data the region near the flame is observed in Fig. 3.14, which is due

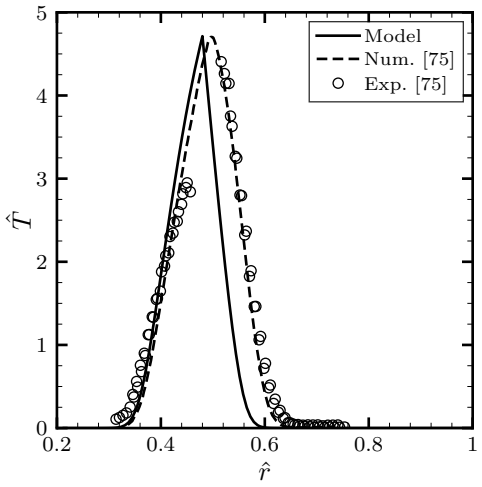

Figure 3.14: Nondimensional temperature profiles for 30 % CH_4/N_2-air flames with stretch rate $k = 122\,\mathrm{s}^{-1}$. Solid line: Theoretical model. Dashed line: Numerical solution from [75]. Symbols: Experimental data from [75].

to the existence of regions where severe interference between C_2 Laser Induced Fluorescence and the Raman signal occur [75]. The data at that region is discarded as a consequence of the great uncertainty produced by this effect. The model predicts qualitatively the temperature profile as well as the location of the reaction zone.

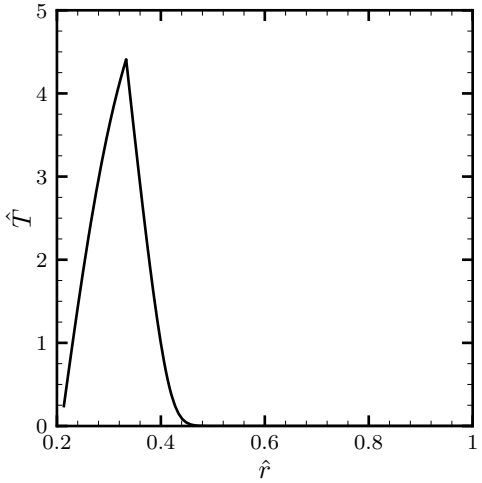

Figure 3.15: Theoretical prediction of nondimensional temperature for liquid fuel-air flames.

The theoretical solution for the case of condensed fuels cannot be validated, because experiments in which that type of fuel is employed are not available in the literature. The theoretical prediction obtained through the solution of the conservation

equations Eqs. (3.29) to (3.32) with boundary conditions Eq. (3.37) is shown in Fig. 3.15. The temperature profile shows the same qualitative structure as the one from gaseous fuels flames (Fig. 3.14). The main difference resides in the fuel injection rate, which in the case of liquid fuels, needs to be of the same order as the vaporization rate to prevent instabilities or extinction, whereas in the case of fuels in gas phase, a wide range of injection velocity are possible. The position of the reaction also agrees qualitatively with the experimental temperature profiles obtained for liquid-pool counterflow flames [45].

Disclosure statement

This chapter, in part, has been published in V. M. Sauer, R. E. Padilla, D. Dunn-Rankin, Analyzing Water-Laden Non-Premixed Counterflow Flames Using the Mixture Fraction/ Excess-Enthalpy Approach, Fort Collins, CO, 1–8, 2013, V. M. Sauer, D. Dunn-Rankin, Impinging Coflow Nonpremixed Methane-Air Flames with Unity Lewis Number, in: 9th US National Combustion Meeting, Cincinnati, OH, 1–10, 2015 and V. M. Sauer, D. Dunn-Rankin, Impinging Nonpremixed Coflow Methane–air Flames with Unity Lewis Number, Proc. Combust. Inst. 36 (1) (2017) 1411–1419 and presented at Analyzing Water-Laden Non-Premixed Counterflow Flames Using Generalized Shvab-Zel'dovich Variables," Work-in-Progress Poster, 35th International Symposium on Combustion, San Francisco, CA. The thesis author is the primary investigator in these publications.

Chapter 4

Swirl-Type Tubular Flames

4.1 Introduction

The axisymmetric tubular flame analysis for liquid fuels is hampered by a lack of experimental data for such systems. The following chapter introduces an experimental system that may be suitable for providing some insights into the effectiveness of the model. Chapter 5 then introduces an analysis motivated by the experiment.

A tubular flame is a classical configuration used in fundamental studies in combustion science. Their characteristic shape, first observed by Ishizuka [65] as circular in cross section and long in the perpendicular direction, distinguishes them from other elementary combustion systems, such as the counterflow, coflow, etc. The most common tubular flame configurations — the swirl type and the counterflow type — have been applied primarily in the analysis of premixed systems. However, after the introduction of nonpremixed counterflow tubular systems [72, 74] interest in tubular combustion configurations has increased due to their cylindrical nature, which allows the study of the effects of flame curvature and, consequently,

they are suitable in turbulent combustion modeling for the description of curved flamelets [70, 163].

The nonpremixed counterflow tubular flame is obtained experimentally by using a modified premixed counterflow tubular burner [67]. One of the reactants is injected outwardly in the radial direction through a porous cylinder along the center axis [72]. An outer contoured nozzle issues inwardly the other reactant. As a consequence, the mathematical model of nonpremixed tubular systems consists of the same conservation equations used to describe premixed tubular flames [97, 164], but with modified boundary conditions to account for the injection of reactants into the chamber from the inner porous cylinder [74, 165]. Another tubular flame configuration in which the reactants are injected separately, the rapidly mixed burner, has been developed recently [166]. This configuration consists of an injection system in which reactants are injected tangentially in a tube through four slits located at its closed end, and a downstream transparent tube allows flame visualization. A Damköhler number analysis suggests that this type of flame can only be established for mixing times shorter than the reaction time, i.e., when the system is actually premixed [167].

The majority of the studies on tubular flames are limited to the analysis of systems with fuel in the gas phase. One of the few exceptions is the liquid film combustor [69]. The liquid film combustor takes advantage of the fact that for miniature systems a condensed fuel layer can offer a surface area for vaporization as high as in vaporizing sprays [73]. In this configuration liquid fuel is injected tangentially onto a tube wall, creating a thin film on its surface. A swirling air flow is introduced from the closed end of the tube through a swirl generator [83]. The injection of swirling air creates a rotational movement of the flow field which helps to spread the fuel and stabilize the film on the combustor inner surface [82].

The combustion of liquid fuels requires a phase change before mixing, and hence is much more complex when compared to combustion of gaseous fuels. In the combustion of condensed fuels the flame is located in the gas phase, and a portion of the heat generated by the

chemical reaction is conducted towards the liquid phase to provide the latent heat needed to vaporize the fuel [168]. At the same time, the gas phase reaction can be accompanied by a number of complicating parameters such as the pyrolysis of the fuel, formation of condensed products, heterogeneous reactions, phase transitions, etc., which, consequently, creates difficulties in developing theoretical models [169]. As a result, the mechanisms involved in the combustion of liquid and gaseous fuels in a tubular system are very distinct, even though the configurations are similar. However, notwithstanding the complications involved in their analysis, most of the fuels used for propulsion are in the liquid phase, making it necessary to develop tubular flame systems where condensed fuels can be applied.

The nonpremixed swirl-type concept is based on radial injection of fuel, and takes advantage of the advances in liquid fuel film and classical tubular flame burners. The nonpremixed swirl-type concept presented herein is based on injection of fuel through porous walls, and takes advantage of the combined advances in liquid fuel film and classical tubular flame burners. In this new configuration, instead of developing a layer of liquid on the walls, the condensed fuel is injected through the permeable burner walls. The condensed fuel vaporizes and becomes the gaseous fuel source for the chemical reaction with the swirling air coming from the bottom inlet. The flame is located in the combustion chamber between the burner walls and the exhaust gas at the core of the chamber. This new configuration, as well as the liquid film burner, are potential alternatives to the systems that, otherwise, would be limited by the difficulties inherent to the atomization of condensed fuel. At the same time, the condensed fuel can offer protection from heat losses and quenching since the temperature of the walls does not exceed the boiling point of the fuel.

The combustor consists of a system in which a permeable material is used to deliver fuel to the combustion chamber. Porous materials have been employed in reacting system for many years. More specifically, in the case of liquid fuels, porous inert media were used in the development of radiant burners [170], for control of noise and instabilities in a swirl-stabilized

combustor [171], to examine flame spread over fuel-soaked ground [172], among others. One of the drawbacks of analyses involving permeable media in combustion is the fact that the porous matrix prevents optical access to the combustion chamber. Therefore, flame visualization and, consequently, the discussion of flame structure and stabilizations mechanisms is not possible with the combustion diagnostic tools currently available.

4.2 Experimental Setup

The system is composed of two concentric cylindrical tubes and an aluminum base used for alignment and support. The liquid fuel flows into the combustion chamber — the hollow central region of the tube — through the walls of the inner tube, which are permeable. The porosity of the walls allows the surface tension to spread the liquid over its volume. The outer tube is solid, made out of quartz. Air is injected axially from the bottom of the combustion chamber through swirl vanes with 15° swirl angle. A jetted photopolymer rapid prototyping machine is used to produce the swirl generators. The schematic of the burner is presented in Fig. 4.1. The porous tube consists of a grade 20 (20 µm) filter element with internal diameter 12.7 mm. The tube is made out of stainless steel meshes formed into cylinders and sintered together. A photographic image of the porous tube is shown in Fig. 4.2. The length of the combustion chamber is 57.5 mm.

The burner is ignited by allowing both air and fuel to flow from their respective feeding lines into the chamber. A propane torch is used to prevaporize some of the liquid fuel as soon as it reaches the porous medium by heating up the outer combustor walls. The flame is then ignited with the propane torch from the downstream region of the burner, above the "Top Support", shown in Fig. 4.1. Lower air flow rates are used during the ignition process, such that the initial proportion of fuel and air injected into the chamber is fuel-rich. The choice of lower air flow rates is made for two reasons. If the cold flow velocity in the chamber was too

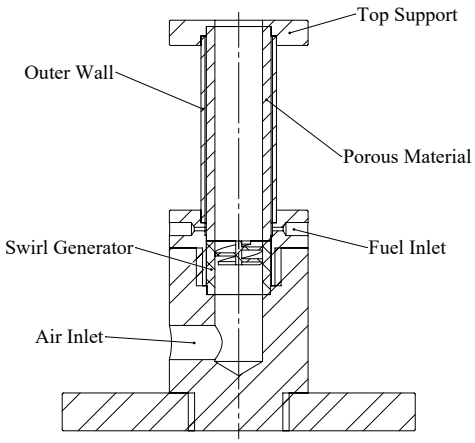

Figure 4.1: Schematic section of the system.

large, it would be difficult for the thermal energy from the propane torch to propagate into the chamber and anchor the flame inside the burner. A premixed flame would be established over the top rim, but it would not sustain itself due to quenching effects induced by the cold flow mixture exiting from the burner. Moreover, if the initial proportion between the flow rates of air and fuel were excessively fuel-lean, the initial mixture could be close to the lower flammability limit, and hence, more difficult to ignite.

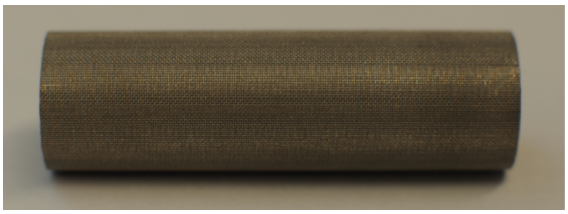

Figure 4.2: Stainless steel filter element.

Two continuous syringe pumps control the injection rate of liquid n-heptane into the burner to allow longer operating times. The condensed fuel leaves the pumps and is mixed into a single line. Before entering the burner, the line is split again. Fuel is delivered to the porous medium through two orifices (indicated in Fig. 4.1 as "Fuel Inlet") that end in a small annular gap between the outer and inner tubes. The liquid fuel is then driven upwards in the small annular space by capillary forces. The volumetric flow rate of fuel is varied from 1 to 2 $\mathrm{mL\,min^{-1}}$. The flow rate of compressed air is controlled by a rotameter calibrated

with a bubble flow meter in the range of 8 to 40 $\mathrm{L\,min^{-1}}$. The volumetric flow rates of air and fuel are varied independently such that several inlet equivalence ratio proportions are considered. Namely, lean, stoichiometric and rich conditions.

Two consumer DSLR cameras with 24.2 MP APS-C CMOS sensors are used to capture photographic images of the overall flame luminosity (mainly due to exited-state CH radicals). The cameras are positioned at different heights, with their optical axis normal to the burner centerline. One camera captures images of the flame formed downstream from the combustion chamber, i.e., the region above the burner rim. The second camera is used to capture images from the top, with its optical axis aligned with the burner axis. A mirror is positioned downstream from the flame at a 45° angle to prevent the camera from direct contact with the hot gases from the downstream region of the flame. The temperature of the outer wall is measured by K-type thermocouples located at the bottom and at the top regions of the quartz tube. The liquid fuel level in the annular region between the porous matrix and the outer tube can be also be quantified, as shown in Fig. 4.3. However, only a qualitative description is considered because the thermocouples need to be taped on the walls, which can alter the heat exchange characteristics between the outer walls and the ambient air. That can potentially modify the liquid level and prevent from an accurate description of the height of liquid-vapor interface at the region close to the tape.

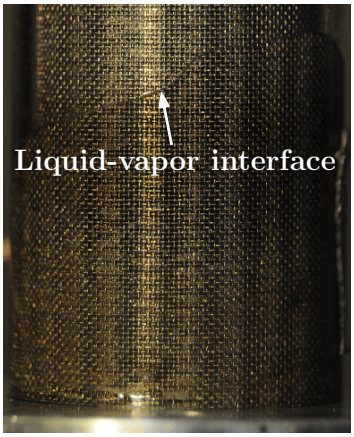

Figure 4.3: Observed fuel liquid-vapor interface.

4.3 Discussion

The porous matrix does not allow the structure of the flame in the combustion chamber to be imaged along the burner axis. Thus, a detailed analysis of the internal flame characteristics such as anchoring mechanisms, measurements of chemical species concentrations and temperature, among others, is not possible. Externally observable characteristics can be used to evaluate qualitatively the system. The shape of the flames observed above the top rim (external to the combustion chamber) depends on the inlet proportions of fuel and air relative to the stoichiometric fuel to air inlet proportions, which is denoted as the inlet equivalence ratio. Depending on the inlet fuel-to-air ratio the flames established inside and outside the combustion chamber can correspond to a single structure with two regions, or to two separate flames.

Measurements of the local outer wall temperature indicate whether the liquid fuel has been completely vaporized in the annular region between the inner and outer tubes. Temperatures higher than the fuel dew point correspond to fuel in the vapor phase flowing into the porous medium. On the other hand, temperature measurements close to the fuel dew point indicate saturated fuel flowing into the porous matrix at that location. The fuel phase can also be monitored throughout the outer quartz tube since it allows visual inspection of the fuel liquid-vapor interface in the annular region. Thermal energy from the downstream zone of the burner is not expected to diffuse downwards in the combustor axial direction very efficiently because the mesh acting as the porous tube is made out of stainless steel, a material with low thermal conductivity. For that reason, large temperature gradients are observed along the outer walls in the longitudinal direction. At heights where the condensed fuel is observed in the annular region, the phase change is expected to occur in the walls of the porous tube. In the zone where condensed phase is not present, fuel vapor is expected to flow from the annular region through the walls of the inner tube.

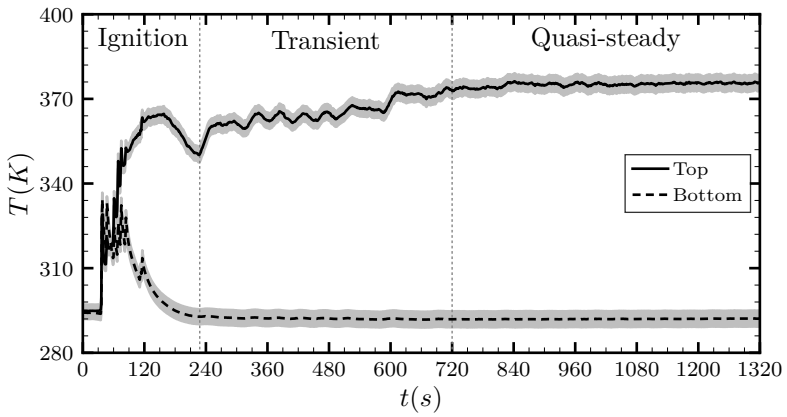

Figure 4.4: Measurement of outer wall temperature variation over time at two selected positions. Volumetric flow rates: $1.4\,\mathrm{mL\,min^{-1}}$ of fuel and $9.6\,\mathrm{L\,min^{-1}}$ of air.

Temperature measurements of the outer wall at two selected heights, one close to the bottom and another next to the top of the burner, help identify whether the inlet equivalence ratio settings produce a stable or an unstable flame. The variation of temperature at those two locations for a stable flame, with flow rates of fuel and air $1.4\,\mathrm{mL\,min^{-1}}$ and $9.6\,\mathrm{L\,min^{-1}}$, respectively, is shown in Fig. 4.4. The temperature measurements, recorded for 22 minutes, show the evolution of local temperature starting from the ignition process. It is observed that after an initial transient period of about eight minutes, the variation in temperature recorded by the thermocouple placed at the top region of the burner is not greater than $\pm 1\,\mathrm{K}$, which is less than the standard uncertainty limits of measurements with K-type thermocouples, represented in the plot as the shaded area surrounding the lines.

4.3.1 Stable Conditions

The stable flame produced in the nonpremixed swirl-type combustor is characterized by time invariant overall structure and burner wall temperatures. Small local oscillations are observed in the flame sitting in the downstream region of the burner. Those local fluctuations are possibly due to nonuniformities in the stainless steel mesh that potentially modify the local heat transfer from the flame, which is converted into latent heat of vaporization for the

liquid fuel, as well as small imperfections in the swirl vanes that produce the rotating flow field of cold air. Further investigation is necessary to accurately describe the nature of those small local instabilities. During stable operating conditions, flickering, extinction or abrupt variations are not observed, neither are steep gradients in the time evolution of the burner wall temperature. Because of the stability of its observed characteristics but persistent small local oscillations, the stable flame is denoted quasi-steady. A flame generated in the nonpremixed swirl burner is assumed to have attained the quasi-steady condition if the burner outer wall temperature and its overall shape, remains stable for a period longer than five minutes. Thus, the system characteristics must be observed for at least a few minutes before any conclusion can be drawn.

The flame shape varies spatially along the burner axis depending on whether the observed region belongs to the luminous core inside or outside the combustion chamber, i.e., bellow or above the "Top Support" shown in Fig. 4.1. For fuel-leaner conditions, in the region above the burner rim, the flame transitions from tubular to inverted conical mainly because of the radial expansion of the tubular structure in the unconfined region above the burner. Some of the combustible mixture continues to burn above the rim and some of it reacts with the outer ambient air, seen as the outer weak zone in Fig. 4.5a, where the tubular flame produced inside the burner is highlighted. Visual inspection shows no discontinuity when the flame transitions from tubular to conical shape, as observed in Fig. 4.6a. If the inlet conditions are fuel-richer, a secondary flame is established above the top rim, which is seen as the outermost intense luminous region at the bottom of Figs. 4.6b and 4.6c. The unburned gas mixture at the burner outlet creates a secondary flame structure that reacts with the ambient air. This secondary reaction zone is indicated in Figs. 4.5b and 4.5c as the outer intense luminous ring.

As observed in the photographic images taken from the top of the burner, the flame possesses a shape that resembles the cylindrical structure observed in the counterflow-type [72] and in

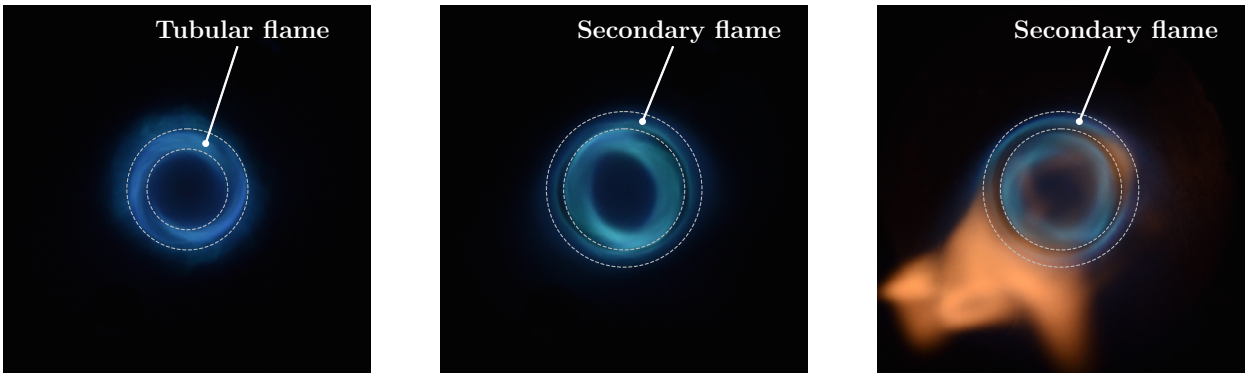

(a) (b) (c)

Figure 4.5: Photographic images (top view) of flames produced by the tubular flame combustor. (a) Single inner flame structure; (b) Dual tubular-secondary flame structure; (c) Sooty flame.

the inner core of the rapidly mixed [173] tubular flame burners. This structure is identified as the more intense inner blue luminous region highlighted in Fig. 4.5a. In all existing tubular flame burners, an intense ring is observed when the tubular flame is imaged from the burner top, i.e., with its axis aligned with the optical axis of the camera. The ring results from the optical effect created by the convolution of the reaction zone, which possesses a tubular shape. However, differently from the conventional tubular flame burners, in which radial or tangential injection of reactants is employed, the present system utilizes swirl vanes to create the rotating flow field. The choice of swirl generators is made for flexibility purposes since it allows the variation of inlet swirl angles. Therefore, instead of a closed luminous ring, in the present configuration the tubular flame is identified as the discontinuous arcs highlighted in Fig. 4.5a.

4.3.2 Transient Conditions

The transient period is defined as the time it takes for the system to transition between a quasi-steady flame and self-adjust to another condition at which the stability is evaluated. Differently from the initial transient observed after ignition (Fig. 4.4), the length of the

(a) (b) (c)

Figure 4.6: Photographic images (side view) of flames produced by the tubular flame combustor. (a) Single inverted conical structure; (b) Dual tubular-secondary flame structure; (c) Sooty flame.

transient period is usually of about three minutes. This is due to the fact that, during the ignition process, foreign heat is dumped into the system by an external heat source (propane torch), which increases the time it takes for the heat transfer processes in the combustor to reach a steady condition. Previous investigations on the liquid film burner do not report clearly the amount of time necessary for the system to reach an equivalent quasi-steady condition. Therefore, the observations in that type of burner might still have influence of the initial heat delivered during ignition by an external heat source. The inlet conditions are set in each run by fixing the flow rate of fuel, while the volumetric flow rate of air is varied. Starting from a previously known stable condition, the flow rate of air is modified to a new selected value, transitioning the system to another condition at which its stability is evaluated. The new settings can produce either a quasi-steady flame, or an unstable flame, that eventually extinguishes. During the transient period the flame structure and the height of the liquid-vapor interface in the annular region between the porous and the quartz tube can demonstrate noticeable variation.

When a quasi-steady flame is established, a meniscus is observed at a height around one quarter of the burner length. For fuel-lean inlet equivalence ratios, the liquid-vapor interface moves downwards until it is not visible through the burner outer walls anymore, corresponding to a complete conversion of condensed fuel into vapor near the inlet. This conversion is confirmed by the temperature recorded by the thermocouple at the bottom of the combustor, which surpasses the boiling point of the fuel. In the fuel lines, however, the fuel remains in condensed phase. The temperature recorded at the top region is increased reaching values as high as 750 K, which is about twice the value recorded during stable operation at the same location. Higher external burner walls temperatures are due the lack of phase change in the annular region. A greater amount of the total heat is transfered from the flame to the fuel as sensible heat, because of the absence of liquid phase in the annular region, increasing the wall temperature. The luminosity of the external flame is reduced and its shape, shorter and narrower than a quasi-steady flame, resembles the premixed low-swirl burner developed at the Lawrence Berkeley National Laboratory [174]. This structure remains visible for not longer than a couple of minutes, after which it finally extinguishes as a completely lifted flame. The process is shown in the photographic images of Fig. 4.7. The flame cannot be sustained by the system because the burning rate at the reaction zone is much greater that the rate at which the fuel is injected into the system. For fuel-rich equivalence ratios the flame structure is longer and sooty (Fig. 4.6c), and the secondary flame formed above the burner rim is clearly observed (Fig. 4.5c). If the equivalence ratios are excessively fuel-rich, the liquid-vapor interface moves upwards in the annular region between the porous and the quartz wall and the flame blows-off. A stable flame cannot be sustained because the heat transfer rate from the reacting zone to the fuel in the porous matrix is smaller than the rate at which the liquid fuel is injected and, therefore, is insufficient to provide the latent heat of vaporization necessary to prevaporize the fuel. As a consequence, the liquid fuel level keeps moving upwards, and the inner flame structure gets quenched.

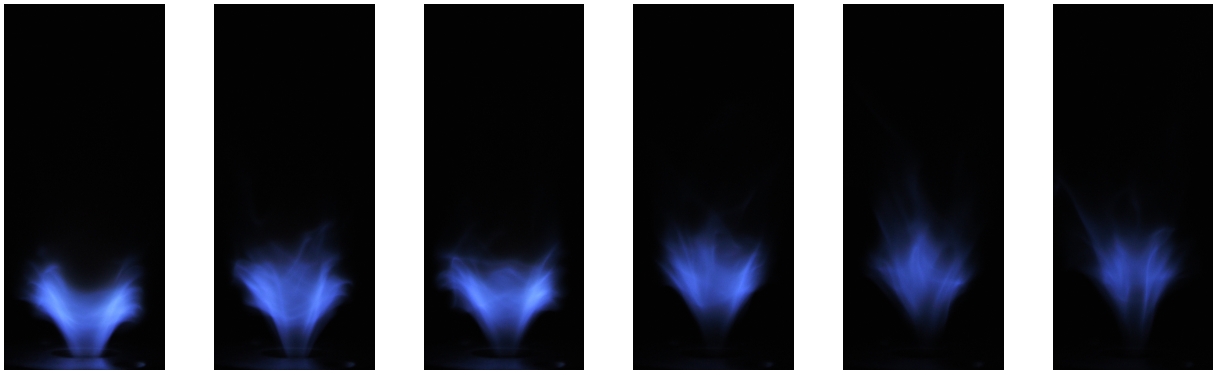

Figure 4.7: Photographic images (side view) of the temporal variation of the system with fuel-lean conditions approaching extinction.

4.3.3 Stability Limits

The system operates in a broad range of inlet equivalence ratios. For quasi-steady conditions, the flame observed above the top rim of the burner can be of two types. The external quasi-steady flame is denoted single if its shape results from the smooth transition of the confined tubular shape into inverted conical in the region above the top support of the burner. A dual flame is produced if unburned gas mixture at the burner outlet creates a secondary flame that reacts with the ambient air. The flame is named dual because two intense luminous reacting zones are observed, as shown Fig. 4.5b. This flame, as well as its structure, is very similar to the one produced by the miniature liquid film burner [82]. For slightly fuel-richer conditions, some regions of the quasi-steady flame emit orange light indicating the presence of soot Fig. 4.6c. Those flame are still stable, although not ideal because of the increased consumption of fuel. Unstable flames are only observed during transient periods since they cannot self-sustain with time. Those flames are either very weak, as the ones shown in Fig. 4.7, or very long and completely orange (resembling the light from a candle), due to the unburned fuel.

In order to identify the operational limits, stability of burning conditions and the observed flame shapes, the working-limit for the burner is presented in Fig. 4.8, where the abscissa represents the inlet liquid fuel flow rate and the ordinate the inlet air flow rate. The

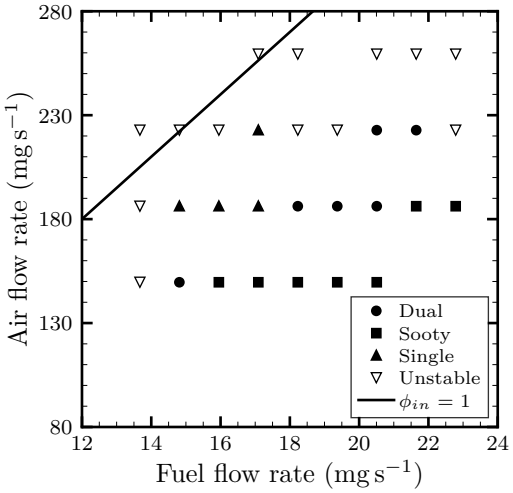

Figure 4.8: Combustor working-limit map.

black line denotes stoichiometric inlet equivalence ratio (ϕ_{in}). The black line separates the map into lean (upper) and rich operation zones (lower). The map shows that all measured points lie in the region of rich conditions. The same operational limitation is observed in the liquid film combustors made out of stainless-steel [84, 87]. Depending on the amount of air introduced into the chamber it is possible to change the flame shape and combustion behavior. Three stable regimes, namely, single (Fig. 4.6a), dual (Fig. 4.6b) and sooty (Fig. 4.6c) are identified by upright triangles, circles and squares, respectively. The unstable weak regime (Fig. 4.7) is represented by hollow inverted triangles. Single flames are observed in fuel-leaner regions of the map. Dual and sooty flames are observed as the proportion of injected fuel is increased. With increasing inlet equivalence ratios, i.e., as the inlet proportions are adjusted to fuel-leaner conditions, the system becomes unstable and only weak flames, which eventually extinguish, are observed. Inlet conditions in the area below those represented in the plot are also unstable, and extinguish by the mechanism described for excess fuel in the system.

The operation envelope can be extended to the fuel-lean region by employing the same strategies considered for the liquid film burner, such as the use of different materials and secondary air injection [84, 87]. These modifications allow the liquid film burner to operate

stably in a wider range of inlet conditions and as well as with fuel lean inlet equivalence ratios. If applied to the nonpremixed swirl-type tubular flame burner it could not only extend the operational conditions of the burner, but also produce a system with potential practical application as personal power systems [86].

Disclosure statement

This chapter, in part, has been published or submitted for publication in V. M. Sauer adn D. Dunn-Rankin, Porous Wall Fed Liquid Fuel Nonpremixed Swirl-Type Tubular Flames, in: 26th ICDERS, Boston, MA, 1-6, 2017. The thesis author is the primary investigator in these publications.

Chapter 5

Swirl-Type Tubular Flames: Theoretical Model

5.1 Introduction

The experimental setup described in Chapter 4 motivates the development of a mathematical model to evaluate and predict theoretically the characteristics of the proposed nonpremixed swirl-type tubular configuration. In this new configuration, illustrated in Fig. 5.1, instead of developing a layer of liquid on the inner surface of the combustion chamber, the condensed fuel is injected through the burner walls, which are permeable. The condensed fuel vaporizes thereby becoming the gaseous fuel source for the chemical reaction with the swirling air that is injected axially. The flame is located in the combustion chamber between the burner walls and the exhaust gas.

The mathematical description of the system is based on the two classical models for pipes flows. The fuel injection is described by the theory of laminar pipe flows with porous walls. The solution of the Navier-Stokes equations for fully developed flows in channels

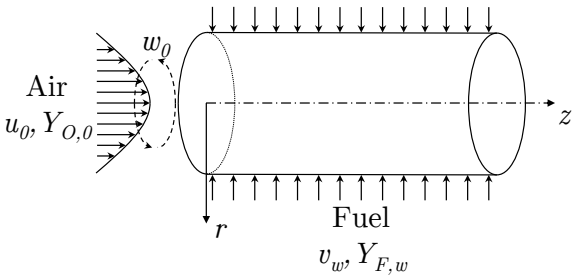

Figure 5.1: Representation of the physical system.

with rectangular permeable walls were first presented by Berman [175]. A constant flow velocity inside the porous wall was assumed, and the conservation equations transformed using a stream function defined in terms of a similarity variable. The analysis was extended to circular pipe flows by Yuan and Finkelstein [176], and was extensively investigated in several studies by a number of groups [177–182]. The study of rotating porous pipes was also considered, but with the assumption that swirl velocity was constant along the pipe [183–186]. Details of the published work on laminar flows in porous ducts has been presented recently in an in-depth review [187]. The theory for laminar pipe flows with porous walls was extended by Yuan and Finkelstein [188] for the investigation of the heat transfer problem for a steady fully developed laminar flow developed by Graetz [189]. The conservation equations for energy and species were modified by the introduction of velocity components from the solution of the momentum equations for laminar pipe flows with porous walls. Their work was followed by a number of investigations that accounted for injection and extraction of mass [190], different boundary conditions [191], mass transfer cooling [192], and internal heat sources [193]. The analysis of the flow field in the system is performed on the basis of the theory developed for swirling laminar flows. Among early relevant analytical descriptions of this type of flow are those of Collatz and Görtler [194] and Talbot [195], who analyzed analytically the decay of swirl in tubes with impermeable walls. Collatz and Görtler [194] presented a solution for the tangential velocity field, but it did not account for concomitant disturbances of the axial and radial velocity fields. On the other hand, Talbot [195] presented a study in which the disturbances of the axial and radial velocities were

considered using a momentum integral equation. Deka [196, 197] and Lavan et al. [198] obtained an equivalent solution to problems in which the downstream section of the tube rotates and the upstream region is stationary by employing integral transforms. Kreith and Sonju [199] extended the analysis to study the swirl decay in turbulent flows, modifying the swirl equations through the introduction of an eddy-diffusivity term. Kinney and Sparrow [200] extended the analytical solution of the swirl decay in tubes by combining it with the theory of laminar pipe flows with porous walls to account for tubes with surface mass transfer. The assumption in their analysis is similar to the ones from Deka [196, 197] and Lavan et al. [198], and consisted of a porous pipe with a downstream rotating porous wall where the swirl is generated and an upstream stationary permeable pipe where mass is injected (or removed) and the swirl decays. Lee et al. [201] used the same framework as Talbot [195] to obtain the velocity field for the growing swirl in a rotating tube. The resultant mixing induced by the fluid flow in the presence of molecular diffusion and chemical reactions was characterized.

The analysis herein combines the effect of swirl decay in tubes with heat and mass transfer in laminar pipe flows with porous walls. Although considered separately in the prior work cited above, these effects have not before been combined in the analysis of reacting nor nonreacting flows in pipes. The model is used to predict important flame characteristics in a nonpremixed system, in which the oxidizer is introduced through a swirling flow from one end and fuel is supplied from the walls of the burner. The conservation equations for energy and species are transformed using the Shvab-Zel'dovich approach, so that the solution methods used in the study of convective heat and mass transfer in confined flows can also be applied. The model can provide theoretical support and general design guidelines to the development of nonpremixed swirl-type tubular systems such as those shown experimentally in Chapter 4.

5.2 Theoretical Model

The conservation equations Eqs. (2.6) to (2.11) are nondimensionalized in order to simplify the evaluation of the terms. The dimensionless axisymmetric steady state conservation equations of mass, momentum in the axial, radial and tangential directions, energy and species for the gas phase, considering it an incompressible flow with constant physical properties throughout the whole domain, are given by,

$$\frac{1}{Re_0}\frac{\partial \hat{u}}{\partial \hat{z}} + \frac{1}{\hat{r}}\frac{\partial}{\partial \hat{r}}(\hat{r}\hat{v}) = 0 \tag{5.1}$$

$$\frac{\hat{u}}{Re_0}\frac{\partial \hat{u}}{\partial \hat{z}} + \hat{v}\frac{\partial \hat{u}}{\partial \hat{r}} = -\frac{1}{Re_0}\frac{\partial \hat{p}}{\partial \hat{z}} + \frac{2}{Re_0}\left[\frac{1}{\hat{r}}\frac{\partial}{\partial \hat{r}}\left(\hat{r}\frac{\partial \hat{u}}{\partial \hat{r}}\right) + \frac{1}{Re_0^2}\frac{\partial^2 \hat{u}}{\partial \hat{z}^2}\right] \tag{5.2}$$

$$\frac{\hat{u}}{Re_0}\frac{\partial \hat{v}}{\partial \hat{z}} + \hat{v}\frac{\partial \hat{v}}{\partial \hat{r}} - \frac{\hat{w}^2}{\hat{r}} = -\frac{\partial \hat{p}}{\partial \hat{r}} + \frac{2}{Re_0}\left[\frac{1}{\hat{r}}\frac{\partial}{\partial \hat{r}}\left(\hat{r}\frac{\partial \hat{v}}{\partial \hat{r}}\right) - \frac{\hat{v}}{\hat{r}^2} + \frac{1}{Re_0^2}\frac{\partial^2 \hat{v}}{\partial \hat{z}^2}\right] \tag{5.3}$$

$$\frac{\hat{u}}{Re_0}\frac{\partial \hat{w}}{\partial \hat{z}} + \hat{v}\frac{\partial \hat{w}}{\partial \hat{r}} + \frac{\hat{v}\hat{w}}{\hat{r}} = \frac{2}{Re_0}\left[\frac{1}{\hat{r}}\frac{\partial}{\partial \hat{r}}\left(\hat{r}\frac{\partial \hat{w}}{\partial \hat{r}}\right) - \frac{\hat{w}}{\hat{r}^2} + \frac{1}{Re_0^2}\frac{\partial^2 \hat{w}}{\partial \hat{z}^2}\right] \tag{5.4}$$

$$\frac{\hat{u}}{Re_0}\frac{\partial \hat{Y}_k}{\partial \hat{z}} + \hat{v}\frac{\partial Y_k}{\partial \hat{r}} = \frac{2}{Pe_0}\left[\frac{1}{\hat{r}}\frac{\partial}{\partial \hat{r}}\left(\hat{r}\frac{\partial \hat{Y}_k}{\partial \hat{r}}\right) + \frac{1}{Re_0^2}\frac{\partial^2 \hat{Y}_k}{\partial \hat{z}^2}\right] - S_k\hat{\dot{m}}_F \tag{5.5}$$

$$\frac{\hat{u}}{Re_0}\frac{\partial \hat{T}}{\partial \hat{z}} + \hat{v}\frac{\partial \hat{T}}{\partial \hat{r}} = \frac{2}{Pe_0}\left[\frac{1}{\hat{r}}\frac{\partial}{\partial \hat{r}}\left(\hat{r}\frac{\partial \hat{T}}{\partial \hat{r}}\right) + \frac{1}{Re_0^2}\frac{\partial^2 \hat{T}}{\partial \hat{z}^2}\right] + \gamma(1+S)\hat{\dot{m}}_F \tag{5.6}$$

where $\hat{u} \equiv u/U_0$, $\hat{v} \equiv v/U_0$ and $\hat{w} \equiv w/U_0$ are the velocity components in the axial, radial and circumferential directions scaled by the average velocity at the inlet U_0. The other dependent variables, $\hat{p} \equiv p/\rho U_0^2$ and $\hat{Y}_k \equiv \hat{Y}_k/\hat{Y}_{k,\mathrm{ref}}$ are pressure and mass fractions of species k, respectively, for k = F, O, CO_2 or H_2O, scaled by their respective reference values, with ρ representing the gas density. The temperature $\hat{T}$ is defined as in Section 2.3.5. The independent variables $\hat{r} \equiv r/r_w$ and $\hat{z} \equiv z/r_w Re_0$ are scaled by the internal radius of the tube, r_w, and the Reynolds number, $Re_0 \equiv 2r_w U_0/\nu$, where ν is the gas kinematic viscosity. The term $\hat{\dot{m}}_F \equiv r_w \dot{m}_F/\rho U_0$ represents nondimensional the rate of consumption of fuel mass. The flows considered are laminar with large axial Reynolds numbers Re_0, therefore, diffusion in the streamwise direction is negligible since it scales with $1/Re_0^2$. Besides

the condition of equal diffusion speed between all species, unity Lewis numbers are assumed, i.e., equal mass and heat diffusion, denoted by $\mathcal{D}$ and α, respectively. Péclet number is defined $Pe_0 \equiv 2r_w U_0/\alpha$. The stoichiometric mass ratios are defined as $S \equiv sY_{F,w}/Y_{O,0}$, $S_{H_2O} \equiv s_{H_2O}Y_{F,w}$ and $\mathrm{S}_{CO_2} \equiv s_{CO_2}Y_{F,w}$ and the heat release $\gamma \equiv q_c Y_{F,w}/c_p T_0(S+1)$, where q_c is the amount of heat released per unit mass of fuel burnt and c_p is the specific heat at constant pressure of the gas phase. Buoyancy, heat transport by radiation, and Soret and Dufour effects are neglected in the analysis. Fick's law is used to describe diffusion velocities of the species.

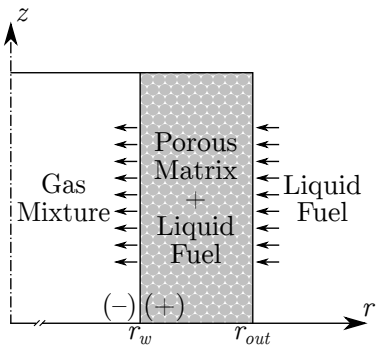

Figure 5.2: Representation of the wall interface.

The mathematical formulation for porous boundary conditions discussed in Section 3.4 is considered to describe the permeable tube walls. However, following the notation from the wall interface represented in Fig. 5.2. As a consequence of the prescribed boiling temperature boundary condition, the mass and energy fluxes at the walls are allowed to vary in the axial direction. In order to further simplify the model, an average value $\hat{V}_w$ is used in the conservation equations as an approximation to the absolute value $|\hat{v}_{w_-}|$ of the velocity at the wall. The term $\hat{V}_w$ becomes an eigenvalue of the problem, specified through the imposition of the boundary conditions. Its value is determined by considering an estimate value $\hat{V}_w$, which is corrected until it equals the average of $|\hat{v}_{w_-}|$, obtained by substituting the solution for $\hat{T}$ into Eq. (3.36). The boundary conditions at the internal surface of the tube are given

as,

$$\frac{\partial \hat{u}}{\partial \hat{r}} = \hat{v} = \hat{w} = \frac{\partial \hat{Y}_k}{\partial \hat{r}} = \frac{\partial \hat{T}}{\partial \hat{r}} = 0, \quad \hat{r} = 0 \tag{5.7a}$$

$$\hat{u} = \hat{v} + \hat{V}_w = \hat{w} = \hat{T} - \hat{T}_b = \hat{Y}_F - \hat{Y}_{F,w} = \hat{Y}_O = 0, \quad \hat{r} = 1 \tag{5.7b}$$

$$\hat{u} - \hat{u}_0 = \hat{v} = \hat{w} - \hat{w}_0 = \hat{T} = \hat{Y}_F = \hat{Y}_O - 1 = 0, \quad \hat{z} = 0 \tag{5.7c}$$

In this analysis, a swirl velocity $\hat{w}_0$, with a maximum intensity $\hat{W}_0 \equiv W_0/U_0$, is imposed at the flow inlet satisfying the condition $\hat{W}_0 \ll 1$. Therefore, the swirl component in the flow field can be considered as a perturbation, which permits the use of series expansion to solve the problem. The condition of a long tube with a very small ratio of radius to length is considered. The oxidant injected through one of the tube ends is limited by the conditions of a laminar Reynolds number Re_0. However, the amount of injected fuel can be as large as the tube length permits, which, at some position along the tube, can create excessively rich regions that result in local flame extinction. Under some conditions, the flame can reignite and maintain itself for a certain length, establishing "flame-streets" as defined by Mohan and Matalon [202]. This combustion regime will not be included in the analysis.

The linear combination of energy and mass fraction conservation equations eliminates the reaction terms through the introduction of two conserved scalars, namely, the mixture fraction Z, and the excess-enthalpy H, as proposed by Liñán et al. [4], as defined in, Eqs. (2.45a) and (2.45b), respectively. The conservation equations for the conserved scalars are given by,

$$\frac{\hat{u}}{Re_0}\frac{\partial Z}{\partial \hat{z}} + \hat{v}\frac{\partial Z}{\partial \hat{r}} - \frac{2}{Pe_0}\left[\frac{1}{\hat{r}}\frac{\partial}{\partial \hat{r}}\left(\hat{r}\frac{\partial Z}{\partial \hat{r}}\right)\right] = 0 \tag{5.8}$$

$$\frac{\hat{u}}{Re_0}\frac{\partial H}{\partial \hat{z}} + \hat{v}\frac{\partial H}{\partial \hat{r}} - \frac{2}{Pe_0}\left[\frac{1}{\hat{r}}\frac{\partial}{\partial \hat{r}}\left(\hat{r}\frac{\partial H}{\partial \hat{r}}\right)\right] = 0 \tag{5.9}$$

The boundary conditions for Eqs. (5.8) and (5.9) are obtained by combining Eqs. (2.45a), (2.45b) and (5.7),

$$\frac{\partial Z}{\partial \hat{r}} = \frac{\partial H}{\partial \hat{r}} = 0, \quad \hat{r} = 0 \tag{5.10a}$$

$$H - H_w = Z - Z_w = 0, \quad \hat{r} = 1 \tag{5.10b}$$

$$H = Z = 0, \quad \hat{z} = 0 \tag{5.10c}$$

At the same time, the fluxes of both conserved scalars at the walls are obtained by substituting Eqs. (2.45a) and (2.45b) into Eqs. (3.33) and (3.36) as,

$$\frac{2}{Pe_0}\frac{\partial Z}{\partial \hat{r}}\bigg|_{\hat{r}=1} = \hat{v}_{w-}\frac{S(1-\hat{Y}_{F,w})}{(S+1)} \tag{5.11a}$$

$$\frac{2}{Pe_0}\frac{\partial H}{\partial \hat{r}}\bigg|_{\hat{r}=1} = \hat{v}_{w-}\hat{L}_{eff} \tag{5.11b}$$

5.2.1 Flow Field

The model is based on the theory of internal laminar swirling flows with surface mass and heat transfer. Due to the swirling nature of the gas flow, the equations of motion are represented in a form that allows the rotating field to be taken into account by superimposing a laminar swirl flow on a Poiseuille flow in a straight pipe. The flow through the tube is two-dimensional, axisymmetric, laminar and the physical properties do not vary with temperature. The velocity components are represented in the form [196],

$$\hat{u} = \hat{u}^o(\hat{z},\hat{r}) + \varepsilon^2\hat{u}^*(\hat{z},\hat{r}) + \mathcal{O}\left(\varepsilon^3\right) \tag{5.12a}$$

$$\hat{v} = \hat{v}^o(\hat{r}) + \varepsilon^2\hat{v}^*(\hat{z},\hat{r}) + \mathcal{O}\left(\varepsilon^3\right) \tag{5.12b}$$

$$\hat{w} = \varepsilon\hat{w}^*(\hat{z},\hat{r}) + \mathcal{O}\left(\varepsilon^2\right) \tag{5.12c}$$

in which the superscript o represents $\mathcal{O}(\varepsilon^0)$ terms, i.e., velocities of undisturbed flow field and the velocity downstream, where perturbations have dissipated and the velocity field has attained a fully developed profile. Since axisymmetric conditions are imposed on the problem, the circumferential velocity perturbation $\hat{w}^*$ has an influence on the species and temperature field through the other velocity components, $\hat{u}$ and $\hat{v}$. By considering $\hat{w}$ as a perturbation of $\mathcal{O}(\varepsilon)$, from Eq. (5.3), it is observed that its effect is to induce a $\mathcal{O}(\varepsilon^2)$ perturbation to the velocity components $\hat{u}$ and $\hat{v}$. The model does not account for perturbations other than the one due to the swirl, therefore $\mathcal{O}(\varepsilon)$ terms are not included in the axial and radial velocities expansions in Eq. (5.12). The term $\hat{W}_0$ is assumed as the magnitude of the swirl perturbation. Consequently, in Eq. (5.12), for $\hat{W}_0 \ll 1$, $\varepsilon = \hat{W}_0$. The swirl angle θ is related to $\hat{W}_0$ by,

$$\hat{W}_0 = \tan\theta \tag{5.13}$$

The procedure employed to obtain the velocity components of the flow field in this section follows closely the derivation presented by Kinney and Sparrow [200].

5.2.1.1 Fully Developed Velocity Profile

With the assumption of steady burning, the mass flow rate of fuel from the porous walls is constant. In the fully developed region of such flows, it has been shown [176] from the overall mass conservation that the flow field can be described in terms of the nondimensional stream function,

$$\hat{\Psi}(\hat{z},\hat{r}) = \frac{1}{2}\hat{r}G(\hat{r})\hat{U}(\hat{z}) \tag{5.14}$$

in which $G(\hat{r})$ is an unspecified function of $\hat{r}$, and the function $\hat{U}(\hat{z}) = (1 + 2Re_w\hat{z})$ is the flow local mean axial velocity [194], where the wall injection Reynolds number is defined as,

$$Re_w \equiv 2r_w V_w/\nu = \hat{V}_w Re_0 \tag{5.15}$$

The velocity components in the axial and radial directions can be written, respectively, as [178],

$$\hat{u}^o(\hat{z},\hat{r}) = U(\hat{z})F(r) \tag{5.16a}$$

$$\hat{v}^o(\hat{r}) = -\hat{V}_w G(\hat{r}) \tag{5.16b}$$

The term $F(\hat{r})$ is a function of $\hat{r}$ yet to be determined. Substituting $\hat{u}^o$ and $\hat{v}^o$ from Eqs. (5.12) and (5.16) into Eqs. (5.1) and (5.2), we obtain a system of differential equations for F and G, namely,

$$2F - G' - \frac{G}{\hat{r}} = 0 \tag{5.17a}$$

$$Re_w\left(2F^2 - GF'\right) - 2\left(F'' + \frac{F'}{\hat{r}}\right) = -\hat{\Lambda} \tag{5.17b}$$

where,

$$\hat{\Lambda} = \frac{1}{\hat{U}}\frac{\partial \hat{p}}{\partial \hat{z}} \tag{5.18}$$

is an eigenvalue of the problem. The prime ($'$) represents differentiation with respect to $\hat{r}$. The boundary conditions, Eq. (5.7), can be modified, namely,

$$F' = G = 0, \quad \hat{r} = 0 \tag{5.19a}$$

$$F = G - 1 = 0, \quad \hat{r} = 1 \tag{5.19b}$$

in order to determine the functions F and G together with the pressure gradient term $\hat{\Lambda}$. For the special case of impermeable walls, in which $Re_w = 0$, the solution of Eq. (5.17) yields the Poiseuille parabolic profile $F = 2(1 - \hat{r}^2)$, with the dimensionless pressure gradient $\hat{\Lambda} = 16$.

5.2.1.2 Axial Decay of Swirl Velocity

Substituting the expressions from Eq. (5.12) into Eq. (5.4), collecting terms of order $\mathcal{O}(\varepsilon)$ and neglecting higher order terms one obtains,

$$\frac{\hat{u}^o}{Re_0}\frac{\partial \hat{w}^*}{\partial \hat{z}} + \hat{v}^o\frac{\partial \hat{w}^*}{\partial \hat{r}} + \frac{\hat{v}^o\hat{w}^*}{\hat{r}} = \frac{2}{Re_0}\left(\frac{\partial^2 \hat{w}^*}{\partial \hat{r}^2} + \frac{1}{\hat{r}}\frac{\partial \hat{w}^*}{\partial \hat{r}} - \frac{\hat{w}^*}{\hat{r}^2}\right) \tag{5.20}$$

Substituting the expressions for $\hat{u}^o$ and $\hat{v}^o$ from Eq. (5.16) into Eq. (5.20), one finds,

$$\frac{2}{F}\left[\frac{\partial^2 \hat{w}^*}{\partial \hat{r}^2} + \left(\frac{Re_w G}{2} + \frac{1}{\hat{r}}\right)\frac{\partial \hat{w}^*}{\partial \hat{r}} + \left(\frac{Re_w G}{2} - \frac{1}{\hat{r}}\right)\frac{\hat{w}^*}{\hat{r}}\right] = \hat{U}\frac{\partial \hat{w}^*}{\partial \hat{z}} \tag{5.21}$$

Both sides of Eq. (5.21) are functions of only one independent variable, thus its solution can be found by a separation of variables in the form,

$$\hat{w}^*(\hat{z}, \hat{r}) = \psi(\hat{z})\phi(\hat{r}) \tag{5.22}$$

which can be substituted into Eq. (5.21), yielding,

$$\frac{2}{F\phi}\left[\frac{d^2\phi}{d\hat{r}^2} + \left(\frac{Re_w G}{2} + \frac{1}{\hat{r}}\right)\frac{d\phi}{d\hat{r}} + \left(\frac{Re_w G}{2} - \frac{1}{\hat{r}}\right)\frac{\phi}{\hat{r}}\right] = \frac{U}{\psi}\frac{d\psi}{d\hat{z}} = -\lambda \tag{5.23}$$

The solution for the axial direction is obtained by integrating the equation for $\psi(\hat{z})$ as,

$$\psi(\hat{z}) = c_1\hat{U}^{-\lambda/(2Re_w)} \tag{5.24}$$

where c_1 is the constant of integration. The equation for $\phi(\hat{r})$ is given by,

$$\frac{d^2\phi}{d\hat{r}^2} + \left(\frac{Re_w G}{2} + \frac{1}{\hat{r}}\right)\frac{d\phi}{d\hat{r}} + \left(\frac{Re_w G}{2} - \frac{1}{\hat{r}}\right)\frac{\phi}{\hat{r}} + \lambda\frac{F}{2}\phi = 0 \tag{5.25}$$

which can be cast into Sturm-Liouville form through the introduction of an integrating factor,

$$q_\phi(\hat{r}) = \exp\left[\int\left(\frac{Re_w G}{2} + \frac{1}{\hat{r}}\right)d\hat{r}\right] \tag{5.26}$$

yielding,

$$\frac{d}{d\hat{r}}\left(q_\phi\frac{d\phi}{d\hat{r}}\right) + \left[\frac{q_\phi}{\hat{r}}\left(\frac{Re_w G}{2} - \frac{1}{\hat{r}}\right)\right]\phi + \lambda\sigma_\phi\phi = 0 \tag{5.27}$$

where the weight function $\sigma_\phi(\hat{r})$ is given by,

$$\sigma_\phi(\hat{r}) = q_\phi F/2 \tag{5.28}$$

The swirl velocity $\hat{w}^*$ must vanish at the tube wall ($\hat{r} = 1$) and at the symmetry axis ($\hat{r} = 0$). These conditions must be satisfied for all $\hat{z}$, such that, $\phi(0) = \phi(1) = 0$. In order to solve Eq. (5.27) numerically a starting estimate and a condition for the eigenvalues λ are necessary. The later is obtained from the orthogonality condition, which requires that, for orthonormal eigenfunctions,

$$\int_0^1 \phi_m(\hat{r})\phi_n(\hat{r})\sigma_\phi(\hat{r})d\hat{r} = \delta_{mn}||\phi_n||^2 \tag{5.29}$$

The solution for the special case $Re_w = 0$ can be used as the starting estimate to the one for any Re_w. Such an educated guess is appropriate because the solution for the problem with surface mass transfer at the walls presents a relatively small deviation from the special case of

impermeable walls. The solution for $Re_w = 0$ can be obtained using the transformation [195],

$$\phi^0(\tau) = \tau^{1/2} \exp(-\tau/2) g(\tau), \quad \text{such that} \quad \tau = \sqrt{\lambda}\, \hat{r}^2 \tag{5.30}$$

which yields,

$$\tau \frac{d^2 g}{d\tau^2} + (2 - \tau) \frac{dg}{d\tau} - \left(1 - \frac{\sqrt{\lambda}}{4}\right) g = 0 \tag{5.31}$$

which is the confluent hypergeometric differential equation [203]. The solution of Eq. (5.31), which is regular at $\tau = 0$, is given by

$$g(\tau) = {}_1F_1(a, b, \tau) = \sum_{k=0}^{\infty} \frac{a^{(k)} \tau^k}{b^{(k)} k!} \tag{5.32}$$

where the superscript (k) represents the rising factorial (Pochhammer symbol). If $\phi_n^0(\hat{r})$ denotes the eigenfunctions $n = 1, 2, 3, ...$ for the special case $Re_w = 0$, the complete solution can be written using

$$\phi_n^0(\hat{r}) = \lambda_n^{1/4} \hat{r} \exp\left(-\frac{\sqrt{\lambda_n}}{2} \hat{r}^2\right) {}_1F_1\left(1 - \frac{\sqrt{\lambda_n}}{4}, 2, \sqrt{\lambda_n} \hat{r}^2\right) \tag{5.33}$$

Using $\phi_n^0(\hat{r})$ as the initial guess to the solution of Eq. (5.27), the swirl velocity $\hat{w}^*(\hat{z}, \hat{r})$ for any Re_w, is obtained by,

$$\hat{w} = \varepsilon \hat{w}^* = \hat{W}_0 \sum_{n=1}^{\infty} c_n \phi_n \hat{U}^{-\lambda_n/(2Re_w)} \tag{5.34}$$

For the special case of tubes with impermeable walls, the swirl velocity is given by,

$$\hat{w} = \hat{W}_0 \sum_{n=1}^{\infty} c_n \phi_n^0 \exp(-\lambda_n \hat{z}) \tag{5.35}$$

The boundary condition at $\hat{r} = 0$ is automatically satisfied, and the remaining boundary condition at $\hat{r} = 1$ is used to determine the eigenvalues λ_n. The constants c_n are determined such that $\hat{w}^*(\hat{z}, \hat{r})$ equals the boundary condition at $\hat{z} = 0$, $\hat{w}_0^*(\hat{r})$. Hence,

$$c_n = \frac{1}{||\phi_n||^2} \int_0^1 \hat{w}_0^*(\hat{r}) \phi_n(\hat{r}) \sigma_\phi(\hat{r}) d\hat{r} \tag{5.36}$$

where the norm $||\phi_n||^2$ is defined in Eq. (5.29). The inlet swirl velocity $\hat{w}_0^*(\hat{r})$ is assumed to behave as a Rankine vortex, i.e.,

$$\hat{w}_0^*(\hat{r}) = \begin{cases} \hat{r}/\hat{r}_0, & \hat{r} \leqslant \hat{r}_0 \\ (\hat{r}_0/\hat{r})(1-\hat{r})/(1-\hat{r}_0), & \hat{r} > \hat{r}_0 \end{cases} \tag{5.37}$$

where $\hat{r}_0$ is the radial location where the swirl velocity transitions from forced to free vortex.

5.2.1.3 Axial and Radial Perturbations Velocities

The perturbation velocities $\hat{u}^*$ and $\hat{v}^*$ can be determined by combining the momentum equations for the axial and radial directions into an equation for the tangential component of vorticity. By differentiating Eq. (5.2) with respect to $\hat{r}$ and Eq. (5.3) with respect to $\hat{z}$, and subtracting one from the other [200], the dependence of the conservation on the pressure gradient is removed. This term describes the vorticity production via the baroclinic mechanism, which occurs when the density and pressure gradients are misaligned, and is often important in flames produced in rotating flows [204]. A single equation can be written in terms of the nondimensional tangential component of vorticity $\hat{\omega}$. Neglecting the streamwise diffusion terms,

$$\frac{\hat{u}}{Re_0}\frac{\partial \hat{\omega}}{\partial \hat{z}} + \hat{v}\frac{\partial \hat{\omega}}{\partial \hat{r}} - \frac{\hat{v}\hat{\omega}}{\hat{r}} - \frac{1}{Re_0}\frac{\partial}{\partial \hat{z}}\left(\frac{\hat{w}^{*2}}{\hat{r}}\right) = \frac{2}{Re_0}\left(\frac{\partial^2 \hat{\omega}}{\partial \hat{r}^2} + \frac{1}{\hat{r}}\frac{\partial \hat{\omega}}{\partial \hat{r}} - \frac{\hat{\omega}}{\hat{r}^2}\right) \tag{5.38}$$

The tangential component of vorticity can also be expanded as,

$$\hat{\omega} = \frac{\partial \hat{v}}{\partial \hat{z}} - \frac{\partial \hat{u}}{\partial \hat{r}} = \left(\frac{\partial \hat{v}^o}{\partial \hat{z}} - \frac{\partial \hat{u}^o}{\partial \hat{r}} \right) + \varepsilon^2 \left(\frac{\partial \hat{v}^*}{\partial \hat{z}} - \frac{\partial \hat{u}^*}{\partial \hat{r}} \right) = \hat{\omega}^o + \varepsilon^2 \hat{\omega}^* \tag{5.39}$$

Substituting Eq. (5.39) together with Eq. (5.12) into Eq. (5.38), and retaining second-order terms only,

$$\frac{\hat{u}^*}{Re_0}\frac{\partial \hat{\omega}^o}{\partial \hat{z}} + \frac{\hat{u}^o}{Re_0}\frac{\partial \hat{\omega}^*}{\partial \hat{z}} + \hat{v}^*\frac{\partial \hat{\omega}^o}{\partial \hat{r}} + \hat{v}^o\frac{\partial \hat{\omega}^*}{\partial \hat{r}} - \frac{\hat{v}^*\hat{\omega}^o}{\hat{r}} - \frac{\hat{v}^o\hat{\omega}^*}{\hat{r}} - \frac{1}{Re_0}\frac{\partial}{\partial \hat{z}}\left(\frac{\hat{w}^{*2}}{\hat{r}}\right) = \frac{1}{Re_0}\left(\frac{\partial^2 \hat{\omega}^*}{\partial \hat{r}^2} + \frac{1}{\hat{r}}\frac{\partial \hat{\omega}^*}{\partial \hat{r}} - \frac{\hat{\omega}^*}{\hat{r}^2}\right) \tag{5.40}$$

which can be further simplified if one notes that, from the continuity equation for the velocity perturbations,

$$\mathcal{O}\left(\frac{\partial^2 \hat{v}^*}{\partial \hat{z}\partial \hat{r}} + \frac{1}{\hat{r}}\frac{\partial \hat{v}^*}{\partial \hat{z}}\right) = \mathcal{O}\left(\frac{1}{Re_0}\frac{\partial^2 \hat{u}^*}{\partial \hat{z}^2}\right) \tag{5.41}$$

The equality in Eq. (5.41) shows that the gradient of the perturbed radial velocity in the scaled axial direction is of the same order of terms that have already been neglected in the analysis. Moreover, by the definition in Eq. (5.16), $\hat{v}^o(\hat{r})$ is a function of $\hat{r}$ only. Therefore,

$$\hat{\omega}^o = -\frac{\partial \hat{u}^o}{\partial \hat{r}} \qquad \text{and} \qquad \hat{\omega}^* = -\frac{\partial \hat{u}^*}{\partial \hat{r}} \tag{5.42}$$

Substituting the expressions for $\hat{\omega}^o$, $\hat{\omega}^*$, $\hat{u}^o$ and $\hat{v}^o$ into Eq. (5.40), we obtain,

$$\frac{\partial^3 \hat{u}^*}{\partial \hat{r}^3} + \left(\frac{Re_w}{2}G + \frac{1}{\hat{r}}\right)\frac{\partial^2 \hat{u}^*}{\partial \hat{r}^2} - \frac{\hat{U}F}{2}\frac{\partial^2 \hat{u}^*}{\partial \hat{z}\partial \hat{r}} - \left(\frac{Re_w}{2\hat{r}}G + \frac{1}{\hat{r}^2}\right)\frac{\partial \hat{u}^*}{\partial \hat{r}} - Re_w F'\hat{u}^* + \frac{Re_0}{2}\hat{U}\left(\frac{F'}{\hat{r}} - F''\right)\hat{v}^* = \frac{1}{2\hat{r}}\frac{\partial}{\partial \hat{z}}\left(\hat{w}^*\right)^2 \tag{5.43}$$

Equation (5.43) must be solved together with the continuity equation for the perturbed velocities,

$$\frac{1}{Re_0}\frac{\partial \hat{u}^*}{\partial \hat{z}} + \frac{1}{\hat{r}}\frac{\partial}{\partial \hat{r}}(\hat{r}\hat{v}^*) = 0 \tag{5.44}$$

The boundary conditions are obtained from Eq. (5.7) and Eq. (5.12),

$$\frac{\partial \hat{u}^*}{\partial \hat{r}} = \hat{v}^* = 0, \quad \hat{r} = 0 \tag{5.45a}$$

$$\hat{u}^* = \hat{v}^* = 0, \quad \hat{r} = 1 \tag{5.45b}$$

$$\hat{u}^* = \hat{v}^* = 0, \quad \hat{z} \to \infty \tag{5.45c}$$

To solve the system composed of Eqs. (5.43) and (5.44) we assume [200],

$$\hat{u}^* = \sum_{n=0}^{5} a_n(\hat{z})\hat{r}^n \tag{5.46}$$

In addition to the two boundary conditions on $\hat{u}^*$ with respect to r, one more can be obtained upon integrating Eq. (5.44),

$$\int_0^1 \hat{u}^*\hat{r}d\hat{r} = 0 \tag{5.47}$$

Furthermore, the polynomial $\hat{u}^*$ is required to satisfy Eq. (5.43) at the wall and at the symmetry axis,

$$\left[\frac{\partial^3 \hat{u}^*}{\partial \hat{r}^3} + \left(\frac{\partial^2 \hat{u}^*}{\partial \hat{r}^2} - \frac{\partial \hat{u}^*}{\partial \hat{r}}\right)\left(1 + \frac{Re_w}{2}\right)\right]_{\hat{r}=1} = 0 \tag{5.48a}$$

$$\left[\frac{\partial^3 \hat{u}^*}{\partial \hat{r}^3} + \left(\frac{\partial^2 \hat{u}^*}{\partial \hat{r}^2} - \frac{1}{\hat{r}}\frac{\partial \hat{u}^*}{\partial \hat{r}}\right)\frac{1}{\hat{r}}\right]_{\hat{r}=0} = 0 \tag{5.48b}$$

The conditions from Eqs. (5.45), (5.47) and (5.48) are sufficient to allow the elimination of five of the polynomial coefficients which can be written in terms of a_0, given in Eq. (5.53).

The perturbed axial velocity can be expressed in terms of the multiplication between an unknown function of the scaled axial coordinate $a_0(\hat{z})$ as,

$$\hat{u}^* = a_0(\hat{z})P(\hat{r}) \tag{5.49}$$

where

$$P(\hat{r}) = 1 - \frac{20(38+3Re_w)}{158+11Re_w}\hat{r}^2 + \frac{105(10+Re_w)}{158+11Re_w}\hat{r}^4 - \frac{56(8+Re_w)}{158+11Re_w}\hat{r}^5 \tag{5.50}$$

From the continuity equation Eq. (5.1), the perturbation velocity $\hat{v}^*$ is given by,

$$\hat{v}^* = -\frac{1}{Re_0}\frac{da_0}{d\hat{z}}Q(\hat{r}) \tag{5.51}$$

where,

$$Q(\hat{r}) = \frac{1}{\hat{r}}\int \hat{r}P(\hat{r})d\hat{r} \tag{5.52}$$

The expressions for $\hat{u}^*$ and $\hat{v}^*$ can be substituted into Eq. (5.43), yielding,

$$\begin{aligned}(\hat{r}P'F + QF' - \hat{r}QF'')\,\hat{U}\frac{da_0}{d\hat{z}} + \\ \left[Re_w\left(2\hat{r}F'P + GP' - \hat{r}GP''\right) + 2\left(\frac{P'}{\hat{r}} - P'' - \hat{r}P'''\right)\right]a_0 = -\frac{\partial}{\partial\hat{z}}(\hat{w}^*)^2\end{aligned} \tag{5.53}$$

In order to solve Eq. (5.53), the solution for $\hat{w}^*$, given in Eq. (5.34), must be squared. This operation results in products of mixed eigenfunctions that can be eliminated through the application of the orthogonality property from Eq. (5.29) [200]. Multiplying Eq. (5.53) by the weight function $\sigma_\phi(\hat{r})$, defined in Eq. (5.28), and integrating with respect to $\hat{r}$,

$$\frac{da_0}{d\hat{z}} + \frac{C_2}{C_1\hat{U}}a_0 = \frac{1}{C_1}\sum_{n=1}^{\infty} B_n\hat{U}^{-(2+\lambda_n/Re_w)} \tag{5.54}$$

which is a linear, non-homogeneous, ordinary differential equation for a_0 with solution,

$$a_0 = A_1 \hat{U}^{-C_2/(2C_1 Re_w)} + \sum_{n=1}^{\infty} \frac{B_n \hat{U}^{-(1+\lambda_n/Re_w)}}{C_2 - 2C_1(Re_w + \lambda_n)} \tag{5.55}$$

where the constant of integration A_1 vanishes, since for $\hat{w}_0^* = 0$, the axial and radial perturbations induced by the tangential velocity component should vanish, i.e., $\hat{u}^* = \hat{v}^* = 0$. The terms B_n, C_1, and C_2 are given, respectively, by,

$$B_n = \frac{2\lambda_n}{||\phi_n||^2} \left[\int_0^1 w_0^* \phi_n \sigma_\phi d\hat{r} \right]^2 \tag{5.56a}$$

$$C_1 = \int_0^1 \left[\hat{r} P' F + Q \left(F' - \hat{r} F'' \right) \right] \sigma_\phi d\hat{r} \tag{5.56b}$$

$$C_2 = \int_0^1 \left[Re_w \left(2\hat{r} F' P + G P' - \hat{r} G P'' \right) + 2 \left(\frac{P'}{\hat{r}} - P'' - \hat{r} P''' \right) \right] \sigma_\phi d\hat{r} \tag{5.56c}$$

In the special case of tubes with impermeable walls, the solution to ordinary the differential equation for a_0, Eq. (5.54), is given by,

$$a_0^0 = \sum_{n=1}^{\infty} \frac{B_n \exp\left(-2\lambda_n \hat{z}\right)}{C_2 - 2C_1 \lambda_n} \tag{5.57}$$

The final form for velocity components is obtained substituting the expressions from Eqs. (5.16), (5.49) and (5.55) into Eq. (5.12),

$$\hat{u} = \hat{u}^o + \varepsilon^2 \hat{u}^* = \hat{U} \left[F + \hat{W}_0^2 P \sum_{n=1}^{\infty} \frac{B_n \hat{U}^{-(2+\lambda_n/Re_w)}}{C_2 - 2C_1(Re_w + \lambda_n)} \right] \tag{5.58a}$$

$$\hat{v} = \hat{v}^o + \varepsilon^2 \hat{v}^* = -\hat{V}_w \left[G - 2\hat{W}_0^2 Q \sum_{n=1}^{\infty} \frac{(1 + \lambda_n/Re_w) B_n \hat{U}^{-(2+\lambda_n/Re_w)}}{C_2 - 2C_1(Re_w + \lambda_n)} \right] \tag{5.58b}$$

The effect of the perturbation induced by the swirl velocity can be estimated by simplifying Eq. (5.58). At the centerline where, from Eq. (5.50), P attains its maximum value $P(0) = 1$, Eq. (5.58) shows that the axial perturbation velocity $u_{\mathfrak{L}}^*(\hat{z})$ can be scaled

by,

$$\hat{u}^*_{\mathfrak{L}}/\hat{U} = \sum_{n=1}^{\infty} \frac{B_n \hat{U}^{-(2+\lambda_n/Re_w)}}{C_2 - 2C_1(Re_w + \lambda_n)} \tag{5.59}$$

The left side of Eq. (5.59), corresponds to the ratio between the maximum intensity of the perturbation induced by the swirl flow in the axial direction and the maximum intensity of the initial swirl squared. From the choice of perturbation orders, this ratio must be of order $\mathcal{O}(\varepsilon^0)$ or lesser, i.e.,

$$\mathcal{O}\left(\hat{u}^*_{\mathfrak{L}}/\hat{U}\right) = \mathcal{O}\left[\sum_{n=1}^{\infty} \frac{B_n \hat{U}^{-(2+\lambda_n/Re_w)}}{C_2 - 2C_1(Re_w + \lambda_n)}\right] \leqslant \mathcal{O}\left(\varepsilon^0\right) \tag{5.60}$$

The analysis is valid in the portion of the tube where Eq. (5.60) is satisfied.

5.2.2 Scalar Field

The analysis considers a non-dissipative, constant property flow. The conserved scalars can be represented in a form similar to the one used for the velocity components as,

$$Z = Z^o + \varepsilon^2 Z^* + \mathcal{O}(\varepsilon^3) \tag{5.61a}$$

$$H = H^o + \varepsilon^2 H^* + \mathcal{O}(\varepsilon^3) \tag{5.61b}$$

in which the subscript o denotes $\mathcal{O}(\varepsilon^0)$ terms, i.e., the values of scalars obtained for the undisturbed flow field and the values of the scalars far downstream, where perturbations have dissipated. The terms $\varepsilon^2 Z^*$ and $\varepsilon^2 H^*$ are perturbations to the conserved scalars, $\mathcal{O}(\varepsilon^2)$ terms. The procedure used to solve the conservation equations for both conserved scalars is equivalent. Thus, without loss of generality, the development only for the excess enthalpy is presented completely.

5.2.2.1 Undisturbed Scalar Field

The undisturbed scalar field is obtained through the solution of the conservation equation for the conserved scalar, Eq. (2.43), retaining only order zero terms, which is given by,

$$\frac{\hat{u}^o}{Re_0}\frac{\partial H^o}{\partial \hat{z}} + \hat{v}^o\frac{\partial H^o}{\partial \hat{r}} = \frac{2}{Pe_0}\left[\frac{1}{\hat{r}}\frac{\partial}{\partial \hat{r}}\left(\hat{r}\frac{\partial H^o}{\partial \hat{r}}\right)\right] \tag{5.62}$$

Substituting the velocity components given in Eq. (5.16) into Eq. (5.62),

$$\frac{2}{F}\left[\frac{\partial^2 H^o}{\partial \hat{r}^2} + \left(\frac{Pe_w}{2}G + \frac{1}{\hat{r}}\right)\frac{\partial H^o}{\partial \hat{r}}\right] = \hat{U}Pr\frac{\partial H^o}{\partial \hat{z}} \tag{5.63}$$

in which $Pr \equiv \nu/\alpha$ is the Prandtl number. Introducing Eq. (5.61) into Eq. (5.10), the boundary conditions for Eq. (5.62) read,

$$\left.\frac{\partial H^o}{\partial \hat{r}}\right|_{\hat{r}=0} = H^o(1,\hat{z}) - H_w = H^o(\hat{r},0) = 0 \tag{5.64}$$

and the flux of H^o at the wall, from Eq. (5.11), can be obtained from,

$$\frac{2}{Pe_0}\left.\frac{\partial H^o}{\partial \hat{r}}\right|_{\hat{r}=1} = \hat{v}_{w_-}\hat{L}_{eff} \tag{5.65}$$

The boundary conditions in the radial direction for H and, consequently, H^o are not homogeneous. For the case of non-zero prescribed excess enthalpy value or flux at the wall, a new dependent variable $\Theta(\hat{z},\hat{r})$ is introduced in order to simplify the calculations. Both sides of Eq. (5.63) are functions of only one independent variable. However, the boundary conditions for H in the radial direction are not both homogeneous. Introducing the transformation,

$$\Theta = -(H^o - H_w)/H_w \tag{5.66}$$

the conservation equation Eq. (5.62) becomes,

$$\frac{2}{F}\left[\frac{\partial^2\Theta}{\partial\hat{r}^2}+\left(\frac{Pe_w}{2}G+\frac{1}{\hat{r}}\right)\frac{\partial\Theta}{\partial\hat{r}}\right]=\hat{U}Pr\frac{\partial\Theta}{\partial\hat{z}} \tag{5.67}$$

with boundary conditions,

$$\left.\frac{\partial\Theta}{\partial\hat{r}}\right|_{\hat{r}=0}=\Theta(\hat{z},1)=\Theta(0,\hat{r})-1=0 \tag{5.68}$$

The solution is obtained by the separating $\Theta(\hat{z},\hat{r})$ as,

$$\Theta(\hat{z},\hat{r})=X(\hat{z})R(\hat{r}) \tag{5.69}$$

Substituting Eqs. (5.66) and (5.69) into Eq. (5.62),

$$\frac{2}{FR}\left[\frac{d^2R}{d\hat{r}^2}+\left(\frac{Pe_w}{2}G+\frac{1}{\hat{r}}\right)\frac{dR}{d\hat{r}}\right]=\hat{U}Pr\frac{1}{X}\frac{dX}{d\hat{z}}=-\beta^2 \tag{5.70}$$

The solution for the axial direction is obtained by integrating the equation for $X(\hat{z})$ as,

$$X(\hat{z})=b_1\hat{U}^{-\beta^2/Pe_w} \tag{5.71}$$

where b_1 is a constant of integration. The equation for $R(\hat{r})$ is given by,

$$\frac{d^2R}{d\hat{r}^2}+\left(\frac{Pe_w}{2}G+\frac{1}{\hat{r}}\right)\frac{dR}{d\hat{r}}+\beta^2\frac{F}{2}R=0 \tag{5.72}$$

which can be cast into Sturm-Liouville form through the introduction of an integrating factor,

$$q_R(\hat{r})=\exp\int\left(\frac{Pe_w}{2}G+\frac{1}{\hat{r}}\right)d\hat{r} \tag{5.73}$$

yielding,

$$\frac{d}{d\hat{r}}\left(q_R\frac{dR}{d\hat{r}}\right)+\beta^2\sigma_R R=0 \tag{5.74}$$

where the weight function $\sigma_R(\hat{r})$ is given by,

$$\sigma_R(\hat{r})=q_R F/2 \tag{5.75}$$

such that the orthogonality property of the eigenfunctions $R_n(\hat{r})$ is given by,

$$\int_0^1 R_m(\hat{r})R_n(\hat{r})\sigma_R(\hat{r})d\hat{r}=\delta_{mn}||R_n||^2 \tag{5.76}$$

The undisturbed conserved scalar is given by,

$$H^o=H_w(1-\Theta) \tag{5.77}$$

in which,

$$\Theta=\sum_{n=1}^{\infty}b_n R_n X_n \tag{5.78}$$

The solution of Eq. (5.72) for the special case $Re_w=0$,

$$R_n^0(\hat{r})=\exp\left(-\frac{\beta_n}{2}\hat{r}^2\right){}_1F_1\left(\frac{1}{2}-\frac{\beta_n}{4},1,\beta_n\hat{r}^2\right) \tag{5.79}$$

can be used as the initial guess to the solution of Eq. (5.72). For the special case of tubes with impermeable walls,

$$\Theta=\sum_{n=1}^{\infty}b_n R_n^0\exp(-\beta_n^2\hat{z}/Pr) \tag{5.80}$$

The boundary condition at $\hat{r} = 0$ is automatically satisfied, and the remaining boundary condition at $\hat{r} = 1$ is used to determine the eigenvalues β_n^2. The constants b_n are determined such that H^o equals the boundary condition at $\hat{z} = 0$. Hence,

$$b_n = \frac{1}{||R_n||^2} \int_0^1 R_n \sigma_R d\hat{r} \tag{5.81}$$

where the norm $||R_n||^2$ and the weight function σ_R are defined in Eqs. (5.75) and (5.76), respectively.

5.2.2.2 Axial and Radial Perturbations to the Scalar Field

Substituting the expressions for the velocity components from Eq. (5.16) and for the excess-enthalpy from Eq. (5.61) into Eq. (2.43), and retaining only second-order terms,

$$\frac{\hat{u}^o}{Re_0}\frac{\partial H^*}{\partial \hat{z}} + \hat{v}^o\frac{\partial H^*}{\partial \hat{r}} - \frac{2}{Pe_0}\frac{1}{\hat{r}}\frac{\partial}{\partial \hat{r}}\left(\hat{r}\frac{\partial H^*}{\partial \hat{r}}\right) = -\left(\frac{\hat{u}^*}{Re_0}\frac{\partial H^o}{\partial \hat{z}} + \hat{v}^*\frac{\partial H^o}{\partial \hat{r}}\right) \tag{5.82}$$

where the terms on the right-hand side of the equality are known. Equation (5.82) is a nonhomogeneous partial differential equation that satisfies the boundary conditions,

$$\left.\frac{\partial H^*}{\partial \hat{r}}\right|_{\hat{r}=0} = H^*(1, \hat{z}) = H^*(\hat{r}, 0) = 0 \tag{5.83}$$

The solution to Eq. (5.82) is sought through the eigenfunction expansion method. The perturbation to the scalar field H^* is given in terms of the eigenfunctions $R_n(\hat{r})$, which are the eigenvectors of the Sturm-Liouville system obtained from the solution of the associated homogeneous problem to Eq. (5.82) as,

$$H^*(\hat{z}, \hat{r}) = \sum_{n=1}^{\infty} X_n^*(\hat{z}) R_n(\hat{r}) \tag{5.84}$$

The associated homogeneous problem to Eq. (5.82) has the same form of Eq. (5.62). For that reason, the eigenfunctions used in the expansion Eq. (5.84) are the same as the ones in Eq. (5.78). Substituting the velocity components given in Eq. (5.16) into Eq. (5.82) and using transformed dimensionless coordinates,

$$\frac{1}{F}\left\{\frac{2}{Pr}\left[\frac{\partial^2 H^*}{\partial \hat{r}^2}+\left(\frac{Pe_w}{2}G+\frac{1}{\hat{r}}\right)\frac{\partial H^*}{\partial \hat{r}}\right]-\left(\hat{u}^*\frac{\partial H^o}{\partial z}+Re_0\hat{v}^*\frac{\partial H^o}{\partial \hat{r}}\right)\right\}=\hat{U}\frac{\partial H^*}{\partial \hat{z}} \tag{5.85}$$

The last two terms on the left hand side of the conservation equation for the perturbed scalar field Eq. (5.85) are known and can be expanded by,

$$\frac{\hat{u}^*}{F}\frac{\partial H^o}{\partial \hat{z}}=a_0\frac{P}{F}\frac{\partial H^o}{\partial \hat{z}}=-H_w\sum_{n=1}^{\infty}\hat{u}_n^*(\hat{z})R_n(\hat{r}) \tag{5.86a}$$

$$Re_0\frac{\hat{v}^*}{F}\frac{\partial H^o}{\partial \hat{r}}=-\frac{da_0}{d\hat{z}}\frac{Q}{F}\frac{\partial H^o}{\partial \hat{r}}=-H_w\sum_{n=1}^{\infty}v_n^*(\hat{z})R_n(\hat{r}) \tag{5.86b}$$

such that the coefficients $\hat{u}_n^*(\hat{z})$ and $v_n^*(\hat{z})$ are obtained through the the application of the orthogonality property of $R_n(\hat{r})$, Eq. (5.76), to Eq. (5.86), yielding,

$$\hat{u}_n^*(\hat{z})=\frac{1}{2\,||R_n||^2}a_0\sum_{k=1}^{\infty}b_k\frac{dX_k}{dz}\int_0^1 PR_kR_nq_Rd\hat{r} \tag{5.87a}$$

$$v_n^*(\hat{z})=-\frac{1}{2\,||R_n||^2}\frac{da_0}{d\hat{z}}\sum_{k=1}^{\infty}b_kX_k\int_0^1 Q\frac{dR_k}{dr}R_nq_Rd\hat{r} \tag{5.87b}$$

Substituting the expansions Eq. (5.86), the velocity components defined in Eq. (5.16), and the transformed coordinates into Eq. (5.82) yields,

$$\frac{2}{FR_n}\left[\frac{\partial^2 R_n}{\partial \hat{r}^2}\left(\frac{Pe_wG}{2}+\frac{1}{\hat{r}}\right)\frac{\partial R_n}{\partial \hat{r}}\right]X_n^*+PrH_w(\hat{u}_n^*+\hat{v}_n^*)=\hat{U}Pr\frac{dX_n^*}{d\hat{z}} \tag{5.88}$$

The term multiplying X_n^* is can be replaced by the eigenvalues β_n correspondent to the solution of the associated homogeneous problem to Eq. (5.82). Each term in the sum satisfies,

$$\frac{dX_n^*}{d\hat{z}} + \frac{\beta_n^2}{\hat{U}Pr} X_n^* = H_w \frac{\hat{u}_n^* + v_n^*}{\hat{U}} \tag{5.89}$$

Equation (5.89) is an ordinary differential equation in X_n^* with solution,

$$X_n^*(\hat{z}) = \sum_{n=1}^{\infty} \hat{U}^{-\beta_n^2/(2Pe_w)} \left\{ b_n^* + H_w \int_0^{\hat{z}} [\hat{u}_n^*(t) + \hat{v}_n^*(t)][\hat{U}(t)]^{-1+\beta_n^2/(2Pe_w)} dt \right\} \tag{5.90}$$

where the constants b_n^* vanish, because of the boundary condition at $\hat{z} = 0$. This is justified from the assumption of perturbations to the scalar field being due solely to the axial and radial velocity perturbations induced by the tangential velocity component. Therefore, the solution of the homogeneous version of Eq. (5.82) (i.e., for the case in which the right-hand side of Eq. (5.82) vanishes) is $H^* = 0$. The perturbed scalar field is given, in its final form, for any Re_w, assuming (for simplicity of representation) the same number of terms in the sums for H^o Eq. (5.77) and H^* Eq. (5.84) as,

$$H(\hat{z}, \hat{r}) = H_w \Bigg\{ 1 - \sum_{n=1}^{\infty} R_n \hat{U}^{-\beta_n^2/(2Pe_w)} \times \left[b_n - \hat{W}_0^2 \int_0^{\hat{z}} [\hat{u}_n^*(t) + \hat{v}_n^*(t)][\hat{U}(t)]^{-1+\beta_n^2/(2Pe_w)} dt \right] \Bigg\} \tag{5.91}$$

The perturbed temperature field can be obtained by substituting back the result of the conserved scalar field from Eq. (5.91) into Eq. (2.45b). Fuel and oxidizer mass fraction fields can be obtained by replacing H with Z in Eq. (5.91) and substituting back the result into Eq. (2.45a).

5.3 Discussion

The solution to the undisturbed velocity field in a porous tube has been extensively discussed by several authors [see 176–180]. It has been observed that different injection velocities at the wall alter significantly the dynamic behavior and the existence of solutions for the fluid flow [see 180, 205–210]. The wall Reynolds number Re_w depends on the liquid fuel evaporation rate, which is a characteristic of the fuel considered. Therefore, the choice of different fuels results in different balances between Stefan convection and diffusion (on the gas side) and convection (on the liquid side). The axial Reynolds number Re_0 and the swirl angle θ also influence the flow field. Sufficiently large Re_0 guarantees that streamwise diffusion is negligible compared to diffusion in the radial direction as long as the flow remains laminar. The axial Reynolds number also controls the length of the developing region through the scaled axial coordinate $\hat{z}$ — which is equivalent to the inverse Graetz number multiplied by Pr — that depends on Re_0. Small swirl angles are necessary for the validity of the model, while providing the circumferential velocity component to the flow field. The influence of those parameters on a non-reacting system is evaluated before proceeding with the full solution, where the combination of all physical effects on the system is examined.

5.3.1 Wall Reynolds Number

The similarity variable $F = \hat{u}^o/\hat{U}$ defined in Eq. (5.16), regarded as the fully developed velocity profile, is a function of the radial coordinate $\hat{r}$ only. Figure 5.3 presents the profiles for $\hat{u}^o/\hat{U}$ for several wall Reynolds numbers. A small change occurs in the profiles, with the nondimensional centerline velocity varying from about 1.6 for a wall with large injection to 2.0 for no injection of mass. For the case of a wall with no injection, the Poiseuille parabolic profile is obtained. These results agree with the ones reported in the literature [177–180, 190, 191].

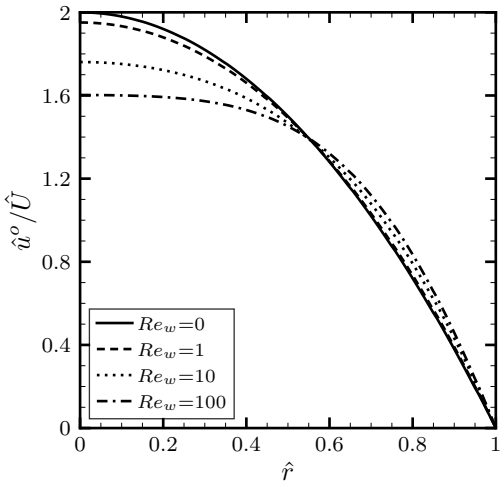

Figure 5.3: Fully developed velocity profiles for wall Reynolds numbers 0, 1, 10 and 100.

It is worth noting that, as in Prandtl's boundary layer theory, the similarity variable F is a function of the radial coordinate stretched in the longitudinal direction. For that reason, the boundary condition at the tube inlet for different values of Re_w is not equivalent to the Poiseuille parabolic profile, but of a Berman [175] flow type [211]. Consequently, close to the inlet, the velocity field obtained through Eq. (5.17) is not expected to match experimental measurements in which the flow is allowed to attain a Poiseuille velocity profile before entering the porous walled tube, but in the downstream region it would asymptotically approach the observations [212].

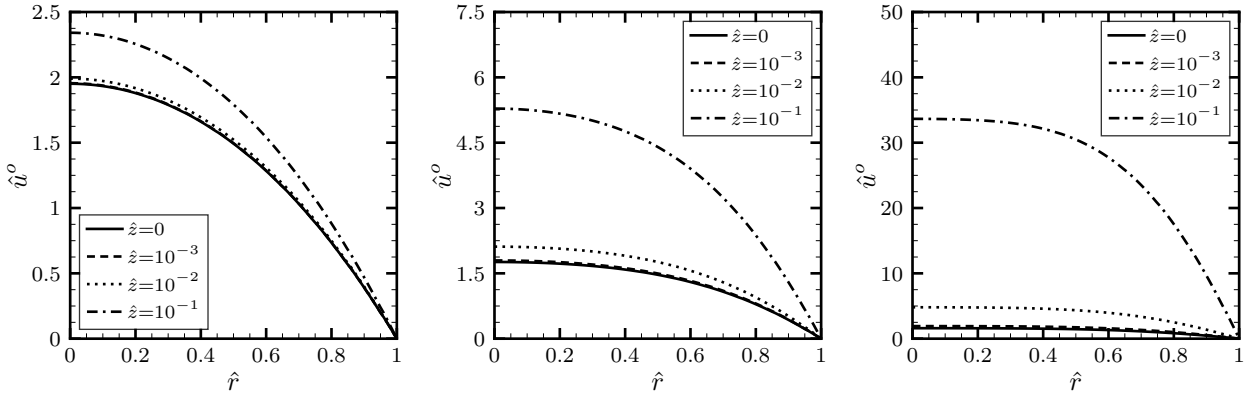

Figure 5.4: Axial velocity component profile at different $\hat{z}$ for selected wall Reynolds numbers. (a) $Re_w = 1$; (b) $Re_w = 10$; (c) $Re_w = 100$.

The wall Reynolds number is defined in terms of the dimensional wall injection velocity $\hat{V}_w$. Equivalently, it can also be described by the axial Reynolds number, as shown in Eq. (5.15). Therefore, the wall Reynolds number provides complete characterization of the dimensionless velocity field of a fluid in a tube with mass injection at the walls. The radial distribution of the axial velocity profiles for different axial positions $\hat{z}$ is shown in Fig. 5.4, where the effect of increasing Re_w is observed.

5.3.2 Swirl Velocity

The decay of the inlet distribution of the swirl velocity component for different axial positions $\hat{z}$ is shown in Fig. 5.5, where the effect of increasing Re_w is observed. It is assumed that the position where the transition from forced to free vortex occurs is $\hat{r}_0 = 0.9$. The plots show the influence of the swirl velocity on the fluid flow without (Fig. 5.5a) and with (Figs. 5.5b and 5.5c) injection of mass through the wall. It is observed that the decay of the swirl velocity with z decreases with increasing values of the wall injection Reynolds number. This effect is shown more clearly in Fig. 5.7a where the maximum value of the swirl velocity is plotted as a function of the scaled axial coordinate $\hat{z}$ for the same values of wall injection Reynolds numbers. As observed by Kinney and Sparrow [200], the decay of swirl velocity has a boundary layer character that confines the retarding action of the tube wall to the inner region (a layer adjacent to the wall surface) and the initial swirl distribution to the outer region. Figure 5.5 shows that the thickness of the inner layer is a function of the wall injection Reynolds number Re_w.

Following previous analyses in which the axial and radial perturbations induced by the swirl velocity were calculated, only the first term in the series in Eq. (5.58) is taken into account [195, 200]. The first term in the series is dominant at axial locations $\hat{z} > 10^{-2}$. If all terms in the expansion were included the decay of the perturbation induced by the swirl to

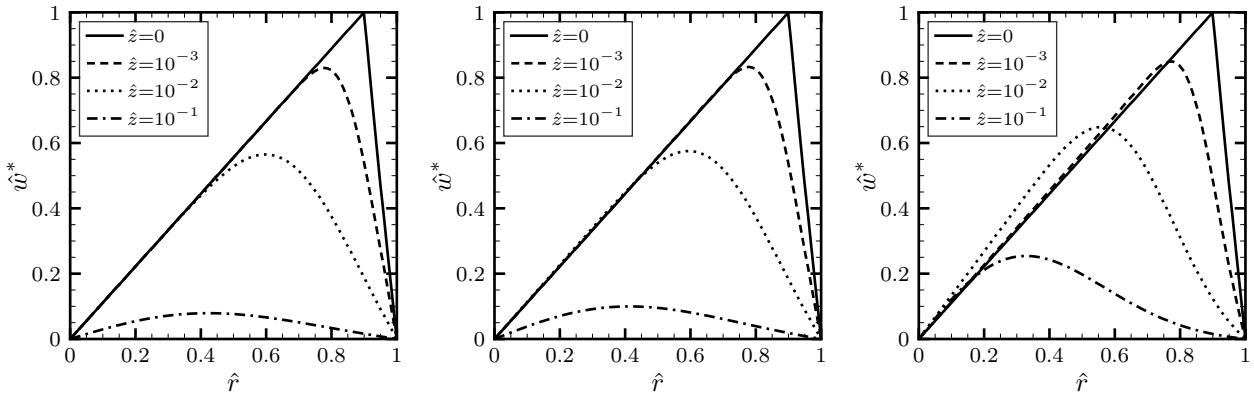

Figure 5.5: Tangential velocity component profile at different $\hat{z}$ for selected wall Reynolds numbers. (a) $Re_w = 0$; (b) $Re_w = 1$; (c) $Re_w = 10$.

the axial velocity would not be monotonic for all Re_w, which is consistent mathematically but not physically. Each mode K_n in the sum in Eq. (5.59), where,

$$K_n \equiv \frac{B_n \hat{U}^{-(2+\lambda_n/Re_w)}}{C_2 - 2C_1(Re_w + \lambda_n)} \tag{5.92}$$

has a varying influence on the total because of their different dependency on Re_w. Hence, from Eq. (5.59), each mode decays monotonically, as observed in Fig. 5.6 for n from 1 to 5, but their sum need not behave the same way. Therefore, the decay of each term represents correctly the influence of the swirl perturbation on other velocity components, but the sum does not. This behavior is mainly due to the lack of higher order terms that would include corrections for the diffusion of the induced perturbation.

The perturbation due to the swirl influences the axial and radial velocity components. Therefore, as the initial swirl decays so does the effect it induces in the other velocity components. The maximum swirl intensity and the perturbation induced by the swirling flow in the axial velocity at the center line are shown in Fig. 5.7 for selected Re_w as a function of the scaled axial coordinate $\hat{z}$. The results from Fig. 5.7b should be taken with care. It is important to point out that the axial and radial perturbations due to the swirl are

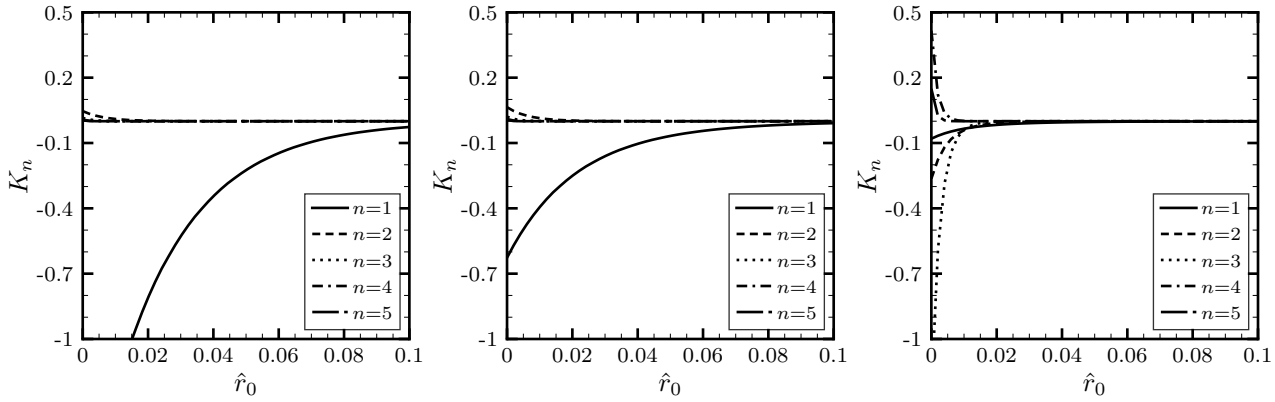

Figure 5.6: Modes K_n as functions of $\hat{z}$ for selected wall Reynolds numbers. (a) $Re_w = 0$; (b) $Re_w = 1$; (c) $Re_w = 10$.

$\mathcal{O}(\varepsilon^2)$ effects and that the mass injection through the walls creates an increase in the mean axial velocity several orders of magnitude greater than the swirl induced perturbation.

The effect of the inlet swirl intensity can also be evaluated. It is observed from Fig. 5.7b that the axial perturbation is strongly influenced by the magnitude of the injection of mass through the tube walls. Therefore, as Re_w increases, a larger $\hat{W}_0$ is needed for the radial and axial velocity components to be affected by the perturbations due to the swirl. At the same time, Eq. (5.60) imposes a limiting restriction to the model at the inlet. In the vicinity of that region, the swirl intensity is maximum, and the magnitude of the induced perturbation is limited by its order. From Fig. 5.7b, it is observed that Eq. (5.60) is indeed satisfied, i.e., $\mathcal{O}(\hat{u}^*_{\mathfrak{C}}/U) \leqslant \mathcal{O}(\epsilon^0)$. The maximum intensity W_0 is assumed to be around 0.5[†], which corresponds to an inlet flow swirl angle θ of approximately 27°. As observed from Fig. 5.7b, the chosen $\hat{W}_0$ induces axial perturbations of absolute values as large as 0.48, 0.16 and 0.02 for $Re_w = 0$, 1 and 10, respectively.

A prescribed inlet swirl velocity distribution $\hat{w}^*_0$, given in Eq. (5.37), is considered. For such velocity distribution, the maximum intensity of the swirl is not solely responsible for

[†]This value for the maximum swirl intensity minimally satisfies the constraints imposed by the perturbation orders.

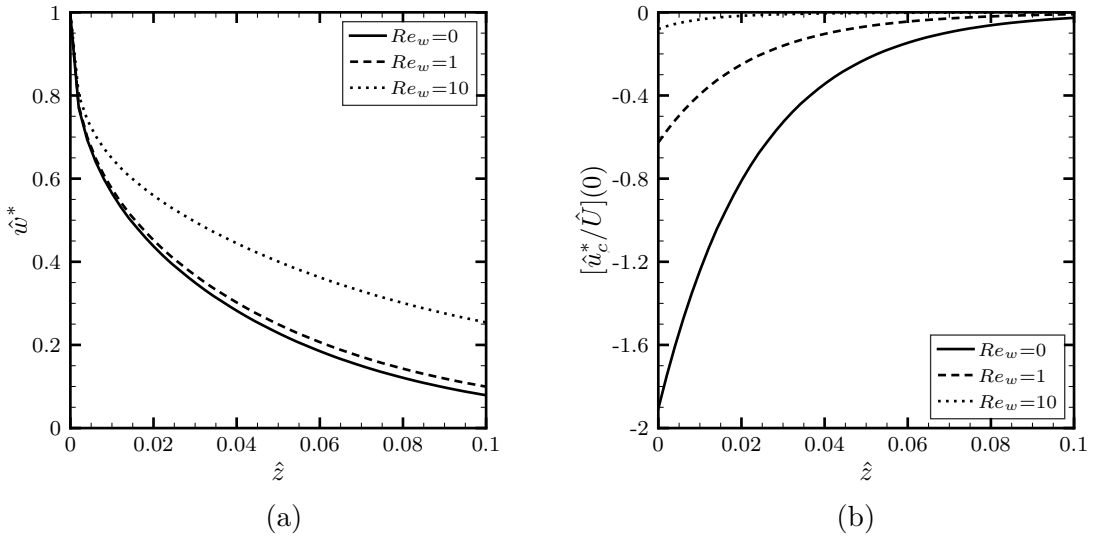

(a) (b)

Figure 5.7: Peak values of the velocity components as a function of $\hat{z}$ for selected wall Reynolds numbers. (a) Swirl velocity; (b) Axial perturbation velocity.

the perturbation, even though it defines its order. The term B_n, defined in Eq. (5.56a), which can be seen as a projection of the function $\hat{w}_0^*$, represents the normalized inlet swirl radial profile squared. Therefore, the magnitude of the perturbation is also influenced by the radial distribution of $\hat{w}_0^*$. The effect of different values of $\hat{r}_0$ on $\hat{u}_{\mathfrak{L}}^*$ at $\hat{z} = 0$ is presented in Fig. 5.8. For the position where the transition from forced to free vortex occurs $\hat{r}_0$ greater than 0.7, which would correspond to commonly observed conditions, the influence of the position where the swirl velocity transitions from forced to free vortex is reduced. At the same time, the larger the injection, the smaller will be the effect of the inlet swirl distribution on the axial induced perturbation. The results in Fig. 5.8 also show that larger perturbation is created for $\hat{r}_0 \simeq 0.6$. This parameter could be considered in the design of swirl vanes that are intended to induce larger perturbations.

5.3.3 Perturbed Scalar Field

Before proceeding to the analysis of the system, the solution for the scalar field is presented. Since it is assumed that the boundary condition at the wall is of the first-type, i.e., a

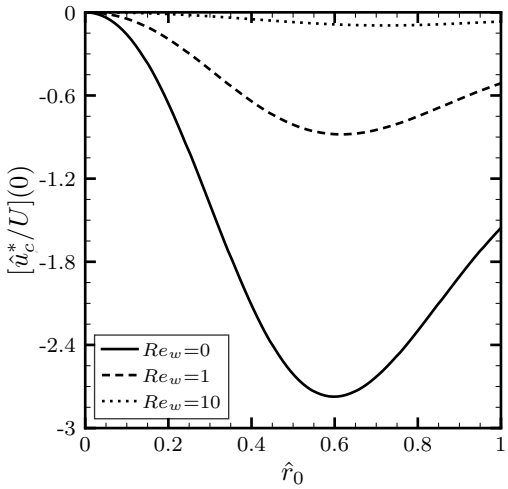

Figure 5.8: Maximum intensity of the axial perturbation induced by the swirl flow at the inlet versus $\hat{r}_0$ for wall Reynolds numbers 0, 1, 10.

prescribed value for the conserved scalar, the solution for both the mixture fraction Z and excess enthalpy H can be scaled in terms of the function Θ, defined in Eq. (5.78). The solution for the perturbed fields for wall Reynolds numbers 1 and 10, for selected radial positions, as a function of the scaled axial coordinate $\hat{z}$ is presented in Fig. 5.9. The solution for the case of impermeable walls ($Re_w = 0$) is not shown in Fig. 5.9 because in the present model fuel evaporates from the wall, so Re_w is always greater than zero.

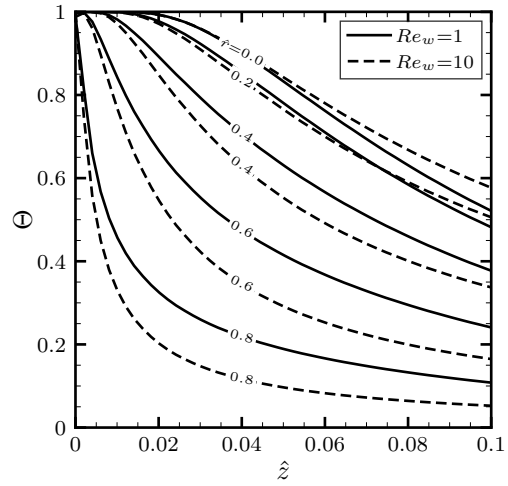

Figure 5.9: Variation of Θ with $\hat{z}$ at selected radial positions for wall Reynolds 1 and 10.

The effect of the perturbations induced by the swirl velocity on the scalar field are prominent in the inner region, i.e., in the zone close to the wall surface. That occurs because the swirl

improves mixing in the inner region, while in the outer region, where a free vortex like structure exists, mixing is not favored. As a consequence, in the inner zone, the transport from the walls is increased in comparison to the undisturbed case.

5.4 Results

The theoretical model is employed in analyzing the structure of nonpremixed swirl-type tubular flames. The generality of the formulation allows it to be applied to various conditions. However, we will limit some parameters in order to analyze systems for which experimental studies would be of interest.

The flows considered in this analysis are laminar, such that their Reynolds numbers are of the order of hundreds, or a few thousands. Consequently, the range of values for the scaled axial coordinate $\hat{z}$ of interest does not extend up to higher values. Results are discussed considering $Re_0 = 500$ and the burner axial length $\hat{z}_{\max} = 0.02$. This choice does not limit the application of the theoretical model, but allows a physical interpretation that matches existing small-scale tubular flame systems, in which the length of the burner is commonly not greater than ten times its inner radius. The evaluation of the solution for a smaller portion of the domain also allows the analysis to be focused on the region where the influence of the swirling flow is more prominent, as observed in Fig. 5.7. It also means that, at the exit port of the burner, a swirling flow would still be found.

The intensity of Stefan convection, i.e., the vaporization rate of the fuel from the porous walls, determines the range of Re_w, which can be estimated roughly from an overall mass conservation at the flame, assuming stoichiometric burning. If all the entraining air and injected fuel up to the axial location $\hat{z}_{\max}$ were completely consumed at the flame sheet, the

mass flow rates of air and fuel necessary for the stoichiometric burning would be,

$$2SRe_w\hat{z}_{\max} = 1 \tag{5.93}$$

which can be employed to determine the values of $\hat{V}_w$ used as a starting estimate for the Stefan convection velocity. It is worth noting that Eq. (5.93) shows that for a fuel burning stoichiometrically, longer tubes would require lower wall injection Reynolds numbers. Assuming the maximum length of the tube as $\hat{z}_{\max}$, the choice of fuel will influence the conserved scalar field through Re_w, via its latent heat of vaporization $\hat{L}$, and the amount of heat release from the chemical reaction though γ. These parameters do not vary significantly for alkanes found in condensed phase in standard conditions. From Eq. (5.93), the values of Re_w for hexane, heptane and octane are, approximately, 1.7. At the same time, for those hydrocarbons, experimental peak flame temperatures are $\hat{T}_S \simeq 4.5$ which corresponds to $\gamma \simeq 4.5$. For that reason we will consider a single condition, which would correspond to any of those alkanes in liquid phase at ambient temperature.

In order to determine $\hat{V}_w$ the procedure described in Section 5.2 is employed. An initial guess is considered to calculate the excess enthalpy field, and Eq. (5.11b) is used to correct $\hat{V}_w$ until its value is equal to the average of $\hat{v}_{w\_}$ over the length of interest. The axial distance $\hat{z}$ over which the mean value is obtained spans the final 80% of the tube. The approximation of $\hat{v}_{w\_}$ by a constant value $\hat{V}_w$ corresponds to its zeroth order, and can be relaxed by employing a formulation in which a nonuniform Re_w is assumed, for example, by considering a local pressure-dependent injection [211, 213]. With the correct approximation for Re_w, the perturbed vector and scalar fields can be sought.

Contours of the nondimensional temperature field and mass fractions are presented in Figs. 5.10a and 5.10b, respectively. The flame position, obtained as the location where the mixture fraction satisfies Eq. (2.46), is highlighted. The contour levels represent the

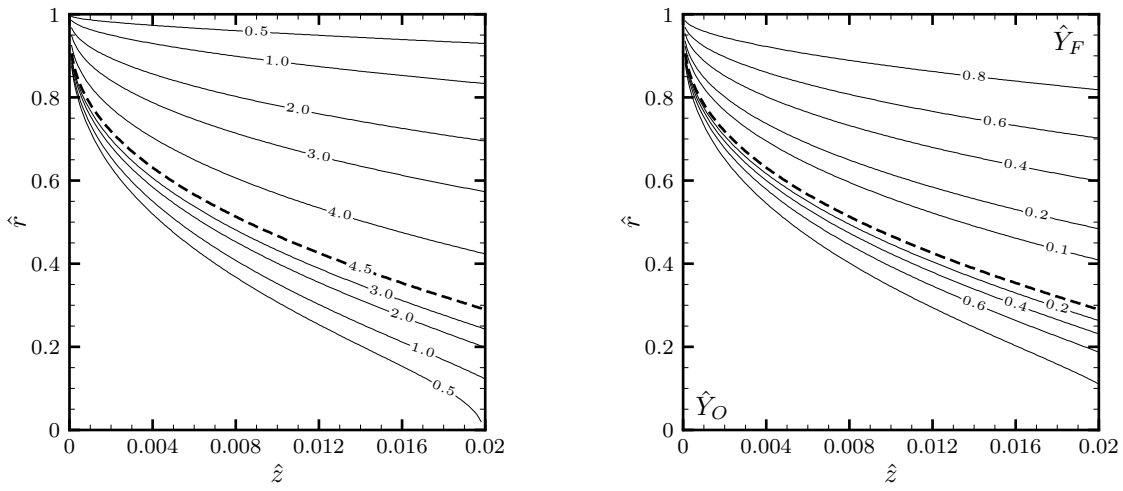

Figure 5.10: Contours of dimensionless scalar fields. The dashed line represents the flame sheet. (a) Temperature; (b) Mass fraction.

nondimensional temperature. The fuel side and the oxidizer side are indicated in Fig. 5.10b by $\hat{Y}_F$ and $\hat{Y}_O$, respectively, where the levels represent the nondimensional mass fractions on each side. It is observed that, even though the flame gets closer to the axis of the tube in the downstream region, the tube is not long enough for the flame sheet to close before the tube outlet. The calculated wall injection Reynolds number is approximately 9. That corresponds to a fuel rich condition, considering the stoichiometric value 1.7 obtained from relation Eq. (5.93). Even though the stoichiometric and the calculated Re_w are of the same order of magnitude, it is important to point out that the solution does not incorporate other thermal losses that could be added to the effective latent heat of vaporization to reduce the estimated fuel injected using Eq. (5.11b). At the same time, effects such as finite rate chemistry, variations of transport and thermodynamic properties with temperature or concentration, radiation losses, nonequilibrium temperature effects between the porous matrix and the liquid phase, radial or axial temperature variations in the wall, axial heat transfer in the porous matrix, spatial variation of the vaporization rate, among several others are not considered in the solution. Therefore, given the approximations involved, the analytical result is expected to predict only qualitatively flame characteristics, similarly

to the solution obtained by the Burke-Schumann model for coflow flames. Indeed, the nonpremixed flame established in this configuration resembles the latter solution for the so called underventilated case. In this condition, the flame is established above a coflow burner from which the amount of air issued is smaller than that necessary to burn all the injected fuel, and the flame extends into the oxidizer region. The nondimensional temperature and species contours in Fig. 5.10 possess the same characteristics.

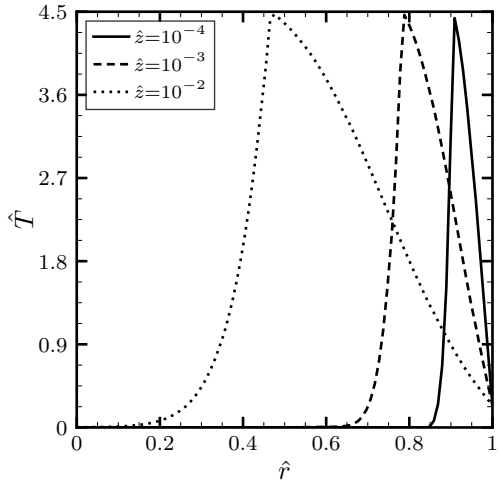

Figure 5.11: Variation of nondimensional temperature with $\hat{r}$ at selected axial positions.

The fuel-rich inlet conditions and the results from Fig. 5.10b indicate that a mixture of unburned fuel and products is found at the burner outlet. This condition resembles the experimental observations for the miniature liquid film burner [82]. Results in the downstream region of the combustion chamber, i.e., after the exit port, cannot be predicted by the model, but the characteristic of the external flame can be qualitatively estimated. As a consequence of the absence of tube walls that constrain the flow and act as a fuel source to the chemical reaction at axial positions greater than the burner length $\hat{z}_{\max}$, the flame would expand outwardly in the radial direction due to the centrifugal force, and would not possess a tubular shape anymore, but would be conical. The external flame shape would also be due to the excess air found in the environment reacting with the mixture of hot unburned fuel and products if the burner is exposed to normal ambient conditions.

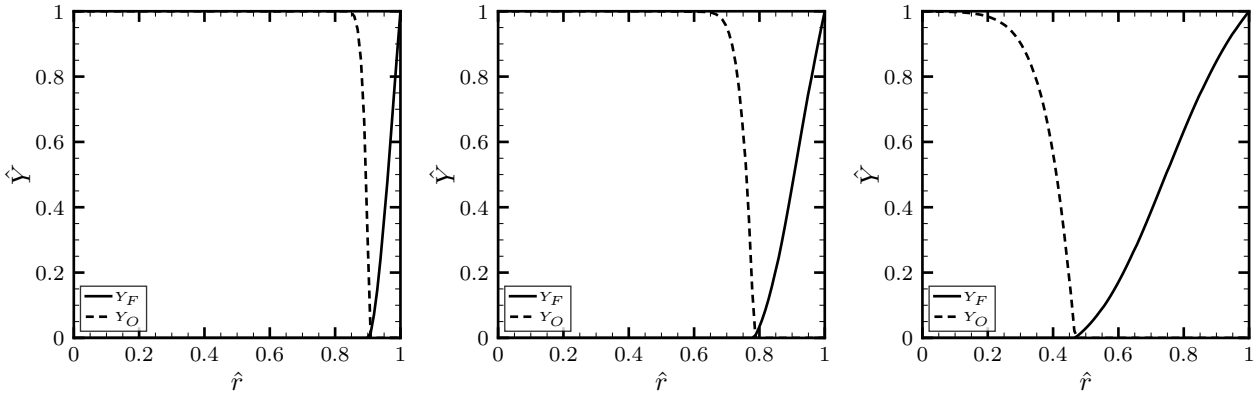

Figure 5.12: Variation of nondimensional mixture fraction profiles at selected axial positions. (a) $\hat{z} = 10^{-4}$; (b) $\hat{z} = 10^{-3}$; (c) $\hat{z} = 10^{-2}$.

Dimensionless temperature and mixture fraction profiles are shown, respectively, in Figs. 5.11 and 5.12 for selected axial positions as a function of the radial coordinate $\hat{r}$. The variation of the temperature and mixture fraction along the radial direction resembles the profiles obtained in nonpremixed counterflow configurations for axial locations near the inlet as expected for a nonpremixed system. The flame is located, for each of the axial positions $\hat{z}$ as the temperature peak, in Fig. 5.11, and as the minima, in Fig. 5.12. The effect of the flame sheet extending into the oxidizer region for larger axial locations is clearly observed.

5.5 Model Validation

The assumptions considered in the theoretical model can be confronted with the experimental observations. Although simplified, some of the overall characteristics of the system are well mathced with the analytical findings. The burning working-map obtained experimentally from Fig. 4.8 can be nondimensionalized considering the scaling parameters defined in Section 5.2. The measured points are shown in Table 5.1.

Table 5.1: Nondimensional stable conditions.

	Re_0	Re_w
Theoretical	500	9.0
Experimental	795	1.7 to 2.4
	990	1.7 to 2.7
	1180	2.0 to 2.6

The calculated value for the wall Reynolds number ($Re_w \simeq 9$) obtained theoretically captures the order of magnitude of the experimental observation. It is observed that the model predicts that a stable flame is established for fuel-rich inlet conditions. At the same time, the measured wall temperatures for quasi-steady flames show that the assumption of prescribed temperature at the fuel boiling point for the boundary condition at the tube surface seems to adequately represent the system. For conditions in which a stable flame is obtained, the maximum wall temperature is relatively close to the boiling point of the fuel. The theoretical model also predicts that the tubular flame produced inside the combustor continues to burn with the ambient air above the rim, even though its structure cannot be fully described.

Disclosure statement

This chapter, in part, has been published or submitted for publication in V. M. Sauer, F. F. Fachini, D. Dunn-Rankin, Structure of Nonpremixed Swirl-Type Tubular Flames Burning Condensed Fuels with Unity Lewis Numbers, in: 10th US National Combustion Meeting, College Park, MD, 1–6, 2017 and V. M. Sauer, F. F. Fachini, D. Dunn-Rankin, Nonpremixed Swirl-Type Tubular Flames Burning Liquid Fuels, J. Fluid Mech. (2017) Under review. The thesis author is the primary investigator in these publications.

Chapter 6

Conclusions

This manuscript includes analysis and some supporting experiments to understand important canonical flame configurations in which fuel and oxidizer are not premixed. The dissertation concentrates on novel orientations where stagnation flows are important and further explores the potential for tubular flames as a characteristic flame system. In all cases, the analyses, though simplified in their chemistry and physical properties, give good insights into several dominant flame behaviors.

Classical theoretical models are extended in order to analyze nonpremixed flames stabilized between an axisymmetric coflow burner and a downstream plate that produces a stagnating flow field. Two approaches previously developed as extensions to the Burke-Schumann theory are modified in order to be applied in the analysis: the Extended Roper (ER) model and the Stream Function as a Coordinate (SFC) model. The semi-analytical models are used to determine the distance between the impinging plate and the burner tip on a methane-air flame. The solutions are compared with experimental data for different vertical positions for the stagnation plate with respect to the burner port. The results show that both models can be employed to estimate flame shapes and the position at which the flame transitions from

a closed tip configuration to an open tip one. The results obtained with the SFC model are, overall, in better agreement with the experimental data. The ER model seems to suffer from the approach considered to account for temperature variations of the physical properties from the burner port to the flame region. The models obtained in this study are not limited to the conditions discussed herein. Situations in which body forces are important, such as the case of a flame in an electric or magnetic field can be also analyzed.

The simplified solutions for water-laden nonpremixed counterflow flames and opposed-flow tubular flames show good agreement with both numerical and theoretical results. Accurate experimental results are still needed for the validation of water-lade flames. At the same time, experimental results also necessary for complete characterization of the proposed nonpremixed counterflow tubular flame burning liquid fuels.

The nonpremixed counterflow-type tubular flame configuration was proposed and its solution presented in a simplified framework. The development of an experimental system is still necessary for model validation.

The porous based nonpremixed tubular burner demonstrates very promising combustion behavior as compared to mesoscale film combustors. Operating limits are expanded and the burner walls remain cool. Further details of combustion efficiency, emissions, as well as the use of materials with different thermal conductivity are recommended for future work.

A theoretical model for nonpremixed swirl-type tubular flames burning condensed fuels with unity Lewis numbers was presented. The formulation allows the determination of the velocity, temperature and species fields. The solution is presented considering a similarity variable transformation for axisymmetric incompressible viscous flow fields. Axial decay of the initial swirl velocity, its induced axial and radial perturbations to the flow, temperature and species field together with surface mass and heat transfer from the porous walls were considered through the superposition of laminar swirling flow on a Berman flow with uniform

mass injection in a straight pipe. The flame structure was obtained assuming infinitely fast conversion of reactants into products and unity Lewis numbers, allowing the application of Shvab-Zel'dovich variables. Results from the perturbation analysis consider constant temperature at the walls, more specifically, at the fuel boiling point. The balance between the amount of energy necessary for the fuel to be heated from the injection temperature to its boiling point and the energy released by the reaction show that the system operates in fuel rich conditions. The flame extends towards the oxidizer region as it is observed in the underventilated case for the Burke-Schumann model.

The theoretical models presented in this manuscript can provide qualitative guidelines to the design of the discussed systems, such as the influence of inlet or dimensional parameters on flame position, flame confinement as well as overall system temperature and heat transfer. The analytical expressions presented herein, which are developed in a simplified framework, allow a fast and comprehensive description of the temperature, species and flow fields for all systems.

Bibliography

[1] F. J. Weinberg, The First Half-Million Years of Combustion Research and Today's Burning Problems, Proc. Combust. Inst. 15 (1) (1975) 1–17.

[2] E. Britannica, Fire, 2016.

[3] F. A. Williams, The Role of Theory in Combustion Science, Proc. Combust. Inst. 24 (1) (1992) 1–17.

[4] A. Liñán, M. Vera, A. L. Sánchez, Ignition, Liftoff, and Extinction of Gaseous Diffusion Flames, Annu. Rev. Fluid Mech. 47 (1) (2015) 293–314.

[5] R. J. Kee, M. E. Coltrin, P. Glarborg, Chemically Reacting Flow: Theory and Practice, Wiley-Interscience, Hoboken, N.J, 2003.

[6] M. D. Smooke, V. Giovangigli, Formulation of the Premixed and Nonpremixed Test Problems, in: M. D. Smooke (Ed.), Reduced Kinetic Mechanisms and Asymptotic Approximations for Methane-Air Flames, no. 384 in Lecture Notes in Physics, Springer Berlin Heidelberg, 1–28, 1991.

[7] Y. B. Zel'dovich, G. I. Barenblatt, V. B. Librovich, G. M. Makhviladze, The Mathematical Theory of Combustion and Explosions, Springer, 1985.

[8] M. T. Reagan, H. N. Najm, P. P. Pébay, O. M. Knio, R. G. Ghanem, Quantifying Uncertainty in Chemical Systems Modeling, Int. J. Chem. Kinet. 37 (6) (2005) 368–382.

[9] H. N. Najm, Uncertainty Quantification and Polynomial Chaos Techniques in Computational Fluid Dynamics, Annu. Rev. Fluid Mech. 41 (1) (2009) 35–52.

[10] V. Giovangigli, Multicomponent Flow Modeling, Springer Science & Business Media, 1999.

[11] S. P. Burke, T. E. W. Schumann, Diffusion Flames, Ind. Eng. Chem. Res. 20 (10) (1928) 998–1004.

[12] F. G. Roper, The Prediction of Laminar Jet Diffusion Flame Sizes: Part I. Theoretical Model, Combust. Flame 29 (1977) 219–226.

[13] T. Takeno, S. Ishizuka, A Tubular Flame Theory, Combust. Flame 64 (1) (1986) 83–98.

[14] V. A. Shvab, Svyaz' mezhdu temperaturnymi i skorostnymi polyami gazovogo fakela (The relationship between the temperature and the velocity fields in a gaseous flame), in: Isseledovanie Protsessov Goreniya Natural'nogo Topliva (Research on Combustion Processes in Natural Fuel), Moscow, 231–248, 1948.

[15] Y. B. Zel'dovich, K teorii gorenia neperemeshannykh gasov (on the theory of combustion of initially unmixed gases), Zh. Tekh. Fiz. 19 (10) (1949) 1199–1210.

[16] D. B. Spalding, Some Fundamentals of Combustion, Butterworths Scientific, 1955.

[17] H. Tsuji, Counterflow Diffusion Flames, Prog. Energy Combust. Sci. 8 (2) (1982) 93–119.

[18] S. Ishizuka, Characteristics of Tubular Flames, Prog. Energy Combust. Sci. 19 (3) (1993) 187–226.

[19] H. G. Wolfhard, W. G. Parker, A New Technique for the Spectroscopic Examination of Flames at Normal Pressures, Proc. Phys. Soc. London, Sect. A 62 (11) (1949) 722.

[20] C. K. Law, Combustion Physics, Cambridge University Press, Cambridge, 2010.

[21] A. E. Potter, J. N. Butler, A Novel Combustion Measurement Based on the Extinguishment of Diffusion Flames, ARS Journal 29 (1959) 54–56.

[22] D. B. Spalding, Theory of Mixing and Chemical Reaction in the Opposed-Jet Diffusion Flame, ARS Journal 31 (6) (1961) 763–771.

[23] T. P. Pandya, F. J. Weinberg, The Structure of Flat, Counter-Flow Diffusion Flames, Proc. R. Soc. London, Ser. A 279 (1379) (1964) 544–561.

[24] T. P. Pandya, F. J. Weinberg, The Study of the Structure of Laminar Diffusion Flames by Optical Methods, Proc. Combust. Inst. 9 (1) (1963) 587–596.

[25] A. E. Potter, S. Heimel, J. N. Butler, Apparent Flame Strength: A Measure of Maximum Reaction Rate in Diffusion Flames, Proc. Combust. Inst. 8 (1) (1961) 1027–1034.

[26] W. A. Hahn, J. O. L. Wendt, T. J. Tyson, Analysis of the Flat Laminar Opposed Jet Diffusion Flame with Finite Rate Detailed Chemical Kinetics, Combust. Sci. Technol. 27 (1-2) (1981) 1–17.

[27] W. A. Hahn, J. O. L. Wendt, NOx Formation in Flat, Laminar, Opposed Jet Methane Diffusion Flames, Proc. Combust. Inst. 18 (1) (1981) 121–131.

[28] H. Tsuji, I. Yamaoka, A Gasdynamic Analysis of the Counter-Flow Diffusion Flame in the Forward Stagnation Region of a Porous Cylinder, ISAS report 31 (5) (1966) 95–115.

[29] H. Tsuji, I. Yamaoka, The Counterflow Diffusion Flame in the Forward Stagnation Region of a Porous Cylinder, Proc. Combust. Inst. 11 (1) (1967) 979–984.

[30] H. Tsuji, I. Yamaoka, The Structure of Counterflow Diffusion Flames in the Forward Stagnation Region of a Porous Cylinder, Proc. Combust. Inst. 12 (1) (1969) 997–1005.

[31] H. Tsuji, I. Yamaoka, Structure Analysis of Counterflow Diffusion Flames in the Forward Stagnation Region of a Porous Cylinder, Proc. Combust. Inst. 13 (1) (1971) 723–731.

[32] F. E. Fendell, Ignition and Extinction in Combustion of Initially Unmixed Reactants, J. Fluid Mech. 21 (02) (1965) 281–303.

[33] L. Krishnamurthy, F. A. Williams, A Flame Sheet in the Stagnation-Point Boundary Layer of a Condensed Fuel, Acta Astronaut. 1 (5–6) (1974) 711–736.

[34] D. B. Spalding, The Combustion of Liquid Fuels, Proc. Combust. Inst. 4 (1) (1953) 847–864.

[35] S. Chung, C. K. Law, Structure and Extinction of Convective Diffusion Flames with General Lewis Numbers, Combust. Flame 52 (1983) 59–79.

[36] J. H. Kent, F. A. Williams, Extinction of Laminar Diffusion Flames for Liquid Fuels, Proc. Combust. Inst. 15 (1) (1975) 315–325.

[37] K. Seshadri, F. A. Williams, Effect of CF3Br on Counterflow Combustion of Liquid Fuel with Diluted Oxygen, in: Halogenated Fire Suppressants, vol. 16 of *ACS Symposium Series*, American Chemical Society, 149–182, 1975.

[38] K. Seshadri, Structure and Extinction of Laminar Diffusion Flames above Condensed Fuels with Water and Nitrogen, Combust. Flame 33 (1978) 197–215.

[39] K. Seshadri, F. A. Williams, Structure and Extinction of Counterflow Diffusion Flames above Condensed Fuels: Comparison between Poly(Methyl Methacrylate) and Its Liquid Monomer, Both Burning in Nitrogen–air Mixtures, Journal of Polymer Science: Polymer Chemistry Edition 16 (7) (1978) 1755–1778.

[40] A. Hamins, D. Trees, K. Seshadri, H. K. Chelliah, Extinction of Nonpremixed Flames with Halogenated Fire Suppressants, Combust. Flame 99 (2) (1994) 221–230.

[41] A. Hamins, K. Seshadri, Short Communication, Combust. Sci. Technol. 38 (1-2) (1984) 89–103.

[42] A. Hamins, K. Seshadri, Structure of Counterflow Diffusion Flames Burning Multicomponent Fuels, Proc. Combust. Inst. 20 (1) (1985) 1905–1913.

[43] A. Hamins, K. Seshadri, The Structure of Diffusion Flames Burning Pure, Binary, and Ternary Solutions of Methanol, Heptane, and Toluene, Combust. Flame 68 (3) (1987) 295–307.

[44] L. Krishnamurthy, F. A. Williams, K. Seshadri, Asymptotic Theory of Diffusion-Flame Extinction in the Stagnation-Point Boundary Layer, Combust. Flame 26 (1976) 363–377.

[45] M. Bui-Pham, K. Seshadri, Comparison between Experimental Measurements and Numerical Calculations of the Structure of Heptane-Air Diffusion Flames, Combust. Sci. Technol. 79 (4-6) (1991) 293–310.

[46] H. K. Chelliah, M. Bui-Pham, K. Seshadri, C. K. Law, Numerical Description of the Structure of Counterflow Heptane-Air Flames Using Detailed and Reduced Chemistry with Comparison to Experiments, Proc. Combust. Inst. 24 (1) (1992) 851–857.

[47] C. M. Müller, K. Seshadri, J. Y. Chen, Reduced Kinetic Mechanisms for Counterflow Methanol Diffusion Flames, in: N. Peters, B. Rogg (Eds.), Reduced Kinetic Mechanisms for Applications in Combustion Systems, no. 15 in Lecture Notes in Physics Monographs, Springer Berlin Heidelberg, 284–307, 1993.

[48] T. Niioka, S. Hasegawa, T. Tsukamoto, J. Sato, Diffusion-Flame Extinction of Liquid Fuel at Elevated Pressures, Combust. Flame 86 (1–2) (1991) 171–178.

[49] T. Hiraiwa, N. Ono, T. Niioka, High-Pressure Combustion Characteristics of Liquid Fuel in the Stagnation-Point Flow, Proc. Combust. Inst. 24 (1) (1992) 239–245.

[50] M. Juniper, N. Darabiha, S. Candel, The Extinction Limits of a Hydrogen Counterflow Diffusion Flame above Liquid Oxygen, Combust. Flame 135 (1–2) (2003) 87–96.

[51] K. Seshadri, S. Humer, R. Seiser, Activation-Energy Asymptotic Theory of Autoignition of Condensed Hydrocarbon Fuels in Non-Premixed Flows with Comparison to Experiment, Combust. Theory Model. 12 (5) (2008) 831–855.

[52] R. Grana, K. Seshadri, A. Cuoci, U. Niemann, T. Faravelli, E. Ranzi, Kinetic Modelling of Extinction and Autoignition of Condensed Hydrocarbon Fuels in Non-Premixed Flows with Comparison to Experiment, Combust. Flame 159 (1) (2012) 130–141.

[53] R. K. Gehmlich, A. Kuo, K. Seshadri, Experimental Investigations of the Influence of Pressure on Critical Extinction Conditions of Laminar Nonpremixed Flames Burning Condensed Hydrocarbon Fuels, Jet Fuels, and Surrogates, Proc. Combust. Inst. 35 (1) (2015) 937–943.

[54] T. Takagi, Y. Yoshikawa, K. Yoshida, M. Komiyama, S. Kinoshita, Studies on Strained Non-Premixed Flames Affected by Flame Curvature and Preferential Diffusion, Proc. Combust. Inst. 26 (1) (1996) 1103–1110.

[55] V. R. Katta, C. D. Carter, G. J. Fiechtner, W. M. Roquemore, J. R. Gord, J. C. Rolon, Interaction of a Vortex with a Flat Flame Formed between Opposing Jets of Hydrogen and Air, Proc. Combust. Inst. 27 (1) (1998) 587–594.

[56] K. Yoshida, T. Takagi, Transient Local Extinction and Reignition Behavior of Diffusion Flames Affected by Flame Curvature and Preferential Diffusion, Proc. Combust. Inst. 27 (1) (1998) 685–692.

[57] H. Finke, G. Grünefeld, An Experimental Investigation of Extinction of Curved Laminar Hydrogen Diffusion Flames, Proc. Combust. Inst. 28 (2) (2000) 2133–2140.

[58] J. C. Lee, C. E. Frouzakis, K. Boulouchos, Numerical Study of Opposed-Jet H2/Air Diffusion Flame - Vortex Interactions, Combust. Sci. Technol. 158 (1) (2000) 365–388.

[59] K. Yoshida, T. Takagi, Structural Studies of Locally Strained Diffusion Flames, JSME Int J., Ser. B 46 (1) (2003) 190–197.

[60] T. H. Lin, S. H. Sohrab, Influence of Vorticity on Counterflow Diffusion Flames, Combust. Sci. Technol. 52 (1-3) (1987) 75–90.

[61] T. H. Lin, S. H. Sohrab, Diffusion Flames in Opposed Counter-Rotating Jets, Combust. Sci. Technol. 63 (4-6) (1989) 193–207.

[62] W. J. Sllcu, S. H. Sohrab, Extinction of Counterflow Diffusion Flames in Counter-Rotating Finite Jets, Combust. Sci. Technol. 66 (1-3) (1989) 39–57.

[63] C. L. Chen, S. H. Sohrab, Extinction of Counterflow Diffusion Flames in Counter and Co-Rotating Finite Jets with General Lewis Numbers, Combust. Sci. Technol. 79 (4-6) (1991) 269–292.

[64] F.-J. Churng, C.-K. Chang, T.-H. Lin, Diffusion Flames in Corotating and Counterrotating Counterflows, JSME Int J., Ser. 2 35 (1) (1992) 95–102.

[65] S. Ishizuka, On the Behavior of Premixed Flames in a Rotating Flow Field: Establishment of Tubular Flames, Proc. Combust. Inst. 20 (1) (1985) 287–294.

[66] H. Kobayashi, M. Kitano, Extinction Characteristics of a Stretched Cylindrical Premixed Flame, Combust. Flame 76 (3) (1989) 285–295.

[67] D. M. Mosbacher, J. A. Wehrmeyer, R. W. Pitz, C.-J. Sung, J. L. Byrd, Experimental and Numerical Investigation of Premixed Tubular Flames, Proc. Combust. Inst. 29 (2) (2002) 1479–1486.

[68] K. Yamamoto, S. Ishizuka, Temperatures of Positively and Negatively Stretched Flames, JSME Int J., Ser. B 46 (1) (2003) 198–205.

[69] W. A. Sirignano, T. K. Pham, D. Dunn-Rankin, Miniature-Scale Liquid-Fuel-Film Combustor, Proc. Combust. Inst. 29 (1) (2002) 925–931.

[70] R. W. Pitz, S. Hu, P. Wang, Tubular Premixed and Diffusion Flames: Effect of Stretch and Curvature, Prog. Energy Combust. Sci. 42 (2014) 1–34.

[71] Y. Zhang, S. Ishizuka, H. Zhu, R. J. Kee, The Effects of Rotation Rate on the Characteristics of Premixed Propane–air Swirling Tubular Flames, Proc. Combust. Inst. 31 (1) (2007) 1101–1107.

[72] S. Hu, P. Wang, R. W. Pitz, M. D. Smooke, Experimental and Numerical Investigation of Non-Premixed Tubular Flames, Proc. Combust. Inst. 31 (1) (2007) 1093–1099.

[73] D. Dunn-Rankin, Tubular Flame Characteristics of Miniature Liquid Film Combustors, in: S. Ishiuka, D. Dunn-Rankin, R. W. Pitz (Eds.), Tubular Combustion, Momentum Press, New York, 189–205, 2013.

[74] P. Wang, S. Hu, R. W. Pitz, Numerical Investigation of the Curvature Effects on Diffusion Flames, Proc. Combust. Inst. 31 (1) (2007) 989–996.

[75] S. Hu, R. W. Pitz, Structural Study of Non-Premixed Tubular Hydrocarbon Flames, Combust. Flame 156 (1) (2009) 51–61.

[76] S. Hu, R. W. Pitz, Y. Wang, Extinction and Near-Extinction Instability of Non-Premixed Tubular Flames, Combust. Flame 156 (1) (2009) 90–98.

[77] Y. Wang, S. Hu, R. Pitz, Cellular Instabilities in Non-Premixed Opposed-Flow Tubular Flames, in: 47th AIAA Aerospace Sciences Meeting Including The New Horizons Forum and Aerospace Exposition, American Institute of Aeronautics and Astronautics, 1–12, 2009.

[78] S. W. Shopoff, P. Wang, R. W. Pitz, Experimental Study of Cellular Instability and Extinction of Non-Premixed Opposed-Flow Tubular Flames, Combust. Flame 158 (11) (2011) 2165–2177.

[79] S. W. Shopoff, P. Wang, R. W. Pitz, The Effect of Stretch on Cellular Formation in Non-Premixed Opposed-Flow Tubular Flames, Combust. Flame 158 (5) (2011) 876–884.

[80] H. Park, S. R. Lee, C. S. Yoo, A Numerical Study of the Diffusive-Thermal Instability of Nonpremixed Tubular Flames near Extinction Limit, Kosco Symposium (2014) 35–38.

[81] H. S. Bak, S. R. Lee, J. H. Chen, C. S. Yoo, A Numerical Study of the Diffusive-Thermal Instability of Opposed Nonpremixed Tubular Flames, Combust. Flame 162 (12) (2015) 4612–4621.

[82] T. K. Pham, D. Dunn-Rankin, W. A. Sirignano, Flame Structure in Small-Scale Liquid Film Combustors, Proc. Combust. Inst. 31 (2) (2007) 3269–3275.

[83] C. Giani, D. Dunn-Rankin, Miniature Fuel Film Combustor: Swirl Vane Design and Combustor Characterization, Combust. Sci. Technol. 185 (10) (2013) 1464–1481.

[84] R. Mattioli, T. K. Pham, D. Dunn-Rankin, Secondary Air Injection in Miniature Liquid Fuel Film Combustors, Proc. Combust. Inst. 32 (2) (2009) 3091–3098.

[85] Y.-H. Li, Y.-C. Chao, N. S. Amadé, D. Dunn-Rankin, Progress in Miniature Liquid Film Combustors: Double Chamber and Central Porous Fuel Inlet Designs, Exp. Therm. Fluid. Sci. 32 (5) (2008) 1118–1131.

[86] D. Dunn-Rankin, E. M. Leal, D. C. Walther, Personal Power Systems, Prog. Energy Combust. Sci. 31 (5–6) (2005) 422–465.

[87] A. P. da Silva, V. M. Sauer, D. Dunn-Rankin, Experimental Evaluation of a Miniature Liquid Film Combustor with Secondary Air Injection, in: Fall 2015 Meeting of the Western States Section of the Combustion Institute, Provo, UT, 1–9, 2015.

[88] W. A. Sirignano, S. Stanchi, R. Imaoka, Linear Analysis of a Liquid-Film Combustor, J. Propul. Power 21 (6) (2005) 1075–1091.

[89] R. B. Bird, W. E. Stewart, E. N. Lightfoot, Transport Phenomena, J. Wiley, New York, 2007.

[90] F. Homann, Der Einfluß Großer Zähigkeit Bei Der Strömung Um Den Zylinder Und Um Die Kugel, Z. angew. Math. Mech. 16 (3) (1936) 153–164.

[91] K. Hiemenz, Die Grenzschicht an Einem in Den Gleichformigen Flussigkeitsstrom Eingetauchten Geraden Kreiszlynder, Dinglers J. 326 (1911) 321–324.

[92] F. White, Viscous Fluid Flow, McGraw-Hill Science/Engineering/Math, 3rd edn., 2005.

[93] R. M. Terrill, J. P. Cornish, Radial Flow of a Viscous, Incompressible Fluid between Two Stationary, Uniformly Porous Discs, Z. Angew. Math. Phys. 24 (5) (1973) 676–688.

[94] T. W. Chapman, G. L. Bauer, Stagnation-Point Viscous Flow of an Incompressible Fluid between Porous Plates with Uniform Blowing, Appl. Sci. Res. 31 (3) (1975) 223–239.

[95] R. J. Kee, J. A. Miller, G. H. Evans, G. Dixon-Lewis, A Computational Model of the Structure and Extinction of Strained, Opposed Flow, Premixed Methane-Air Flames, Proc. Combust. Inst. 22 (1) (1989) 1479–1494.

[96] G. Dixon-Lewis, Structure of Laminar Flames, Proc. Combust. Inst. 23 (1) (1991) 305–324.

[97] G. Dixon-Lewis, V. Giovangigli, R. J. Kee, J. A. Miller, B. Rogg, M. D. Smooke, G. Stahl, J. Warnatz, Numerical Modeling of the Structure and Properties of Tubular Strained Laminar Premixed Flames, in: Dynamics of Deflagrations and Reactive Systems: Flames, vol. 131 of *Progress in Astronautics and Aeronautics*, American Institute of Aeronautics and Astronautics, 125–144, 1991.

[98] R. J. Kee, J. A. Miller, T. H. Jefferson, CHEMKIN: A General-Purpose, Problem-Independent, Transportable, FORTRAN Chemical Kinetics Code Package, Tech. Rep. SAND–80-8003, Sandia Labs., 1980.

[99] D. G. Goodwin, H. K. Moffat, R. L. Speth, Cantera: An Object-Oriented Software Toolkit for Chemical Kinetics, Thermodynamics, and Transport Processes, version 2.2.0, 2015.

[100] C. Company, Flow of Fluids through Valves, Fittings, and Pipe, Tech. Rep. 410, Crane Co., 1988.

[101] Z. Tan, Air Pollution and Greenhouse Gases: From Basic Concepts to Engineering Applications for Air Emission Control, Springer, 2014.

[102] W. G. Vincenti, C. H. Kruger, Introduction to Physical Gas Dynamics, Krieger, Malabar, FL, 1967.

[103] A. Liñán, The structure of diffusion flames, in: M. Onofri, A. Tesei (Eds.), Fluid Dynamic Aspects of Combustion Theory, E.T.S.I. Aeronáuticos (UPM), Harlow, Essex, 11–29, 1991.

[104] A. Liñán, F. A. Williams, Fundamental Aspects of Combustion, Oxford University Press, New York, 1993.

[105] J. Carpio, M. Sánchez-Sanz, E. Fernández-Tarrazo, Pinch-off in Forced and Non-Forced, Buoyant Laminar Jet Diffusion Flames, Combust. Flame 159 (1) (2012) 161–169.

[106] V. M. Sauer, A. J. K. Leiroz, M. J. Colaço, Analysis of Biofuel Reacting Flows in Ducts, in: Proceedings of the ENCIT 2012, Rio de Janeiro, RJ, 1–8, 2012.

[107] S. Chander, A. Ray, Flame Impingement Heat Transfer: A Review, Energy Convers. Manage. 46 (18–19) (2005) 2803–2837.

[108] S. Polat, B. Huang, A. S. Mujumdar, W. J. M. Douglas, Numerical Flow and Heat Transfer under Impinging Jets: A Review, Annual Review of Heat Transfer 2 (2) (1989) 157–197.

[109] R. Viskanta, Heat Transfer to Impinging Isothermal Gas and Flame Jets, Exp. Therm. Fluid. Sci. 6 (2) (1993) 111–134.

[110] C. E. Baukal, B. Gebhart, A Review of Semi-Analytical Solutions for Flame Impingement Heat Transfer, Int. J. Heat Mass Transfer 39 (14) (1996) 2989–3002.

[111] M. Sibulkin, Heat Transfer near the Forward Stagnation Point of a Body of Revolution, J. Aeronaut. Sci. 19 (8) (1952) 570–571.

[112] J. A. Fay, F. R. Riddell, Theory of Stagnation Point Heat Transfer in Dissociated Air, J. Aerosp. Sci. 25 (2) (1958) 73–85.

[113] D. E. Rosner, Convective Heat Transfer with Chemical Reaction, Tech. Rep. AD269816, Aeron. Res. Lab., 1961.

[114] M. J. Remie, M. F. G. Cremers, K. R. A. M. Schreel, L. P. H. de Goey, Analysis of the Heat Transfer of an Impinging Laminar Flame Jet, Int. J. Heat Mass Transfer 50 (13–14) (2007) 2816–2827.

[115] L. Lees, Laminar Heat Transfer over Blunt-Nosed Bodies at Hypersonic Flight Speeds, J. Jet Propulsion 26 (4) (1956) 259–269.

[116] H. H. Liakos, M. K. Koukou, N. C. Markatos, M. A. Founti, Effects of Pressure and Impingement Angle in Flaming Processes, Can. J. Chem. Eng. 78 (4) (2000) 834–841.

[117] G. K. Malikov, D. L. Lobanov, K. Y. Malikov, V. G. Lisienko, R. Viskanta, A. G. Fedorov, Direct Flame Impingement Heating for Rapid Thermal Materials Processing, Int. J. Heat Mass Transfer 44 (9) (2001) 1751–1758.

[118] H. H. Liakos, E. P. Keramida, M. A. Founti, N. C. Markatos, Heat and Mass Transfer Study of Impinging Turbulent Premixed Flames, Heat Mass Transfer 38 (4-5) (2002) 425–432.

[119] M. J. Remie, G. Särner, M. F. G. Cremers, A. Omrane, K. R. A. M. Schreel, L. E. M. Aldén, L. P. H. de Goey, Heat-Transfer Distribution for an Impinging Laminar Flame Jet to a Flat Plate, Int. J. Heat Mass Transfer 51 (11–12) (2008) 3144–3152.

[120] M. J. Remie, G. Särner, M. F. G. Cremers, A. Omrane, K. R. A. M. Schreel, M. Aldén, L. P. H. de Goey, Extended Heat-Transfer Relation for an Impinging Laminar Flame Jet to a Flat Plate, Int. J. Heat Mass Transfer 51 (7–8) (2008) 1854–1865.

[121] W.-D. Hsieh, S.-S. Hou, T.-H. Lin, Methane Flames in a Jet Impinging onto a Wall, Proc. Combust. Inst. 30 (1) (2005) 267–275.

[122] W.-D. Hsieh, T.-H. Lin, Methane Flame Stability in a Jet Impinging onto a Wall, Energy Convers. Manage. 46 (5) (2005) 727–739.

[123] S.-S. Hou, S.-S. Yang, S.-J. Chen, T.-H. Lin, Interactions for Flames in a Coaxial Flow with a Stagnation Point, Combust. Flame 132 (1–2) (2003) 58–72.

[124] L. L. Dong, C. S. Cheung, C. W. Leung, Characterization of Impingement Region from an Impinging Inverse Diffusion Flame Jet, Int. J. Heat Mass Transfer 56 (1–2) (2013) 360–369.

[125] Y.-C. Chien, D. Dunn-Rankin, Electric Field Effects on Carbon Monoxide Release from Impinging Flames, in: 8th U.S. National Combustion Meeting, Park City, UT, 1–10, 2013.

[126] Y.-C. Chien, Electrical Aspects of Impinging Flames, Ph.D. thesis, University of California, Irvine, Irvine, CA, 2015.

[127] Y.-C. Chien, D. Escofet-Martin, D. Dunn-Rankin, CO Emission from an Impinging Non-Premixed Flame, Combust. Flame 174 (2016) 16–24.

[128] V. M. Sauer, D. Dunn-Rankin, Impinging Coflow Nonpremixed Methane-Air Flames with Unity Lewis Number, in: 9th US National Combustion Meeting, Cincinnati, OH, 1–10, 2015.

[129] V. M. Sauer, D. Dunn-Rankin, Impinging Nonpremixed Coflow Methane–air Flames with Unity Lewis Number, Proc. Combust. Inst. 36 (1) (2017) 1411–1419.

[130] F. G. Roper, C. Smith, A. C. Cunningham, The Prediction of Laminar Jet Diffusion Flame Sizes: Part II. Experimental Verification, Combust. Flame 29 (1977) 227–234.

[131] P. B. Sunderland, Z.-G. Yuan, D. L. Urban, Shapes of Buoyant and Nonbuoyant Methane Laminar Jet Diffusion Flames, in: Proceedings of the 4th International Microgravity Combustion Workshop, Cleveland, OH, 129–134, 1997.

[132] S. S. Krishnan, J. M. Abshire, P. B. Sunderland, Z.-G. Yuan, J. P. Gore, Analytical Predictions of Shapes of Laminar Diffusion Flames in Microgravity and Earth Gravity, Combust. Theory Model. 12 (4) (2008) 605–620.

[133] R. von Mises, Bemerkungen zur Hydrodynamik, Z. angew. Math. Mech. 7 (6) (1927) 425.

[134] S. C. Li, A. S. Gordon, F. A. Williams, A Simplified Method for the Computation of Burke-Schumann Flames in Infinite Atmospheres, Combust. Sci. Technol. 104 (1-3) (1995) 75–91.

[135] C. Vázquez-Espí, Analysis of Axisymmetric Laminar Jet Diffusion Flames for Small Values of the Stoichiometric Mixture Fraction, Combust. Sci. Technol. 171 (1) (2001) 1–38.

[136] P. B. Sunderland, G. M. Faeth, Soot Formation in Hydrocarbon/Air Laminar Jet Diffusion Flames, Combust. Flame 105 (1–2) (1996) 132–146.

[137] M. N. Ozisik, Heat Transfer: A Basic Approach, Mcgraw-Hill College, New York, 1984.

[138] J. I. Masters, Some Applications in Physics of the P Function, J. Chem. Phys 23 (10) (1955) 1865–1874.

[139] F. A. Williams, Combustion Theory, Addison-Wesley Pub. Co., Menlo Park, 2nd edn., 1994.

[140] L. F. Shampine, P. H. Muir, H. Xu, A User-Friendly FORTRAN BVP Solver, Journal of Numerical Analysis, Industrial and Applied Mathematics 1 (2) (2006) 201–217.

[141] R. Piessens, E. de Doncker-Kapenga, C. W. Überhuber, D. K. Kahaner, Quadpack: A Subroutine Package for Automatic Integration, Springer, Berlin; New York, 1983.

[142] S. S. Penner, M. Y. Bahadori, E. M. Kennedy, Laminar Diffusion Flames with Cylindrical Symmetry, Arbitrary Values of Diffusion Coefficients and Inlet Velocities, and Chemical Reactions in the Approach Streams, in: Dynamics of Flames and Reactive Systems, Progress in Astronautics and Aeronautics, American Institute of Aeronautics and Astronautics, 261–292, 1985.

[143] A. Lazzarini, R. Krauss, H. Chelliah, G. Linteris, Extinction of Counterflow Diffusion Flames with Fine-Water Droplets, in: Halon Options Technical Working Conference, 2–4, 2000.

[144] G. Thomas, The Quenching of Laminar Methane-Air Flames by Water Mists, Combust. Flame 130 (1–2) (2002) 147–160.

[145] B. Han, A. F. Ibarreta, C.-J. Sung, J. S. T'ien, Structure of Low-Stretch Methane Nonpremixed Flames, Combust. Flame 149 (1–2) (2007) 173–190.

[146] S. Li, P. Libby, F. A. Williams, Experimental and Theoretical Studies of Counterflow Spray Diffusion Flames, Proc. Combust. Inst. 24 (1) (1992) 1503–1512.

[147] M. N. Sasongko, M. Mikami, A. Dvorjetski, Extinction Condition of Counterflow Diffusion Flame with Polydisperse Water Sprays, Proc. Combust. Inst. 33 (2) (2011) 2555–2562.

[148] F. L. Dryer, Water Addition to Practical Combustion Systems—Concepts and Applications, Proc. Combust. Inst. 16 (1) (1977) 279–295.

[149] S. Circone, S. H. Kirby, L. A. Stern, Direct Measurement of Methane Hydrate Composition along the Hydrate Equilibrium Boundary, J. Phys. Chem. B 109 (19) (2005) 9468–9475.

[150] A. M. Lentati, H. K. Chelliah, Dynamics of Water Droplets in a Counterflow Field and Their Effect on Flame Extinction, Combust. Flame 115 (1) (1998) 158–179.

[151] A. M. Lentati, H. K. Chelliah, Physical, Thermal, and Chemical Effects of Fine-Water Droplets in Extinguishing Counterflow Diffusion Flames, Proc. Combust. Inst. 27 (2) (1998) 2839–2846.

[152] R. Seiser, K. Seshadri, The Influence of Water on Extinction and Ignition of Hydrogen and Methane Flames, Proc. Combust. Inst. 30 (1) (2005) 407–414.

[153] D. Zhao, H. Yamashita, K. Kitagawa, N. Arai, T. Furuhata, Behavior and Effect on NOx Formation of OH Radical in Methane-Air Diffusion Flame with Steam Addition, Combust. Flame 130 (4) (2002) 352–360.

[154] A. Katoh, M. Shinoda, K. Kitagawa, A. K. Gupta, Visualization of Steam Addition Effect on OH Distribution in a Flame by Isotope Shift/Planar Laser-Induced Fluorescence (IS/PLIF) Spectroscopy, J. Eng. Gas Turbines Power 128 (1) (2004) 8–12.

[155] R. E. Padilla, Structure and Behavior of Water-Laden Methane/Air Flames, Ph.D. thesis, University of California, Irvine, Irvine, CA, 2016.

[156] S. Lee, R. Padilla, D. Dunn-Rankin, T. Pham, O. C. Kwon, Extinction Limits and Structure of Counterflow Nonpremixed H2O-Laden CH4/Air Flames, Energy 93, Part 1 (2015) 442–450.

[157] S. Lee, H. Ha, D. Dunn-Rankin, O. C. Kwon, Effects of Pressure on Structure and Extinction Limits of Counterflow Nonpremixed Water-Laden Methane/Air Flames, Energy 134 (2017) 545–553.

[158] A. Liñán, Diffusion-Controlled Combustion, in: H. Aref, J. W. Phillips (Eds.), Mechanics for a New Mellennium, Kluwer Academic Publishers, Dordrecht, 487–502, 2000.

[159] I. K. Puri, K. Seshadri, M. D. Smooke, D. E. Keyes, A Comparison between Numerical Calculations and Experimental Measurements of the Structure of a Counterflow Methane-Air Diffusion Flame, Combust. Sci. Technol. 56 (1-3) (1987) 1–22.

[160] Q. Li, L. Fernandez, P. Zhang, P. Wang, Stretch and Curvature Effects on NO Emission of H2/Air Diffusion Flames, Combust. Sci. Technol. 187 (10) (2015) 1520–1541.

[161] D. A. Nield, A. Bejan, Convection in Porous Media, Springer, New York, 2013.

[162] V. M. Sauer, R. E. Padilla, D. Dunn-Rankin, Analyzing Water-Laden Non-Premixed Counterflow Flames Using the Mixture Fraction/ Excess-Enthalpy Approach, Fort Collins, CO, 1–8, 2013.

[163] Y. Xuan, G. Blanquart, M. E. Mueller, Modeling Curvature Effects in Diffusion Flames Using a Laminar Flamelet Model, Combust. Flame 161 (5) (2014) 1294–1309.

[164] M. D. Smooke, V. Giovangigli, Extinction of Tubular Premixed Laminar Flames with Complex Chemistry, Proc. Combust. Inst. 23 (1) (1991) 447–454.

[165] P. Wang, J. A. Wehrmeyer, R. W. Pitz, Stretch Rate of Tubular Premixed Flames, Combust. Flame 145 (1–2) (2006) 401–414.

[166] S. Ishizuka, T. Motodamari, D. Shimokuri, Rapidly Mixed Combustion in a Tubular Flame Burner, Proc. Combust. Inst. 31 (1) (2007) 1085–1092.

[167] B. Shi, D. Shimokuri, S. Ishizuka, Methane/Oxygen Combustion in a Rapidly Mixed Type Tubular Flame Burner, Proc. Combust. Inst. 34 (2) (2013) 3369–3377.

[168] D. B. Spalding, Combustion of Liquid Fuels, Nature 165 (4187) (1950) 160–160.

[169] I. G. Namyatov, S. S. Minaev, V. S. Babkin, V. A. Bunev, A. A. Korzhavin, Diffusion Combustion of a Liquid Fuel Film on a Metal Substrate, Combust. Explos. Shock Waves 36 (5) (2000) 562–570.

[170] M. Kaplan, M. J. Hall, The Combustion of Liquid Fuels within a Porous Media Radiant Burner, Exp. Therm. Fluid. Sci. 11 (1) (1995) 13–20.

[171] D. Sequera, A. K. Agrawal, Passive Control of Noise and Instability in a Swirl-Stabilized Combustor with the Use of High-Strength Porous Insert, J. Eng. Gas Turbines Power 134 (5) (2012) 051505/1–11.

[172] H. Ishida, Flame Spread over Fuel-Soaked Ground, Fire Saf. J. 10 (3) (1986) 163–171.

[173] B. Shi, J. Hu, S. Ishizuka, Carbon Dioxide Diluted Methane/Oxygen Combustion in a Rapidly Mixed Tubular Flame Burner, Combust. Flame 162 (2) (2015) 420–430.

[174] C. K. Chan, K. S. Lau, W. K. Chin, R. K. Cheng, Freely Propagating Open Premixed Turbulent Flames Stabilized by Swirl, Proc. Combust. Inst. 24 (1) (1992) 511–518.

[175] A. S. Berman, Laminar Flow in Channels with Porous Walls, J. Appl. Phys. 24 (9) (1953) 1232–1235.

[176] S. W. Yuan, A. B. Finkelstein, Laminar Pipe Flow with Injection and Suction through a Porous Wall, Tech. Rep. AD058831, Princeton University, 1955.

[177] E. R. G. Eckert, P. L. Donoughe, B. J. Moore, Velocity and Friction Characteristics of Laminar Viscous Boundary-Layer and Channel Flow over Surfaces with Ejection or Suction, Tech. Rep. TN-4102, NACA, Cleveland, OH, 1957.

[178] A. S. Berman, Effects of Porous Boundaries on the Flow of Fluids in Systems with Various Geometries, in: Proceedings of the Second United Nations International Conference on the Peaceful Uses of Atomic Energy, vol. 4, Oak Ridge Gaseous Diffusion Plant, Tenn., Geneva, 351–358, 1958.

[179] J. White, F. M., Laminar Flow in a Uniformly Porous Tube, J. Appl. Mech. 29 (1) (1962) 201–204.

[180] R. M. Terrill, P. W. Thomas, On Laminar Flow through a Uniformly Porous Pipe, Appl. Sci. Res. 21 (1) (1969) 37–67.

[181] R. M. Terrill, Laminar Flow in a Uniformly Porous Channel, Aeronautical Quarterly 15 (3) (1964) 299–310.

[182] J. R. Sellars, Laminar Flow in Channels with Porous Walls at High Suction Reynolds Numbers, J. Appl. Phys. 26 (4) (1955) 489–490.

[183] R. M. Terrill, Flow through a Porous Annulus, Appl. Sci. Res. 17 (3) (1967) 204–222.

[184] R. M. Terrill, P. W. Thomas, Spiral Flow in a Porous Pipe, Phys. Fluids 16 (3) (1973) 356–359.

[185] S. Prager, Spiral Flow in a Stationary Porous Pipe, Phys. Fluids 7 (6) (1964) 907–908.

[186] W. H. H. Banks, M. B. Zaturska, Swirling Flow in a Porous Pipe with an Accelerating Wall, Acta Mech. 119 (1) (1996) 1–12.

[187] S. Chellam, M. R. Wiesner, C. Dawson, G. R. Brown, Laminar Flow in Porous Ducts, Rev. Chem. Eng. 11 (1) (2011) 53–99.

[188] S. W. Yuan, A. B. Finkelstein, Heat Transfer in Laminar Pipe Flow with Uniform Coolant Injection, J. Jet Propulsion 28 (3) (1958) 178–181.

[189] L. Graetz, Ueber Die Wärmeleitungsfähigkeit von Flüssigkeiten, Ann. Phys. 254 (1) (1882) 79–94.

[190] R. B. Kinney, Fully Developed Frictional and Heat-Transfer Characteristics of Laminar Flow in Porous Tubes, Int. J. Heat Mass Transfer 11 (9) (1968) 1393–1401.

[191] G. Raithby, Laminar Heat Transfer in the Thermal Entrance Region of Circular Tubes and Two-Dimensional Rectangular Ducts with Wall Suction and Injection, Int. J. Heat Mass Transfer 14 (2) (1971) 223–243.

[192] Y. Peng, S. W. Yuan, Laminar Pipe Flow with Mass Transfer Cooling, J. Heat Transfer 87 (2) (1965) 252–258.

[193] V. M. Eroshenko, L. I. Zaichik, V. B. Rabovskii, Heat Exchange in Tubes with Permeable Walls in the Presence of Internal Heat Sources, J. Eng. Phys. Thermophys. 38 (3) (1980) 222–227.

[194] L. Collatz, H. Görtler, Rohrströmung mit schwachem Drall, Z. Angew. Math. Phys. 5 (2) (1954) 95–110.

[195] L. Talbot, Laminar Swirling Pipe Flow, J. Appl. Mech. 21 (1954) 1–7.

[196] B. C. Deka, Some Effects of Weak Swirl on Laminar Pipe Flow, Proc. Indian Nat. Sci. Acad. Part A 29 (2A) (1963) 251–270.

[197] B. C. Deka, Some Effects of Weak Swirl on Laminar Pipe Flow, Proc. Indian Nat. Sci. Acad. Part A 32 (3A) (1966) 292–317.

[198] Z. Lavan, H. Nielsen, A. A. Fejer, Separation and Flow Reversal in Swirling Flows in Circular Ducts, Phys. Fluids 12 (9) (1969) 1747–1757.

[199] F. Kreith, O. K. Sonju, The Decay of a Turbulent Swirl in a Pipe, J. Fluid Mech. 22 (02) (1965) 257–271.

[200] R. B. Kinney, E. M. Sparrow, Laminar Swirling Flow in a Tube with Surface Mass Transfer, J. Appl. Mech. 37 (4) (1970) 936–944.

[201] C. S. Lee, J. J. Ou, S. H. Chen, The Velocity Profile and Resultant Mixing with Chemical Reaction in Rotating Tubular Flow, Chem. Eng. Sci. 42 (1) (1987) 53–61.

[202] S. Mohan, M. Matalon, Diffusion Flames and Diffusion Flame-Streets in Three Dimensional Micro-Channels, Combust. Flame 177 (2017) 155–170.

[203] M. Abramowitz, I. A. Stegun (Eds.), Handbook of Mathematical Functions: With Formulas, Graphs, and Mathematical Tables, Dover Publications, New York, 9 edn., 1965.

[204] T. C. Lieuwen, Unsteady Combustor Physics, Cambridge University Press, New York, 2012.

[205] W. A. Robinson, The Existence of Multiple Solutions for the Laminar Flow in a Uniformly Porous Channel with Suction at Both Walls, J. Engrg. Math. 10 (1) (1976) 23–40.

[206] F. M. Skalak, C.-Y. Wang, Pulsatile Flow in a Tube with Wall Injection and Suction, Appl. Sci. Res. 33 (3-4) (1977) 269–307.

[207] T. W. Secomb, Flow in a Channel with Pulsating Walls, J. Fluid Mech. 88 (2) (1978) 273–288.

[208] F. Skalak, C. Wang, On the Nonunique Solutions of Laminar Flow through a Porous Tube or Channel, SIAM J. Appl. Math. 34 (3) (1978) 535–544.

[209] M. B. Zaturska, P. G. Drazin, W. H. H. Banks, On the Flow of a Viscous Fluid Driven along a Channel by Suction at Porous Walls, Fluid Dyn. Res. 4 (3) (1988) 151–178.

[210] L. Durlofsky, J. F. Brady, The Spatial Stability of a Class of Similarity Solutions, Phys. Fluids 27 (5) (1984) 1068–1076.

[211] P. Haldenwang, Laminar Flow in a Two-Dimensional Plane Channel with Local Pressure-Dependent Crossflow, J. Fluid Mech. 593 (2007) 463–473.

[212] G. D. Raithby, D. C. Knudsen, Hydrodynamic Development in a Duct with Suction and Blowing, J. Appl. Mech. 41 (4) (1974) 896–902.

[213] L. Galowin, L. Fletcher, M. Desantis, Investigation of Laminar Flow in a Porous Pipe with Variable Wall Suction, AIAA Journal 12 (11) (1974) 1585–1589.

[214] K. L. Judd, L. Maliar, S. Maliar, R. Valero, Smolyak Method for Solving Dynamic Economic Models: Lagrange Interpolation, Anisotropic Grid and Adaptive Domain, Journal of Economic Dynamics and Control 44 (2014) 92–123.

[215] V. M. Sauer, F. F. Fachini, D. Dunn-Rankin, Structure of Nonpremixed Swirl-Type Tubular Flames Burning Condensed Fuels with Unity Lewis Numbers, in: 10th US National Combustion Meeting, College Park, MD, 1–6, 2017.

[216] V. M. Sauer, F. F. Fachini, D. Dunn-Rankin, Nonpremixed Swirl-Type Tubular Flames Burning Liquid Fuels, J. Fluid Mech. (2017) Under review.